Università degli Studi della Calabria
Facoltà di Scienze Matematiche, Fisiche e Naturali

Dottorato di Ricerca in Fisica
XXII ciclo

Tesi di Dottorato

Study on Z^0 and Higgs production at ATLAS
&
DREAM calorimetry

Dottorando:
Tommaso Venturelli

Supervisore:	Coordinatore:
Prof.ssa Laura La Rotonda	**Prof. Giovanni Falcone**

settore scientifico disciplinare FIS/01-FIS/04

A mio padre.

Contents

Contents

Introduzione

Nel novembre 2009 una nuova generazione di esperimenti di Fisica delle Alte Energie (HEP) hanno preso il via al Large Hadron Collider (LHC), al CERN, il Laboratorio Europeo per la Fisica delle Particelle che si trova a Ginevra, in Svizzera. LHC è un collider protone-protone progettato per avere un'energia di centro di massa di 14 TeV e una luminosità di 10^{34} cm^{-2} s^{-1}; esplorando la scala del TeV, LHC aprirà nuove frontiere nella ricerca di nuove particelle. Uno dei suoi principali obbiettivi sarà la ricerca del bosone di Higgs, necessario per confermare il meccanismo di rottura spontanea della simmetria nel Modello Standard, che si pensa giochi un ruolo fondamentale nella generazione delle masse delle particelle. Inoltre, le elevate sezioni d'urto permetteranno di studi sui processi del Modello Standard con altissima precisione.

Allo scopo di sfruttare al meglio le potenzialità fornite dal collider, quattro esperimenti sono stati posizionati sull'anello di LHC: due rivelatori "general purpose" (ATLAS e CMS), un esperimento di fisica del beauty (LHC-b), progettato per compiere misure di precisione sulla violazione di CP, e un rivelatore dedicato allo studio della fisica delle interazioni forti ad alte densità di energia (ALICE), grazie alla possibilità di LHC di poter accelerare anche ioni con masse che arrivano a quella dei nuclei di piombo.

La prima parte della mia tesi è legata alla ricerca dell'Higgs del Modello Standard per il canale $H{\rightarrow}ZZ^*{\rightarrow}4l$ nell'esperimento ATLAS, nel range di masse 120-180 GeV. In questo range, il rapporto segnale-background è meno favorevole che a masse più elevate; in aggiunta al continuum del background irriducibile $ZZ{\rightarrow}4l$, canali come $Zbb{\rightarrow}2lbb$ e $tt{\rightarrow}WbWb{\rightarrow}l\nu bl\nu b$ costituiscono il background riducibile e sono dominanti a livello di produzione. Ho sviluppato una parte dell'analisi "tecnica" relativa a questo canale, e ho contribuito al miglioramento di due diversi metodi, alternativi a quelli standard, per stimare la forma e il contributo al segnale di tali background.

Lo studio dei bosoni W e Z, che sono oggetti fisici dalle caratteristiche

Introduction

ben note, permetterà una migliore comprensione del rivelatore durante il primo periodo di presa dati. La misura della sezione d'urto, e il suo confronto con le previsioni teoriche, può essere un buon test per LHC, e sarà poi accompagnato da misure di precisione ad alte luminosità delle proprietà di *W* e *Z*. La seconda parte di questa tesi si incentra sulla stima del contributo del background nella misura della sezione d'urto del canale *Z*→2μ in ATLAS. Tutta l'analisi presentata è stata effettuata partendo da un energia di centro massa di 10 TeV.

Come l'esperienza con ATLAS insegna, la maggior parte dei rivelatori usati nei moderni esperimenti con collider sono molto complessi, e sono necessari molti anni di progettazione e test su prototipi prima che questi possano essere realmente utilizzabili e costruiti su grande scala. Per questa ragione parecchi sforzi sono incentrati attualmente sul concepire e testare rivelatori da usare nella prossima generazione di esperimenti di Fisica delle Alte Energie. Una tecnica di calorimetria nuova e assai promettente è il Dual REAdout Method (DREAM). Questa tecnica non è soggetta alle limitazioni dei calorimetri adronici tradizionali; la collaborazione internazionale DREAM sta provando differenti approcci, come utilizzare diversi tipi di fibre o materiali omogenei, con lo scopo di costruire un calorimetro adronico di elevata risoluzione. Nella terza parte della mia tesi espongo nel dettaglio questa tecnica e mostro le analisi a cui ho partecipato come membro del gruppo di Cosenza, parte della collaborazione DREAM.

Questa tesi è strutturata come segue:

il primo capitolo dà una descrizione generale dell'impianto complessivo dell'esperimento: vengono descritti il collider LHC e il rivelatore ATLAS;

il secondo capitolo descrive la fisica di Higgs, *W* e *Z*, dando il background teorico, descrivendo la produzione dei tre bosoni a LHC e i loro principali canali di decadimento, e illustrando l'attuale limite sperimentale sulla massa dell'Higgs;

il terzo capitolo è dedicato al software di ATLAS utilizzato nell'analisi per generare, simulare e ricostruire gli eventi nell'analisi;

il quarto capitolo si incentra sulla ricerca del bosone di Higgs, e descrive i risultati di un'analisi tecnica preliminare fatta come membro dell'Higgs working group e due metodi per estrarre il background nella regione della massa dell'Higgs;

il quinto capitolo fornisce una descrizione dell'analisi fatta sul background per il canale *Z*→2μ a 10 TeV, mostrando diversi metodi per valutare dai dati il contributo del background al segnale misurato;

nel sesto capitolo sono descritti in dettaglio la tecnica DREAM e le ragioni che hanno spinto al suo sviluppo; in particolare vengono mostrati i risultati dei test beam di DREAM che impiegavano materiali omogenei (in questo caso cristalli).

Chapter 1

LHC and the ATLAS experiment

The LHC (Large Hardon Collider)[1][2] is a proton-proton collider with a center of mass energy of 14 TeV and 10^{34} cm^{-2} s^{-1} luminosity (Figure 1.1). The energy of LHC is about seven times larger than the energy of Tevatron collider at Fermilab (the machine that previously had the highest center of mass energy) and allows the production of particles with mass up to 5 TeV.

The LHC supports four large scale experiments: ATLAS and CMS, to perform precision measures and to search for new particles; LHCb to perform dedicated studies on physics of B-hadrons and of CP-violations; ALICE, a heavy-ion experiment, that will study matter behavior at high energies and densities.

Two proton beams started to circulate in the LHC rings on the 10th of September 2008. On the 19th of September 2008, an accident occurred in sector 3-4, provoking a destructive release of a large volume of Helium from the magnet cold mass in the insulation vacuum of the sector. This accident led to a sudden long shut-down of the machine, during which LHC has necessitated a full-scale repair. All these operations lasted until the summer 2009; on the 23rd of November the first collisions at the injection energy, 450 TeV, were recorded by the four LHC experiments. On the 19th of March 2010 the beams reached an energy of 3.5 TeV; on the 14th of October 2010 a luminosity of 1.01×10^{32} cm^{-2} s^{-1} was reached. The final energy and luminosity are foreseen after the technical stop in 2012.

The chapter is organized as follow: in section 1.1 I will describe the main reasons behind the construction of LHC. In section 1.2 I will give a general description of the collider and of the experiments. In section 1.3 the ATLAS detector is described.

1.1 Motivations of LHC

The High Energy physic studies the elementary particles and their interactions. To investigate the universe to the smallest scales we need to reach more and more high energies. This is well explained by the relation between the momentum of a particle and its wave length in the De Broglie equation $\lambda = \dfrac{h}{p}$ ($h = 6.6260755 \times 10^{34}$ Js is the Plank constant) that show how the higher momenta are able to reveal the finest structure of particles.

The Standard Model[3][4] is a theoretical model able to describe the behavior of matter at the smallest scale and highest energy. The SM is a Quantum Field Theory based on local $SU(3)_C \times SU(2)_T \times U(1)_Y$ gauge symmetries; $SU(3)_C$ is associated to strong interactions (colour), the $SU(2)_T$ and $U(1)_Y$ are associated to the electroweak interactions (weak isospin and hypercharge). Matter fields are described by spin-½ point-like fermions, while the mediators of interactions are spin-1 gauge bosons.

The fermions are divided in quarks (fractionary charge and colour, i.e. they feels strong interaction) and leptons (unitary charge and no colour). Both of these groups interact electroweakly. Each of these groups is divided into three families. Each lepton family is composed by a massive charged lepton (e, μ, τ) with unitary charge and a massless neutral neutrino (ν_e, ν_μ, ν_τ). Each quark family is composed by a massive quark with charge 2/3 e (u, c, t) and a massive quark with charge -1/3 e (d, s, b). Each family is identical to other except for the mass of the particles. The antiparticles are also grouped in analogue six families. Other particles (hadrons) are produced from strong interaction between quarks. Hadrons are divided in barions (3 quarks) and mesons (2 quarks).

The strong interaction is mediated by eight colored neutral massless vector bosons, the gluons. Four vector bosons mediate the electroweak interaction: two massive charged bosons W (responsables of charged current interactions), a massive neutral boson Z (responsable of neutral current interaction) and a massless neutral boson γ, the photon (responsable of electromagnetic interactions).

The mass of the fundamental fermions and of the $W^\pm$ and Z bosons are given by the spontaneous symmetry breaking of the $SU(2)_T \times U(1)_Y$ interaction, originated by the existence of a theoretical Higgs Field with a non zero expectation value in the vacuum. One physical degree of freedom remains in the Higgs sector after the symmetry breaking, and it should manifest itself as a massive neutral scalar boson Higgs (see chapter 2).

Many Standard Model predictions are verified at a level of 0,1% or better, but some fundamental aspects are not included into it and some aspects of the

Fig. 1.1: Overview of the CERN area. The LHC ring and its four experiments are schematically indicated.

model itself are still not clear. At large mass scale there is a problem of fine tuning (naturalness problem): radiative corrections to the Higgs boson mass diverge unless very delicate and specific cancellation is postulated. Moreover, there are hints that the coupling constants of electromagnetic, weak and strong interactions could unify at very high energy[5][6]. In the Standard Model the coupling constants extrapolated from experimental data don't meet at a single point. These problems are solved, for example, in the Supersymmetric theories (SUSY). Other problems of the SM are the absent description of neutrino oscillations, the presence of many arbitrary parameters, and the lack of unification of gravity with strong and electroweak interactions.

Both in the Standard Model and in many theories which try to complete and expand it, something is foreseen at the TeV scale; therefore, there are strong physics motivations supporting LHC.

A first motivation is the problem of the **origin of the mass**. Usually in the SM the Higgs mechanism is used to explain the mass of fermions, but the value of Higgs mass is not predicted by the theory, also if it should not exceed 1 TeV. Until now, no experiment has found the Higgs boson up the limit of 114 GeV[7].

The standard model has some flaws and obscure points; SUSY theories can resolve many of these problems but they need a lot of new particles to work. The **physics beyond the Standard Model** is another point of interest of LHC, as supersymmetrical particles with masses up to 2 TeV can be produced and detected, such as the five Higgs bosons with a mass at TeV scale that are predicted by the Minimal Supersymmetric extension of the Standard Model.

An aspect complementary to the search of new physics are the **precision measurements** of properties and interactions of the known particles; any observed deviation from the Standard Model would be a signal for new physics. In particular, measurements of the W mass, of $WW\gamma$ and WWZ Triple Gauge Couplings are foreseen.

Another aspect of interest for LHC is the study of ***b*-physics**, the main

issue being the observation of CP-violation in the B^0_d system and the measurement of the three angles of the Cabibbo-Kobayashi-Maskawa matrix. The investigation of *B-B*bar mixing in the B^0_s system, rare *b*-decays and general spectroscopy of states with *b* quarks will be of great interest. These measurements have a dedicated detector, LHCb[8].

The great number of top quark that will be produced at LHC will give a huge statistic for the analysis of **top physics**, allowing a gain in top mass resolution (merely limited by theoretical uncertainties, rather than by statistical ones) and a study of its decay channels in details.

Finally, a study in **plasma physics** on the phase transition from hadronic matter to plasma of deconfined quarks and gluons will be possible. It is believed that an inverse transition (from plasma to hadronic matter) happened in the universe about 10 µs after the Big Bang. A dedicated experiment, ALICE, will perform these studies[9].

1.2 Portrait of LHC

LHC will provide proton-proton collisions with a center of mass energy ($\sqrt{s}$) of 14 TeV and a luminosity of 10^{34} cm^{-2} s^{-1}. The luminosity (*L*) is the parameter that connect the rate of events *R* (number of events per unit of time) and the interaction cross section σ:

$$R = L \times \sigma \qquad (1.1)$$

Luminosity depends on the machine parameters:

$$L = (f\, n_1\, n_2)/(4\pi\, \sigma_x\, \sigma_y) \qquad (1.2)$$

with *f* the particle bunches collision frequency, n_1 and n_2 are the numbers of particles in the two colliding bunch and σ_x and σ_y are the parameters which characterize the beam profile in the horizontal (bending) and in the vertical direction respectively.

The high luminosity will compensate the small cross section of interesting interactions. LHC will also provide heavy ion collision (Pb-Pb) at center of mass energy of about 5.5 TeV per nucleon.

The protons will be accelerated initially by the existing system on accelerators already working for LEP: Linac2, PS Booster, PS and SPS. The protons will be grouped in packages of about 10^{11} particles, and they will be injected in LHC with an energy of 450 GeV. There will be 2835 bunches of protons circulating in the 27 km long vacuum pipe of LHC.

The limitng factor to the achievable center of mass energy is the bending

power needed to keep the beams circulating; from the equation

$$p = 0.3\,B \cdot R \,, \qquad\qquad (1.3)$$

where p is the beam momentum (TeV), B the magnetic fields provided by the magnets (T) and R the radius of the LEP ring (km), the magnetic field needed to achieve a beam momentum of 7 TeV is about 5.4 Tesla. Practically it is impossible to completely cover the machine with magnets, so the 1200 superconductive dipole magnets operating with superfluid helium at 1.8 K provide a magnetic field of 8.3 T. There are two separate beam lines, because LHC accelerates equally charged particles in opposite directions.

At LHC will occur a bunch crossing every 25 ns; the total proton-proton cross section at 14 TeV is 80 mb, so the interaction rate is 10^9 events/s. When an hard scattering is produced during a bunch crossing, this event is overlapped with 25 additional soft events (pile-up); therefore, LHC detectors need a fast response time (in the range of $20\div50$ ns, which correspond to integrate over 1-2 bunch crossing) and a fine granularity to minimize pile-up. Also, due to high particle flux coming from p-p collision, LHC detectors need to be resistant to radiation.

LHC will constitute a factory of all the Standard Model particles, as well of new particles in the TeV. However, its main drawbacks will be QCD background and pile-up events: the event rate at LHC is dominated by QCD jet production, because QCD cross section grow faster with the center of mass energy than the electroweak one, hence the signal-background ratios are very low.

There will be two general purpose experiments (ATLAS and CMS) and two specialized ones (LHCb and ALICE) that will operate at four interaction points of LHC.

The **CMS** experiment (Compact Muon Solenoid)[10] is based on a single, large superconducting solenoidal magnet generating a uniform magnetic field at 4 T. The inner detector contains silicon pixel and multi-strip gas chambers. The electromagnetic calorimeter is made of lead tungstate crystals; the hadronic calorimeter uses plastic scintillating tiles. Drift chambers, installed in the barrel, and cathode strip chambers, in the end-cap regions, are used for muon tracking. Drift chambers are auto-triggering, but trigger information is provided also by resistive plate chambers.

LHCb[8] is a dedicated b-physics experiment. It is a open geometry forward collider detector which is designed to fully exploit the b physics potential of LHC. The large Lorentz boost of accepted b-mesons allows precise decay time measurements which are completed by excellent particle information and efficient triggers.

ALICE[9] will investigate Pb-Pb collisions. This heavy-ion detector will study the behavior of strongly interacting matter at very high energies and densities, and in particular it will explore the formation of quark-gluon plasma.

The **ATLAS** detector will be described in the next sections.

1.3 The ATLAS detector

The ATLAS (**A T**oroidal **L**hc **A**pparatu**S**) detector is a general purpose detector[11][12][13]; it is sensible to a largest possible spectrum of massive particles to maximize the potential for the discovery of new physics. The detector was designed to exploit the full potential of LHC. This goal implies several requests to the detector design:

- Large acceptance and maximum coverage in pseudorapidity[1] η with almost full azimuthal angle ϕ.
- Possibility to trigger and measure particles at low p_T thresholds.
- Good electromagnetic calorimetry for electron and photon
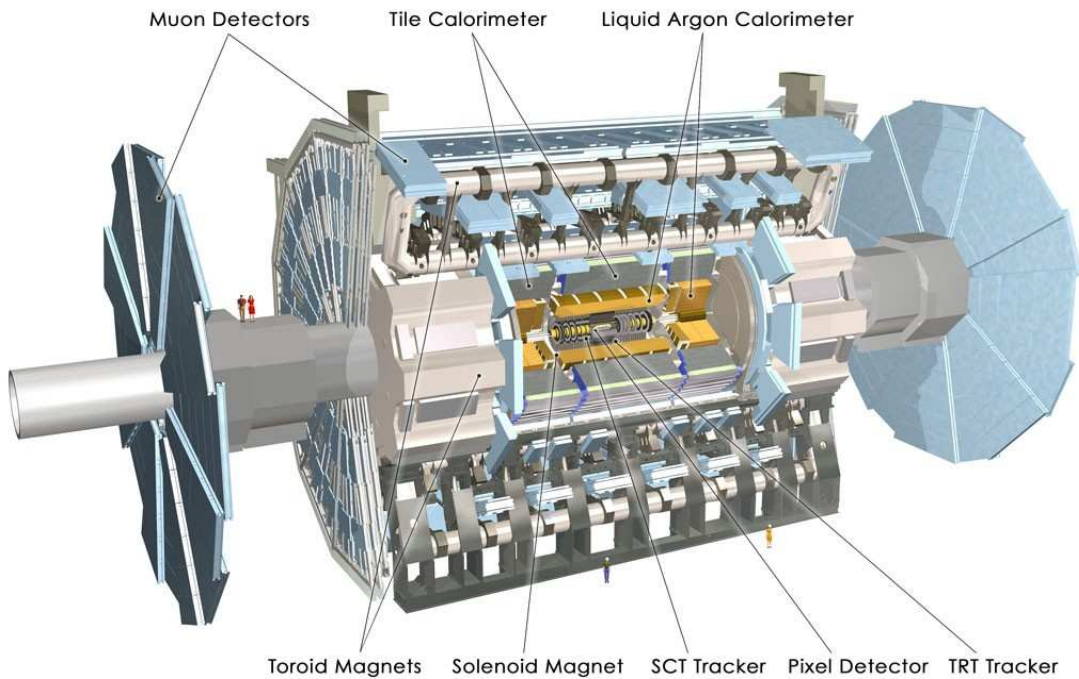
Fig. 1.2: The ATLAS detector.

---

[1] The ATLAS conventional coordinate system is right- handed and has the *x*-axis pointing form the interaction point to the center of the LHC ring, the *z*-axis directed along the tunnel and the *y*-axis pointing from the interaction point upward. Given the symmetry of the detector, a system of cylindrical coordinates (*z*, ϕ, ζ) is used. Instead of the polar angle theta, the *pseudorapidity* η, defined as

$$\eta = -\ln(\tan(\zeta/2))$$

is more commonly used. In this reference system, the transversal momentum is $p_T = \sqrt{(p_x^2 + p_y^2)}$

identification and measurements, and hermetic jet and E_T missing hadronic calorimetry

- Efficient tracking at high luminosity for the measurement of lepton momentum, for *b*-quark tagging and for enhanced electrons and photon identification, as well as tau and heavy-flavour vertexing and reconstruction capability of some B-decay final state at lower luminosity.

- Stand-alone high precision muon momentum measurements up to highest luminosity.

The ATLAS detector is a cylinder of 42 m total length and 11 m radius, and it has the traditional onion shell structure used in collider experiments (see Figure 1.2).

1.3.1 Magnetic Field

The ATLAS detector presents a magnetic system composed by a central superconducting solenoid (CS) surrounding the Inner Detector cavity and a large superconducting air-core toroid made of independent coils arranged with an eight fold symmetry outside the Calorimeters as a part of the Muon Spectrometer[14][15][16][17].

The CS operates at 4.5 K and it creates a magnetic field of 2 T parallel to the beam axis in the inner part of the detector. The field is quite homogeneous in the barrel section, but decrease rapidly with *z* in the end cap region. The solenoid coil is integrated into the vacuum vessel of the LAr Calorimeter barrel cryostat, in order to minimize the material before it and avoid that particles start showering before they reach the Calorimeters.

The toroidal magnet system in the Muon System bends charged particles in the *R* - *z* plane and it is composed of three parts: the two End Cap Toroids (ECTs) and the Barrel Toroid (BT). Each of the three toroids consists of eight coils assembled radially and symmetrically around the beam axis. The barrel toroid has a length of 25 m, with an inner bore of 9.4 m and an outer diameter of 20.1 m. The coil caps have a length of 5 m, an inner bore of 1.64 m and an outer diameter of 10.7 m. The ECT coils are rotated by 22.5° with respect to the BT coil system in order to provide radial overlap and to optimize the bending power in the transition region of both coil systems. The toroidal design of the muon magnet system has an open structure to minimize the contribution of multiple scattering to the momentum resolution; moreover, the bending increases with higher pseudorapidities, because the particles cross all the η range almost perpendicular to the field lines.

The performance in terms of bending power is characterized by the field integral $\int B \, dl$ where *B* is the azimuthal field component and the integral is
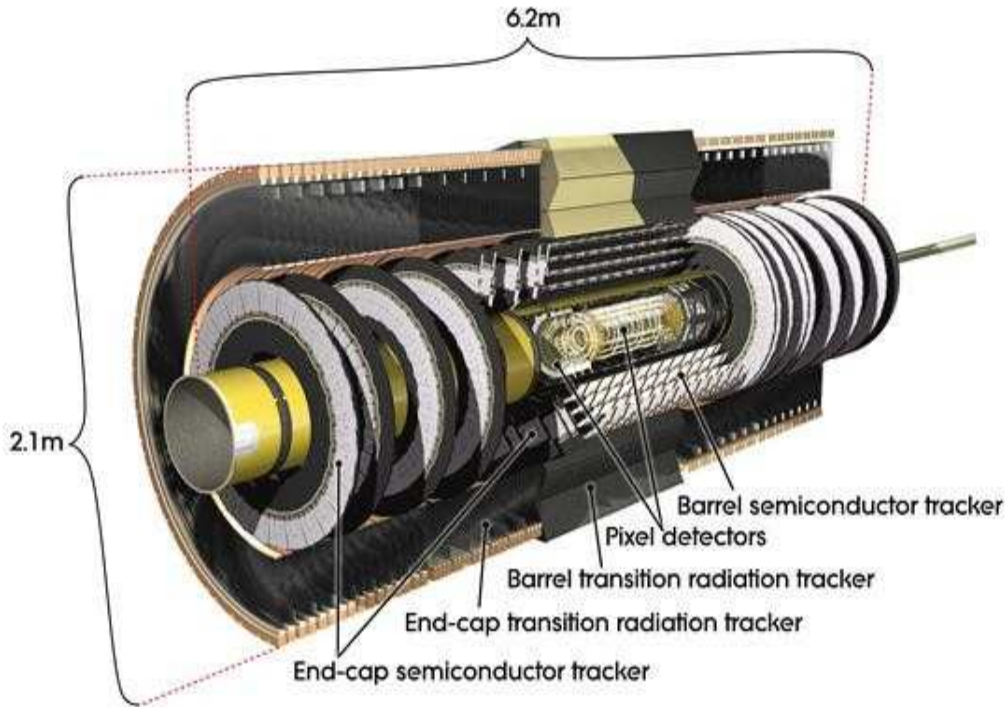
Fig. 1.3: The ATLAS Inner Detector

taken on a straight line trajectory between the inner and the outer radius of the toroids. The BT provides to 2 Tm ÷ 6 Tm in the range $|\eta|$<1.3 and the two ECT contribute with 4 Tm ÷ 8 Tm in the range 1.6<$|\eta|$<2.7. The toroidal magnet provides a peak field of 3.9 T in the barrel and 4.1 T in the end-cap. A disadvantage of this configuration is the presence of region with highly non-uniform field, especially in the transition regions, where the bending power is lower.

1.3.2 Inner Detector

The Inner Detector (ID)[18][19] is sited in the most inner part of the Atlas detector, and it is the closest part to the beam line (see Figure 1.3). The main purpose of the Inner Detector is the reconstruction of tracks and vertexes with a high efficiency. For this reason, it has to perform momentum measurements in a broad momentum range (in particular below a p_T of 0.5 GeV particles loop in the magnetic field, and a reconstruction is not possible using only the Electromagnetic Calorimeter) to discriminate between electrons and photons and to perform a good identification of particles in dense jets (where the Calorimeter cannot resolve them).

The ID is contained in the solenoid magnet; its outer radius is 115 cm and its length is 6.7 m. The ID is divided into three parts: the Pixel detector, the

Semi-Conductor tracker (SCT) and the Transition radiation tracker (TRT).

The *Pixel Detector* is composed by three barrel layers of 140 millions of silicon pixels, with a size of 50 μm in $R − \phi$ and 300 μm in z. On each side there are five disks, with a radius between 11 and 20 cm, which complete angular coverage. The design resolution of the Pixel detector is $\sigma_{R\text{-}\phi} = 12$ μm and $\sigma_z = 60$ μm. The fine granularity assures a good performance even with the expected high track densities and the high resolution allows to reconstruct secondary decay vertexes.

The *SCT* consists in eighty layers of silicon strip detectors. They are arranged in pairs and rotated of a stereo angle of 40 mrad respect each other. The strips in the barrel have pitch of 80 μm and a length of 12.8 cm, while in the end cap, to obtain an optimal coverage in η, the length is between 6 and 12 cm and the pitch varies with an average size of 85 μm. This configuration provides precision measurements in the z coordinate in the barrel, with a resolution of $\sigma_z = 580$ μm and $\sigma_{R\text{-}\phi} = 18$ μm

The *TRT* is the outer part of the ID, and it is composed by 420000 proportional drift tubes placed in layers along z in the barrel and in wheels radially in the cap. The tubes have a diameter of 4 mm and operate with a non flammable mixture of Xe, CF_4 and CO_2, optimized for the detection of X-ray, that are produced by transition radiation. It is possible to use the TRT to discriminate between tracking hits (only lower threshold) and transition-radiation hits (both thresholds) using two different discriminators. The single-wire resolution for tracking hits is about 170 μm and even for the highest rates it is expected an efficiency greater than 50%.

1.3.3 Calorimeters

The Calorimeters system[20][21][22] is required to measure the energy and direction of photons, electrons, isolated hadrons and jets, as well missing transverse energy. The Calorimetry consists of an Electromagnetic Calorimeter (ECAL), a Hadronic barrel Calorimeter, two Hadronic end-cup Calorimeters and Forward Calorimeters, covering the pseudorapidity regions of ($|\eta|$<3.2, $|\eta|$<1.6, 1.5<$|\eta|$<3.2 and 3.2<$|\eta|$<4.9 respectively (Figure 1.4).

The *Electromagnetic Calorimeter* of the ATLAS detector has many significative features: good electron reconstruction capacity from 1 GeV ÷ 2 GeV to 5 TeV, very good resolution over the range 1 GeV ÷ 300 GeV, good resolution in pseudorapidity measurement of the showers, very good photon/photon-jet, electron/electron-jet and tau/tau-jet separation. It is a Lead Liquid Argon sampling calorimeter with accordion shaped Kapton electrodes and lead absorber plates over its full coverage: this geometry provides complete ϕ symmetry, without azimuthal cracks; it is divided into barrel part
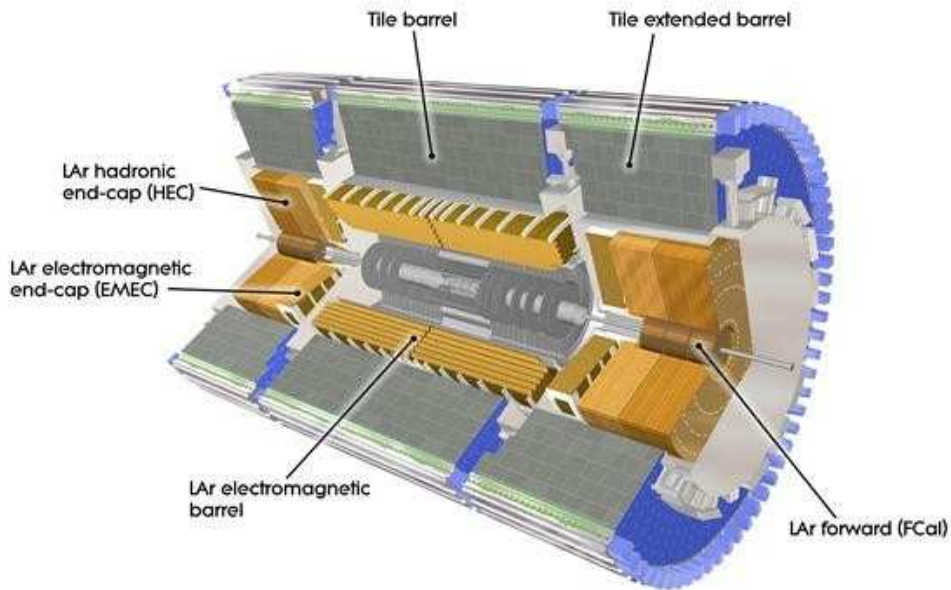
Fig. 1.4: The ATLAS calorimetric system

and two end caps. A barrel cryostat around the inner cavity contains the barrel part and the solenoid coil, while two end-caps cryostat enclose the Electromagnetic end-caps Calorimeters. The lead thickness in the absorber plates has been optimized as a function of η in terms of EM Calorimeter performance in energy resolution. The LAr sampling technique is radiation resistant, and provides long term stability of the detector response, excellent hermeticity, good energy resolutions, and relatively easy detector calibration. The EM Calorimeter thickness is more than 24 X_0 (radiation lengths) in the barrel and 26 X_0 in the end-caps; the segmentation is $\Delta\eta \times \Delta\phi = 0.025 \times 0.025$. For a correction of the energy loss in the material in front of the ECAL (ID, cryostat, coil) the Calorimeter is preceded in the region of $|\eta|<1.8$ by a pre-sample detector, which consists of an active LAr layer. In the $1.0<|\eta|<1.6$ region there is, additionally, a scintillator slab used for the same purpose.

The energy resolution of the ECAL is $\Delta E/E = 10\%/\sqrt{E} + 1\%$ (E in GeV). The measurement resolution of the the shower direction will be about 50 mrad $/\sqrt{E}$ (E in GeV).

The main features of the *Hadronic Calorimeter* are: jet direction capability which has to go up to $|\eta| \cong 5$, good resolution in jet reconstruction, jet-jet mass reconstruction. To best suit the requirements and to cope with the radiation environment different techniques and devices are used. Thickness is an important parameter in the design of the Hadronic Calorimeter, because it has to provide good containment for hadronic showers and reduce punch-

trough into the muon system to a minimum. The total thickness is 11 λ (interaction lengths) at $\eta = 0$.

In the $|\eta|<1.6$ a sampling Calorimeter is used with iron as an absorber material and scintillating tiles (3 mm thick) as active material (Tile Calorimeter). The signals on both sides produced by the scintillating tiles are read out by wavelength-shifting fibers into two separate photomultipliers. The resulting segmentation of the Hadron Calorimeter is $\Delta\eta \times \Delta_\phi = 0.1 \times 0.1$.

In the end-cap range of $1.5<|\eta|<4.9$ a hadronic LAr Calorimeter is used. The end-cap Hadronic Calorimeter extends up to $|\eta|<3.2$ and it is a copper-LAr detector with parallel plate geometry. The high density Forward Calorimeter covers the region of $3.2<|\eta|<4.9$, its front face is placed at about 5 m from the interaction point; it is moved out by 12 m with respect to the ECAL in order to reduce the number of backscattered neutrons into the ID. It is a dense LAr Calorimeter with rod-shaped electrodes in a metal matrix; it is composed by three sections: the first is made of copper while the other two are made of tungsten. Each section consists of a metal matrix with regularly spaced longitudinal channels filled with concentric rods and tubes: both matrix and tubes are grounded, while the rods are at positive high voltage. The sensitive medium is the LAr in the gap between them.

The expected energy resolution for the Hadronic Calorimeter is $\Delta E/E = 50\%/\sqrt{E} + 3\%$ (E in GeV) for $|\eta|<3$ and $\Delta E/E = 100\% /\sqrt{E} + 10\%$ (E in GeV) for $3<|\eta|<4.9$.

1.3.4 Muon Spectrometer

The Muon Spectrometer[23] by volume is the main part of the ATLAS detector. It is instrumented with separate trigger and high precision tracking chambers. The main purpose of the Muon Spectrometer is the measurement of the muon momentum by means of the deflection of muon tracks in large superconductive air-core toroid magnets. A large barrel magnet provides the magnetic bending for $|\eta|<1.0$, while for $1.4<|\eta|<2.7$, muon tracks are bent by the two smaller end-caps magnets inserted into both ends of the barrel toroid (Figures 1.5 and 1.6). The region for $1.0<|\eta|<1.4$ is usually called transition region; here magnetic deflection is provided by a combination of barrel and end-cap fields. The precision measurement of the muon tracks is made by R-z projection; the z coordinate is measured in the barrel, while the R coordinate is measured in the transition and end-cap regions.

In the barrel region ($0<|\eta|<1.0$) muon tracks are measured in chambers arranged in three cylindrical layers (stations) concentric to the beam axis, with a 5 m, 7,5 m and 10 m radium respectively (inner, middle and outer stations).
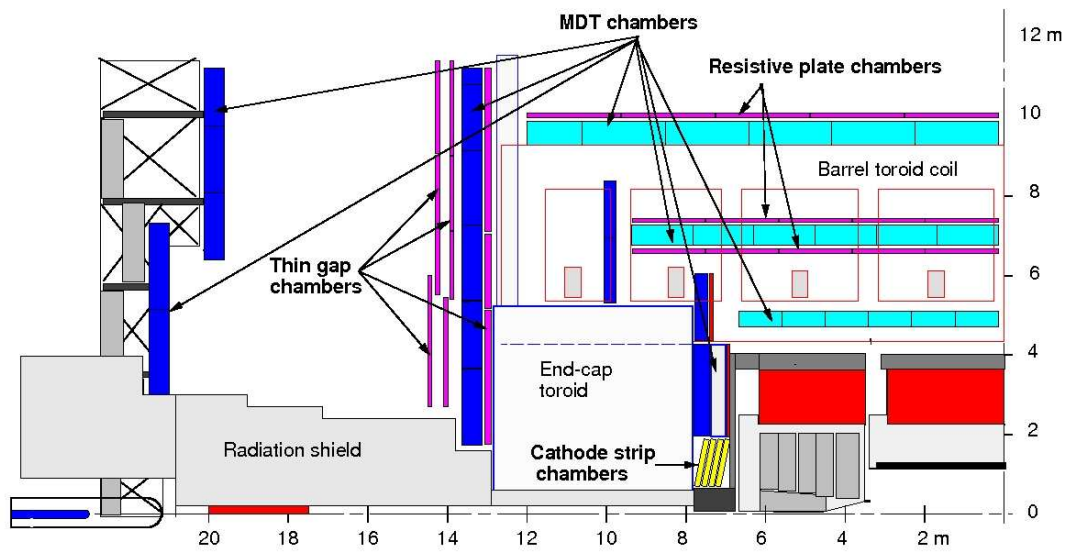
Fig. 1.5: Profile of the MuonSpectrometer in the *yz*-plane.
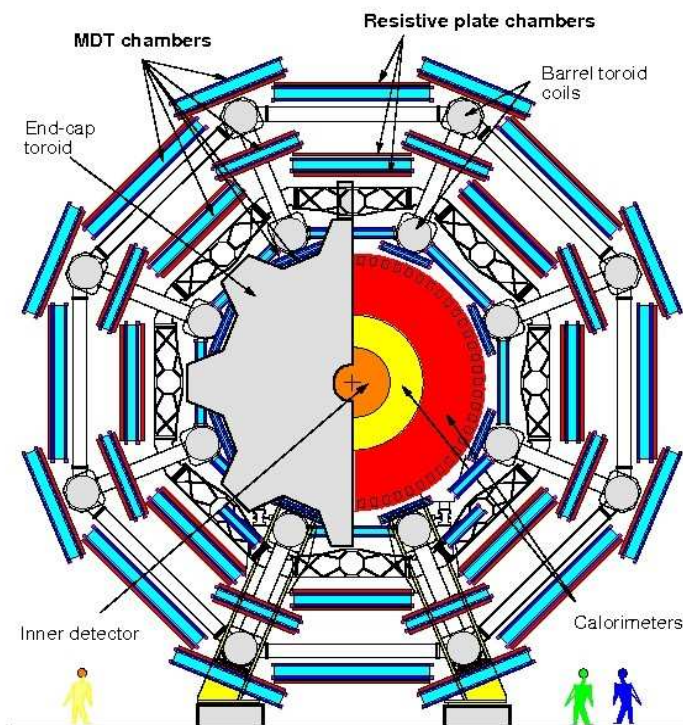

Fig. 1.6: Profile of the Muon Spectrometer in the
xy-plane.

Chapter 1 – LHC and the ATLAS experiment

In this region particles are measured near the inner and outer field boundaries and inside the filled volume in order to determine the momentum from their sagitta. In the end-cap region (1.0<|η|<2.7) the chambers are arranged into fours disks at 7 m, 10 m, 14 m and 21-23 m from the beam interaction point. The barrel chambers are rectangular, while the end-cap chambers have trapezoidal shape. Both in the barrel and in the end-caps, a 16-fold segmentation in azimuth has been chosen to follow the eightfold azimuthal symmetry of the magnet structure. The chambers are arranged in large and small sectors; the large sectors cover the regions between the barrel toroid coils, while the small sectors cover the azimuthal range around the Barrel Toroidal Coils. In two lower barrel sectors rails carrying the Calorimeter, and their feet require ad hoc shaped chambers to maximize the acceptance. There is also an opening in the central R-ϕ plane, for the passage of cables ad services to the Inner Detector, the Central Solenoid and the Calorimeters.

The Muon Spectrometer chambers employ four different kinds of technologies: Monitored Drift Tube Chambers (MDTs) and Cathode Strip Chambers (CSCs) are precision chambers, while Resistive Plate Chambers (RPCs) and Thin Gap Chambers (TGCs) are trigger devices. The MDTs give the precision measurements of the muon tracks in the main bending direction of the magnetic field and they aren't used only in the inner ring of the end cap inner station (2.0<|η|<2.7) where, due to the proximity of the beam line, a high density of tracks is expected and CSCs are employed instead. In the barrel RPCs are used as trigger devices for bunch-crossing identification and for the measurement of the second coordinate. They are located on both sides of the middle MDT station and above or directly below the outer MDT station. In the end-caps, near the middle MDT station TGCs are located to provide the trigger information.

In the design of the spectrometer instrumentation a major impact came form the high level of particle fluxes, as it affects required performance parameters such as rate capability, granularity, ageing properties and radiation hardness. Trigger and reconstruction algorithms are optimized to cope with the difficult background conditions resulting from penetrating primary collision productions and from radiation background, mostly neutrons and photons in the 1 MeV range, produced from secondary interactions in the Calorimeters, shielding material, beam pipe and LHC machines elements. There are many necessary performance for the Muon Spectrometer: transverse momentum resolution constant over the full rapidity range at level of few percent for low p_T is required in order to reconstruct narrow two or four muon final state on top of a high background level, with a 10% value for p_T = 1 TeV; for safe track reconstruction and reliable momentum determination measurement of muon in the non bending projection has to be with a r.m.s. spatial resolution of 5 mm ÷ 10 mm; to reach a good coverage (upon η = 3) and good hermeticity

for all the physics channel a wide rapidity coverage is required; transverse momentum threshold has to be of 10 GeV ÷ 20 GeV for high mass states (lower thresholds of 5 GeV are required for CP violation and beauty physics); a trigger capability for almost all physical channels is required.

Monitored Drift Tube Chambers

The MDT chambers are built on a basic element, the drift tube, an aluminum tube filled with gas. It has an outer diameter of 3 cm, a thickness of 0.4 mm, a length between 70 cm and 630 cm. A anodic central gold plated W-Re wire is placed inside the tube. The tubes are full of a mixture of 93% Ar and 7% CO_2 at 3 bar absolute pressure. A muon crossing the MDT ionize the gas along its track; the produced electrons drift towards the wire in the electric field and are multiplied in an avalanche process close the wire (due to the high field). The signal read at the end of the tube is the current induced on the wire; it is read by a low-impedance current sensitive preamplifier, followed by a differential amplifier and a discriminator. The output of the shaping amplifier is connected to a simple ADC, to correct the drift-time measurement for time-slewing using the charge-integrated signal; then the corrected signal is converted into a distance using the *r-t* relation of the mixture. The chosen mixture provides a non linear space time relation, with a maximum drift-time of 700 ns, a small Lorentz angle and excellent ageing properties. The average spatial resolution of a single tube is expected around 80 μm.

In the MDT tubes are arranged in 2 multilayers of three or four layer, respectively in the middle and outer stations and in the inner station. This structure permits an accurate relative positioning of the tubes and mechanical integrity under the effects of gravity and temperature. Wires and tubes have been assembled with a precision of 20 μm. Moreover an excellent optical alignment system is required in order to achieve the desiderate high transverse momentum resolution[24]; it has to monitor the position of the chambers with a precision of 30 μm. The system is used both for checking the in-chamber deformation and the relative displacement of the chambers. Temperature sensors are used in order to monitor chamber thermal expansion. The spacer frames support most of the components of the optical alignment system; however, in the end-caps, the alignment system makes use of an additional bar system.

Cathode Strip Chambers

The CSCs are multiwire proportional chambers with cathode strip readout. The anode wire pitch is 2.54 mm and cathode readout pitch is 5.08 mm. They are arranged in 2×4 layers, and they contain a non flammable mixture of Ar (30%),

CO_2 (50%) and CF_4 (20%). A good spatial resolution (60 μm) is achieved by charge interpolation between neighboring stripes. The cathode strips for the precision measurement are orthogonal to the anode wires. From strips oriented parallel to the anode wires a measurement of the transverse coordinate is obtained. The CSCs have a small electron drift time resolution (7 ns), good two-track resolution and low neutron sensitivity.

Resistive Plate Chambers.

The RPCs are located in the barrel region. The basic RPC unit is a narrow gas gap formed by two parallel resistive bakelite plates with a thickness of 2 mm, separated by 2 mm thick polycarbonate spacers, which define the size of the gap. The gap is full of a mixture based on tetrafluorethane ($C_2H_2F_4$), with some admixture of SF_6, to allow a relatively low operating voltage. The primary ionization electrons are multiplied into avalanches by a high electric field; the signal is read through capacitive coupling by metal strips on both sides of the detector.

A RPC trigger chamber consists of two rectangular detector layers, each one read out by two orthogonal series of pick-up strips; the η stripes are parallel to the MDT wires and provide the bending view of the trigger detector, the ϕ stripes are orthogonal to the MDT and provide the second-coordinate measurement.

Thin Gap Chambers

The TGCs are similar to multiwire proportional chambers, with a larger anode wire pitch. The signals from the anode wires that are arranged parallel to the MDT wires provide the trigger information together with readout strips arranged orthogonal to the wires. These readout strips are also used to measure the second coordinate. The gas employed is a high quenched gas mixture of 55% CO_2 and 45 % of n-pentane (n – C_5H_{12}). The electric field configuration and the small wire distance provide for a short drift time and thus a good time resolution. TGS are arranged in doublets and triplets of chambers. The inner station consists of one doublets and it is only used to measure the second coordinate. The seven chambers layers in the middle station are arranged in one triplet and one doublet which provide the trigger and the second coordinate measurement. The anode plane is sandwiched between two cathode planes made of 1.6 mm G10 plates. On the center plane of the chamber etched copper strips provide the readout of the azimuthal coordinate; no readout strips are foreseen for the central layer of the triplet.

1.3.5 The Trigger Scheme

In LHC a bunch cross rate of 40 MHz and an interaction rate of 10^9 Hz are foreseen. A rate of 100 Hz is the technical-economical limit to permanently store data from events, thus for a detector working at LHC trigger and data acquisition (DAQ)[25][26] system are crucial; the task of the trigger is to reduce the huge interaction rate to 100 Hz of interesting events.

A trigger signal is a fast signal, generated every time an event of interest occurs in the detector. When conditions predicted by the characteristic of interesting events are satisfied through the trigger algorithm, the data taking starts. The ATLAS trigger scheme is based on three levels: LVL1, LVL2 and EF (Event Filter). Each step take in account more and more refined informations and it can work at a lower rate. The LVL2 and the EF are referred as High Level Trigger (HLT) system, and they share the overall trigger selection framework, differing mostly in the amount of data they can access.

At the first level, only data from the Calorimeters and the Muon System are used; they are quickly analyzed to derive an accept or reject decision. The LVL1 trigger accepts data at the full LHC bunch-crossing rate of 40 MHz. The LVL1 muon trigger has been designed to supply muons, which have a transverse momentum above a threshold of 6 GeV for low energy muons and 20 GeV for high energy muons; this is accomplished using the muon trigger chambers, RPC in the barrel and TGC in the end-caps. In the barrel region, low-p_T trigger is based on the two innermost RPC layers: the reference RPC layer (pivot station, which is the layer located immediately above the middle MDT chamber) and the layer located immediately below the middle MDT chamber (low-p_T coincidence planes). In both the R-z and R-ϕ projections, a coincidence in three out four strip planes is required. In the end-caps, the same trigger is realized using TGCs, by a three out of four coincidence in the two outermost layers. Both triggers can be extended to become high-p_T trigger: in the barrel it is required an additional hit in each projection in layer located immediately above the outer MDT chamber (high p_T coincidence planes); in the end-cap two of three coincidences in the bending plane of the triplet of the innermost TGC chamber plus one of the two coincidence in its azimuthal strip planes are required. The Calorimetry selections are based on reduced-granularity information from all the calorimeters. The objects searched for by the calorimeters are isolated electromagnetic clusters with transverse energy above 30 GeV, high energy hadronic jets and large missing transverse energy.

The essential requirement of the LVL1 is to identify the interesting bunch crossing and provide the Region of Interest (RoI) for the other trigger levels; RoI data contain information about position, p_T of candidate objects, deposited energy from a small fraction of the detector, corresponding to delimited regions centered on the objects indicated by the LVL1 trigger.

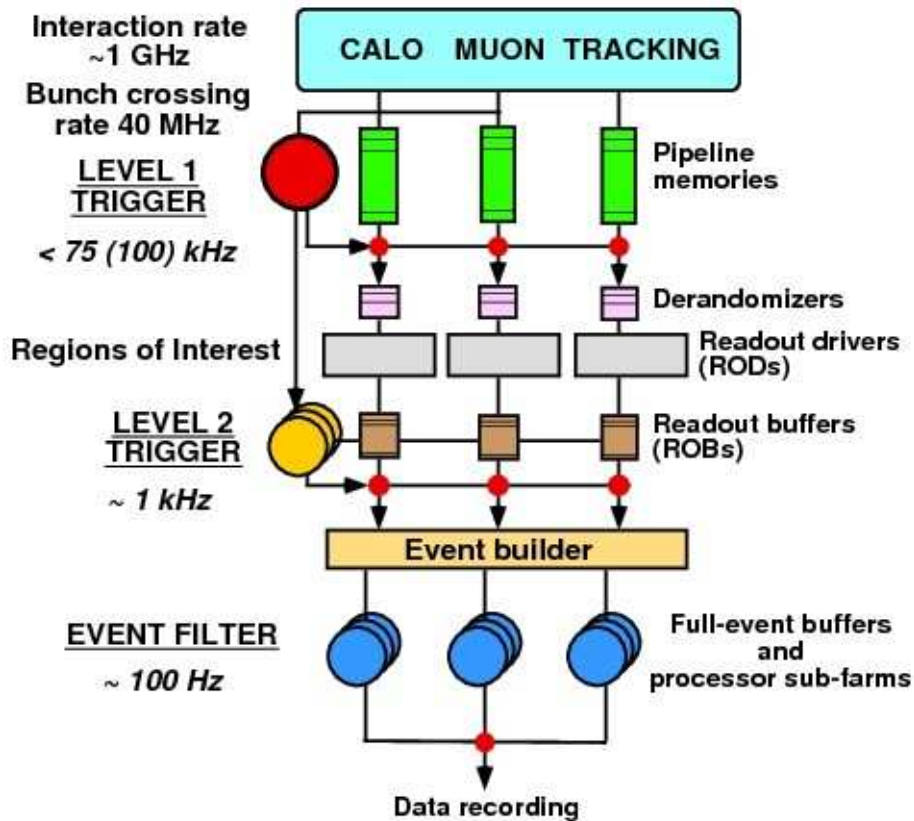The LVL2 trigger analyze the RoI data across different detector and

Fig. 1.7: Overview of the trigger system of ATLAS

provides a refined analysis of the LVL1 trigger. The Inner Detector is involved in the LVL2 trigger. For the isolated electron trigger, the ID searches for track pointing towards the cluster. It is expected for the LVL2 trigger to reduce the rate from 75 kHz to around 1kHz, which is the highest acceptable rate for the EF trigger.

The Event Filter makes the final selections of physics events that will be written to mass storage for the full offline analysis. At this stage a complete reconstruction of the event is possible. The EF will employ offline algorithms and methods, adapted to the on-line environment, and it will use the calibration and alignment information as well as the magnetic field map. The output rate should be reduced by an order of magnitude, giving more or less 100 Hz.

A summary of ATLAS trigger scheme is shown in Figure 1.7.

Chapter 2

The standard model and the *W*, *Z* and Higgs boson production at LHC

In this chapter I give a short introduction to *W* and *Z*, the vector bosons of electroweak interaction, and to the Higgs Boson, necessary in the Standard Model to give mass to the particles. In section 2.1 I will briefly describe the Standard Model of electroweak interations and the spontaneous symmetry breaking mechanism. In section 2.2 I will illustrate the main channels of production and decay for the described particles.

2.1 The Standard Model of Electroweak Interactions

The present belief in the theoretical physics is that all the particle interactions can be dictated by local gauge symmetries; this is connected to the idea that physical conserved quantities are conserved in local regions of space and not just globally.

The connection between symmetries and conservation laws is best discussed in the framework of the Lagrangian field theory. A Lagrangian is called symmetric under a transformation if the equation describing the behavior of the particles is invariant under that transformation.

The electroweak theory[27] incorporates the electromagnetic interactions with a weak interactions theory and it is described adding to the $SU(2)_T$ gauge symmetry, suggested by the existence of left handed weak isospin doublets, a $U(1)_Y$ weak-hypercharged phase symmetry.

To simplify the description of the theory, one can construct an

electroweak theory applied only to the first generation leptons, e^- and ν_e. While electrons can be left and right-handed, neutrinos are found in experiments to exist only as left-handed particles: it is possible to define a left-handed weak isospin doublet L, with weak-isospin $T = \frac{1}{2}$ and weak hypercharge $Y = -1$ and a right-handed weak isospin singlet R, with weak-isospin $T = 0$ and weak hypercharge $Y = -2$.

$$L = \begin{pmatrix} \nu \\ e^- \end{pmatrix}_L \qquad\qquad R = e^-_R$$

The electroweak gauge group $SU(2)_T \times U(1)_Y$ implies two sets of massless gauge fields: a weak isovector B^i_μ with coupling constant g for $SU(2)_T$ and a weak isoscalar a_μ with coupling constant g' for $U(1)_Y$.

The Lagrangian of the system can be written as

$$\mathcal{L} = \mathcal{L}_G + \mathcal{L}_F + \mathcal{L}_S + \mathcal{L}_{YK} \qquad (2.1)$$

where the terms or the Lagrangian are

- $\mathcal{L}_G = -\dfrac{1}{4} F_a^{\mu\nu} F_{a\mu\nu} - \dfrac{1}{4} f^{\mu\nu} f_{\mu\nu}$

  with $a = 1, 2, 3$ which is the Lagrangian of the free massless gauge fields. In this Lagrangian

  $$F_a^{\mu\nu} = \partial_\mu B^a_\mu - \partial_\nu B^a_\mu + g \epsilon^a_{bc} B^b_\mu B^c_\nu$$
  $$(2.2)$$
  $$f_{\mu\nu} = \partial_\mu a_\nu - \partial_\nu a_\mu.$$

- $\mathcal{L}_F = \bar{R} i \gamma^\mu \left(\partial_\mu + \dfrac{i}{2} g' Y a_\mu \right) R + \bar{L} i \gamma^\mu \left(\partial_\mu + \dfrac{i}{2} g' Y a_\mu + \dfrac{i}{2} g \vec{T} \cdot \vec{B}_\mu \right) L$

  which is the Lagrangian of the free massless fermionic fields.

- $\mathcal{L}_S = (D_\mu \phi)^\dagger (D^\mu \phi) - \mu^2 (\phi^\dagger \phi) - \lambda (\phi^\dagger \phi)^2$

  which is the Lagrangian of the scalar fields necessary to symmetry breaking and to give masses to the gauge bosons and to the fermions.

- $\mathcal{L}_{YK} = -G_e \left[\bar{R} \left(\phi^e L \right) + \left(\bar{L} \phi \right) R \right]$

  is the Yukawa Lagrangian, and it express the coupling between massless fermionic fields and the scalar fields ϕ.

The field ϕ is a doublet of scalar fields of hypercharge $Y = 1$:

$$\phi = \begin{pmatrix} \phi^+ \\ \phi^0 \end{pmatrix} \quad \text{with} \quad \phi^+ = \frac{1}{\sqrt{2}}(\phi_1 + i\phi_2) \quad \text{and} \quad \phi^0 = \frac{1}{\sqrt{2}}(\phi_3 + i\phi_4)$$

The gauge-covariant derivative D_μ is:

$$D_\mu = \partial_\mu + \frac{i}{2}g'Ya_\mu + \frac{i}{2}g'\vec{T}\cdot\vec{B}_\mu \qquad (2.3)$$

with $\quad Y = \begin{pmatrix} 1 & 0 \\ 0 & 1 \end{pmatrix}, \; T_1 = \begin{pmatrix} 0 & 1 \\ 1 & 0 \end{pmatrix}, \; T_2 = \begin{pmatrix} 0 & -i \\ -i & 0 \end{pmatrix}, \; T_3 = \begin{pmatrix} 1 & 0 \\ 0 & -1 \end{pmatrix}.$

This Lagrangian is invariant under local transformation of the group U(1). While λ in the $\mathcal{L}_S$ term needs to be positive to ensure an inferior limit for the potential term, for μ^2 there are two possible situations:

1) $\mu^2 > 0$, the potential has a parabolic shape, and it has a unique point of minimum, $\phi = 0$. This uniqueness ensure that the symmetry cannot be broken and in this way a massless gauge boson is obtained.

2) $\mu^2 < 0$, the potential has a relative maximum for $\phi = 0$ and an infinite set of minimum points, in correspondence of

$$|\phi| = \sqrt{\frac{-\mu^2}{2\lambda}}. \qquad (2.4)$$

(as depicted in Figure 2.1)

The choice of a minimum over the infinite possible set break the symmetry: all these minimum configurations are connected by gauge transformations, that change the phase of the ϕ field, and when the system
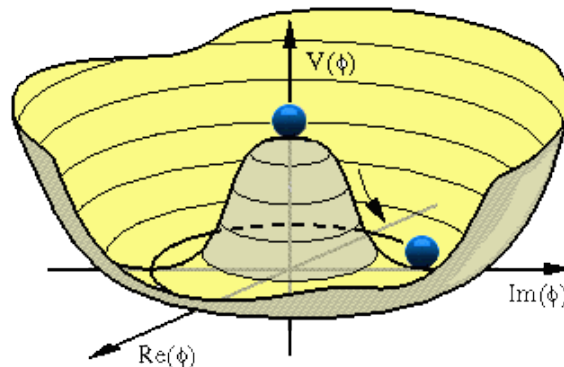

Fig. 2.1: The potential
V(ϕ) = μ^2 ($\phi^\dagger\phi$) +λ ($\phi^\dagger\phi$)^2 for μ^2<0

choose one of the minimum configurations, this is no longer symmetric under the gauge symmetry. This mechanism is called spontaneous symmetry breaking.

The field can be parametrized near to the vacuum field chosen. All the possible minimum are equivalent (under a gauge transformation) so it can be chosen

$$\phi_0 = \begin{pmatrix} 0 \\ \dfrac{\upsilon}{\sqrt{2}} \end{pmatrix} \quad \text{with} \quad \upsilon = \sqrt{-\dfrac{\mu^2}{\lambda}}.$$

The parametrized field is

$$\phi(x) = \begin{pmatrix} 0 \\ \dfrac{\upsilon + \eta(x)}{\sqrt{2}} \end{pmatrix} \exp\left[\dfrac{i\vec{T}\cdot\vec{\xi}(x)}{2\upsilon} \right]; \quad (2.5)$$

the $\xi(x)$ variations corresponds to oscillations in the minimum, and it is a massless scalar field called *Goldstone boson*. It is possible to eliminate the Goldstone boson using the following gauge transformation:

$$\phi(x) \rightarrow \phi'(x) = \exp\left[-\dfrac{i\vec{T}\cdot\vec{\xi}(x)}{2\upsilon} \right] \phi(x) = \begin{pmatrix} 0 \\ \dfrac{\upsilon + \eta(x)}{\sqrt{2}} \end{pmatrix} \quad (2.6)$$

$$a_\mu \rightarrow a'_\mu \quad (2.7)$$

$$B^i_\mu \rightarrow B'^i_\mu \quad (2.8)$$

The terms $D^\mu \phi$ of the Lagrangian becomes now, omitting the apex for simplicity,

$$
\begin{aligned}
D^\mu \phi \quad &= \quad \left(\partial^\mu + i\dfrac{g'}{2} Y a^\mu + i\dfrac{g}{2} \vec{T}\cdot\vec{B}^\mu \right) \begin{pmatrix} 0 \\ \dfrac{\upsilon + \eta}{\sqrt{2}} \end{pmatrix} = \\
&= \begin{pmatrix} 0 \\ \dfrac{\partial_\mu \eta}{\sqrt{2}} \end{pmatrix} + i \left(\dfrac{g'}{2} Y a^\mu + \dfrac{g}{2} \vec{T}\cdot\vec{B}^\mu \right) \begin{pmatrix} 0 \\ \dfrac{\upsilon + \eta}{\sqrt{2}} \end{pmatrix} \quad (2.9)
\end{aligned}
$$

so the term $(D_\mu \phi)^\dagger (D^\mu \phi)$ of the Lagrangian becomes

$$(D_\mu \phi)^\dagger (D^\mu \phi) = \frac{1}{2} \partial_\mu \eta \partial^\mu \eta + \frac{1}{8} \left\| \left(g' Y a^\mu + g \vec{T} \cdot \vec{B}^\mu \right) \begin{pmatrix} 0 \\ \upsilon + \eta \end{pmatrix} \right\|^2 . \quad (2.10)$$

The second term of this equation is

$$\left\| \left(g' Y a^\mu + g \vec{T} \cdot \vec{B}^\mu \right) \begin{pmatrix} 0 \\ \upsilon + \eta \end{pmatrix} \right\|^2 = \left\| \begin{pmatrix} g' a_\mu + g B_\mu^3 & g B_\mu^1 - i g B_\mu^2 \\ g B_\mu^1 + i g B_\mu^2 & g' a_\mu - g B_\mu^3 \end{pmatrix} \begin{pmatrix} 0 \\ \upsilon + \eta \end{pmatrix} \right\|^2 =$$

$$= \left\| \begin{pmatrix} (g B_\mu^1 - i g B_\mu^2)(\upsilon + \eta) \\ (g' a_\mu - g B_\mu^3)(\upsilon + \eta) \end{pmatrix} \right\|^2 . \quad (2.11)$$

Ignoring terms higher than the second order, we obtain

$$\left\| \left(g' Y a^\mu + g \vec{T} \cdot \vec{B}^\mu \right) \begin{pmatrix} 0 \\ \upsilon + \eta \end{pmatrix} \right\|^2 \simeq g^2 (g B_\mu^1 - i g B_\mu^2)(g B^{1\mu} + i g B^{2\mu}) \upsilon^2 +$$

$$+ \upsilon^2 (g' a_\mu - g B_\mu^3)(g' a^\mu - g B^{3\mu}). \quad (2.12)$$

This can be semplify writing the fields as

$$W_\mu^+ = \frac{1}{\sqrt{2}} \left(B_\mu^1 - i B_\mu^2 \right)$$

$$W_\mu^- = \frac{1}{\sqrt{2}} \left(B_\mu^1 + i B_\mu^2 \right)$$

$$c Z_\mu^0 = -g' a_\mu + g B_\mu^3$$

$$c A_\mu = g' a_\mu + g B_\mu^3$$

with $c = \sqrt{g'^2 + g^2}$.
Then it is obtained:

$$(D_\mu \phi)^\dagger (D^\mu \phi) = \frac{1}{2} \partial_\mu \eta \partial^\mu \eta + \frac{g^2 \upsilon^2}{8} \left(|W_\mu^+|^2 + |W_\mu^-|^2 \right) + \frac{\upsilon^2 c^2}{8} |c Z_\mu^0|^2 . \quad (2.13)$$

From the parametrization of ϕ we can explicate the terms $\phi^\dagger \phi$ and $(\phi^\dagger \phi)^2$:

$$\phi^\dagger \phi = \frac{\upsilon^2 + \eta^2 + 2 \upsilon \eta}{2} \quad (2.14)$$

$$\left(\phi^\dagger \phi \right)^2 \simeq \frac{1}{4} \left(\upsilon^4 + 4 \upsilon^2 \eta^2 + 2 \upsilon^2 \eta^2 + 2 \upsilon^3 \eta \right) \quad (2.15)$$

The potential of the Lagrangian $\mathcal{L}_S$ is then

$$\mu^2\left(\phi^\dagger\phi\right) + \lambda\left(\phi^\dagger\phi\right)^2 \simeq \eta^2\left(\frac{\mu^2}{2} + \frac{3}{2}\lambda\upsilon^2\right) + \upsilon\eta\left(\mu^2 + \lambda\upsilon^2\right) = -\eta^2\mu^2 \quad (2.16)$$

If one writes $m_\mu = \sqrt{-2\mu^2}$ it is obtained

$$\mu^2\left(\phi^\dagger\phi\right) + \lambda\left(\phi^\dagger\phi\right)^2 \simeq \frac{m_\mu}{2}\mu^2 \quad (2.17)$$

and the Lagrangian becomes

$$\mathcal{L}_S = \left(\frac{1}{2}\partial_\mu\eta\,\partial^\mu\eta - \frac{m_\mu}{2}\mu^2\right) + \frac{g^2\upsilon^2}{8}\left(\left|W_\mu^+\right|^2 + \left|W_\mu^-\right|^2\right) + \frac{\upsilon^2c^2}{8}\left|cZ_\mu^0\right|^2 \quad (2.18)$$

In this last formula, it appears that η is a scalar particle with charge zero, called *Higgs boson*, with a mass m_μ not determined by the theory; W_μ^+, W_μ^- and Z_μ^0 are the three gauge boson of weak interaction, with masses

$$m_W = \frac{g\upsilon}{2} \text{ and } m_Z = \frac{\upsilon c}{2}$$

for $W_\mu^\pm$ and for Z_μ^0 respectively.

The ratio between the boson masses is less than one:

$$\frac{m_W}{m_Z} = \frac{g\upsilon}{2}\frac{2}{\upsilon c} = \frac{g}{c} = \frac{g}{\sqrt{g'^2+g^2}} < 1 \quad (2.19)$$

It is then possible to introduce the *Weinberg angle* θ$_W$ defined as

$$\tan\theta_W = \frac{g'}{g} \quad (2.20)$$

and then:

$$\cos\theta_W = \frac{g}{\sqrt{g'^2+g^2}} = \frac{m_W}{m_Z} \qquad sen\,\theta_W = \frac{g'}{\sqrt{g'^2+g^2}}$$

It is possible to write A_μ and Z_μ^0 as a function of θ$_W$:

$$A_\mu = \sin\theta_W B_\mu^3 + \cos\theta_W a_\mu$$

$$Z_\mu^0 = -\sin\theta_W a_\mu + \cos\theta_W B_\mu^3$$

(2.21)

The A_μ remains massless, and it is the electromagnetic propagator, the *photon*.

Substituting the fields a_μ and $\vec{B}_\mu$ in the $\mathcal{L}_F$ lagrangian, it is possible to obtain the couplings between the fermionic fields and the gauge bosons (in particular the Lagrangian of QED is found, assuming $e = g'\cos\theta_W$).

The mass of the fermionic fields in the Lagrangian $\mathcal{L}_{YK}$ can be obtained if the expression of the fields used is explicated:

$$\mathcal{L}_{YK} = -G_e \left[\overline{e_R^-} \begin{pmatrix} \phi^- & \phi^0 \end{pmatrix} \begin{pmatrix} \nu_e \\ e^- \end{pmatrix}_L + \begin{pmatrix} \overline{\nu_e} & \overline{e^-} \end{pmatrix}_L \begin{pmatrix} \phi^+ \\ \phi^0 \end{pmatrix} e_R^- \right] \quad (2.22)$$

Then φ is parametrized as previously:

$$\begin{aligned}
\mathcal{L}_{YK} &= -\frac{G_e}{\sqrt{2}} \left[\overline{e_R^-} \begin{pmatrix} 0 & \upsilon+\eta \end{pmatrix} \begin{pmatrix} \nu_e \\ e_L^- \end{pmatrix} + \begin{pmatrix} \overline{\nu_e} & \overline{e^-} \end{pmatrix}_L \begin{pmatrix} 0 \\ \upsilon+\eta \end{pmatrix} e_R^- \right] = \\
&= -\frac{G_e}{\sqrt{2}} \left[\overline{e_R^-}\upsilon e_L^- + \overline{e_R^-}\eta e_L^- + \overline{e_L^-}\upsilon e_R^- + \overline{e_L^-}\eta e_R^- \right] = \\
&= -\frac{G_e\upsilon}{\sqrt{2}} \left(\overline{e_R^-}e_L^- + \overline{e_L^-}e_R^- \right) - \frac{G_e\eta}{\sqrt{2}} \left(\overline{e_R^-}e_L^- + \overline{e_L^-}e_R^- \right)
\end{aligned}$$

(2.23)

If it is put $e = \begin{pmatrix} e_L^- \\ e_R^- \end{pmatrix}$, it is obtained:

$$\mathcal{L}_{YK} = -\frac{G_e\upsilon}{\sqrt{2}}\overline{e}e - \frac{G_e\eta}{\sqrt{2}}\overline{e}e \quad (2.24)$$

The electron mass can be defined as $m_e = \dfrac{G_e\upsilon}{\sqrt{2}}$ so the Yukawa Lagrangian is

$$\mathcal{L}_{YK} = -m_e\overline{e}e - \frac{m_e\eta}{\upsilon}\overline{e}e \quad (2.25)$$

The second term indicates the coupling between the electron and the Higgs

field. As for the massive gauge bosons, the coupling is proportional to the masses.

2.2 W±, Z⁰ and Higgs in LHC

2.2.1 *W±* production and decay.

The mass and the width of the *W* boson were measured by LEP and Tevatron experiments with the highest precision. The world average values are 80.420 ± 0.031 GeV and 2.085 ± 0.042 GeV respectively[28]. The branching ratio of its decay channels are given in the table 2.1.

The production of *W* bosons at the LHC is due to the **Drell-Yan process**. The dominant processes with a leptonic final state at the LHC are $q\bar{q} \to W^{\pm} \to l^{\pm} \nu (\bar{\nu})$ (Figure 2.2).

Decay mode	Probability (%)
$W \to e\,\nu$	10.80 ± 0.09
$W \to \mu\,\nu$	10.75 ± 0.13
$W \to \tau\,\nu$	11.25 ± 0.20
Hadrons	67.60 ± 0.27

Table 2.1: Branching ratio for the various W boson decay channels[28]
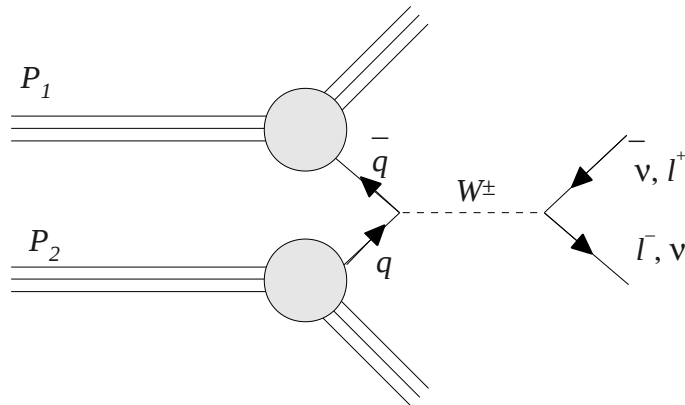
Fig. 2.2: Leading order diagram of the Drell-Yan process in *W* production

2.2.2 Z^0 production and decay

The mass and the width of the Z boson were measured by the LEP experiments to highest precision. The world average values are 91.1876 ± 0.0021 GeV and 2.4952 ± 0.0023 GeV respectively[28]. The branching ratios of its decay channels are given in the table 2.2.

The production of Z bosons at the LHC is due to the **Drell-Yan process** in which a quark and an antiquark annihilate to form a vector boson (Figure 2.3). The dominating processes with a letponic final state at the LHC are $q\bar{q} \rightarrow Z^0/\gamma^* \rightarrow l^+ l^-$ (65%) and $qg \rightarrow q\gamma^*/Z^0 \rightarrow ql^+ l^-$ (35%). The dominant higher order correction of the first process is the scattering of a quark with a gluon, which contributes roughly 1/3 to the overall cross-section of this process.

Decay mode	Probability (%)
$Z \rightarrow e^+ e^-$	3.363 ± 0.004
$Z \rightarrow \mu^+ \mu^-$	3.366 ± 0.007
$Z \rightarrow \tau^+ \tau^-$	3.367 ± 0.008
Invisibles	20.00 ± 0.06
Hadrons	69.91 ± 0.06

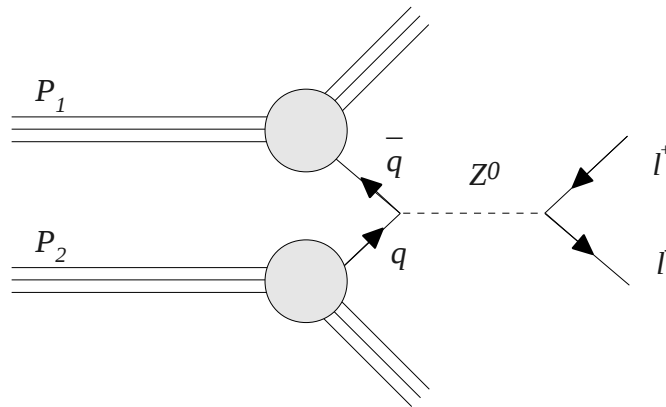**Table 2.2:** Branching ratio for the various Z boson decay channels[28]

Fig. 2.3: Leading order diagram of the Drell-Yan process in Z^0 production

2.2.3 SM Higgs production

The production of the standard model Higgs boson at LHC is expected to proceed mainly through four process (Figure 2.4): gluon-gluon fusion mechanism, vector-boson fusion mechanism, Higgs-strahlung mechanism and associated production.

The **gluon-gluon fusion mechanism** $gg{\rightarrow}H$ is the dominant mechanism in the Higgs mass range up to about 1 TeV; the gluons coupling to the Higgs boson are mediated by a triangular loop of top and bottom quarks

The **vector-boson fusion mechanism** $qq{\rightarrow}qqV^*V^*{\rightarrow}Hqq$ is the 10% of the total production cross section for $m_H < 2m_Z$ and it becomes comparable to the gluon fusion Higgs masses around 1 TeV. This process lead very distinctive signatures of two jets emitted at small angle respect to the beam axis, with central activity suppressed due to the lack of color exchange between the two quarks.

The **Higgs-strahlung mechanism** $q\bar{q} {\rightarrow}V^*{\rightarrow}VH$ and the **associated production** of the Higgs boson with top pair $gg{\rightarrow}Ht\bar{t}$ and $q\bar{q}{\rightarrow}Ht\bar{t}$ have lower cross sections than the previous mechanisms, but they have a better signal to background ratio. The first is useful in the intermediate Higgs mass range due to the possibility to tag the associated vector boson; the second provides an additional option by tagging the top pair.
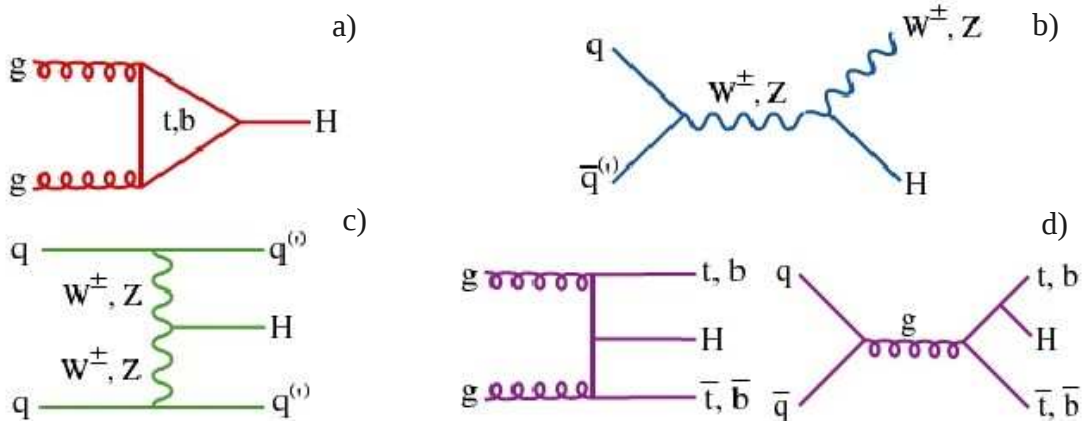

Fig. 2.4: Main processes of production for the standard model Higgs boson at LHC: a) gluon gluon fusion mechanism; b) Higgs-strahlung; c) vector boson fusion; d) Higgs associated production.

2.2.3 Limits on Higgs mass

Even if the Higgs mass m_H is a free parameter in the SM, it is possible to obtain some constraints that are derived from theory and from direct and indirect searches. One constraint on Higgs mass is obtained performing a fit with the electroweak parameters measured with high precision at LEP, Tevatron and SLAC. The fit is used to probe indirectly the Higgs sector which is still unexplored. A first set of measurements performed at LEP and SLD is related to the Z^0 line shape, lepton asymmetries, τ-polarization, $q\bar{q}$ charge asymmetry and heavy flavours[29]. The W and top mass measurement preformed at the Tevatron Collider are also taken into account. Other measurements not exclusively related with accelerator physics, like the $sin\theta_{eff}$ measurement from neutrino interaction and the G_F constant extracted from precise measurements on the muon lifetime are included. In the fit the Higgs mass is left as a free parameter.

The best accuracy on the prevision is obtained including all the data in the fit (Figure 2.5). The results of the fit is $m_H = 84^{+34}_{-26}$ GeV at 68% confidence level. In the plot the yellow bands represent the excluded regions for m_H. The lower
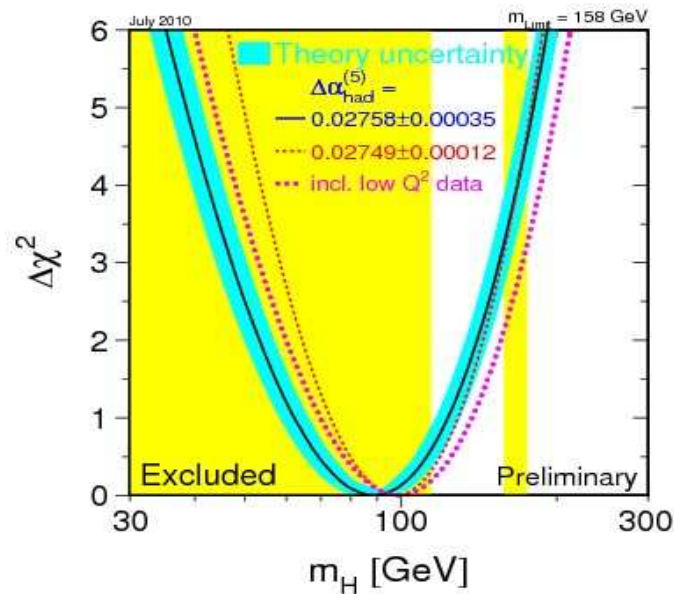

Fig. 2.5: $\Delta\chi = \chi^2 - \chi^2_{min}$ as a function of the Higgs mass. The black line correspond to the results of the fit, while the the blue band represents an estimation of the theoretical error due to missing order corrections. The red and dashed line is the result obtained using the evaluation of $\Delta\alpha^{(5)}(m_Z^2)$ from [30]. The vertical yellow bands show the 95% C.L. excluded region on m_H due to direct search.

limit is derived from the LEP-2 experiments and is $m_H > 114.4$ GeV2[31]; in addition, Tevatron has excluded at 95% CL the value of 160 GeV$<m_H<$170 GeV.

2.2.4 SM Higgs decay

The **Higgs boson coupling to fermions** is proportional to the fermion masses; this is reflected in the decay branching ratio. In the Figure 2.6 the branching ratio for the various Higgs decay channels are shown as function of the Higgs mass[32]. The main channels used at LHC to look for a Standard Model Higgs boson can be classified depending on the Higgs mass: *low mass region* for $m_H<$130 GeV, *intermediate mass region* for 130 GeV$<m_H<2m_Z$, and *high mass region*, for $m_H>2m_Z$.

In the low mass region $H \rightarrow b\bar{b}$ decay channel dominates, but the signal background ratio for the inclusive production is smaller than 10^{-5}, so it will be impossible to observe this channel above the QCD background. The $H \rightarrow \tau\bar{\tau}$ has also a seizable decay rate and amounts to 8% of the total. The channel $H \rightarrow \gamma\gamma$ is considered the major discovery channel because it has a branching ratio of small cross section but a very clean signature.

In the intermediate mass region, the decay is almost entirely through the $H \rightarrow WW^*/WW$ and $H \rightarrow ZZ^*$ channels. The most promising channels for the experimental searches are $H \rightarrow ZZ^* \rightarrow 4l$ and $H \rightarrow WW^* \rightarrow l\nu l\nu$. Around the *WW* threshold, where the pair of dominant *WW* channel become on shell, the *ZZ** branching ratio drops to a level of 2% and reaches again a branching ratio of 30% above the *ZZ* threshold.
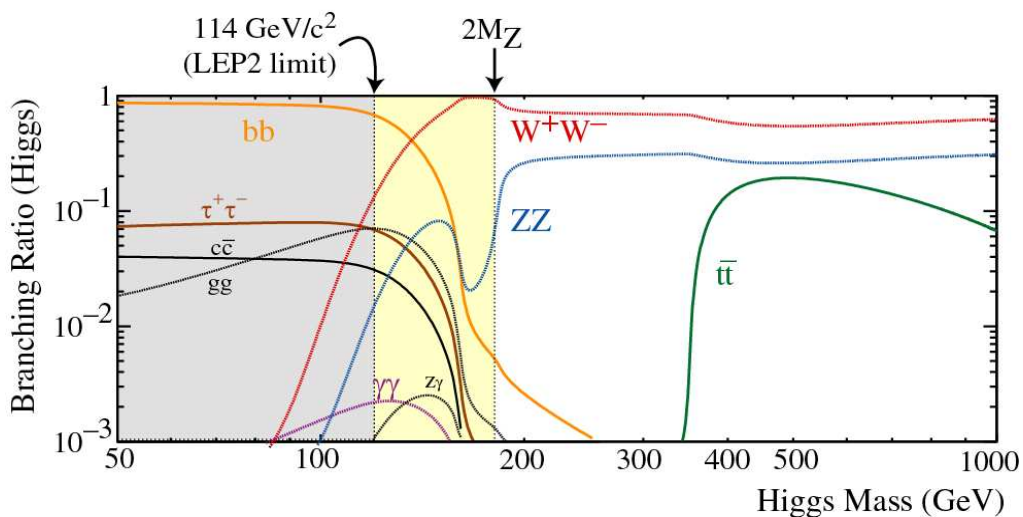

Fig. 2.6: Branching Ratios for the different decay channels of the standard model Higgs Boson for values of Higgs Mass between 50 and 1000 GeV

The high mass region is the best region to discover a Higgs boson signal for LHC, since the $H{\rightarrow}ZZ{\rightarrow}4l$ becomes almost background free. Above the $\bar{t}t$ production threshold the $\bar{t}t$ decay mode opens up but never exceeds a branching ratio of 20%.

Chapter 3

The ATLAS software and computing

During the years in the preparation of ATLAS, several software and computing techniques were developed to allow and aid the generation of simulated ATLAS data and the analysis, the manipulation and the transfer of data both real and simulated.

In this work the ATLAS software tools have been used to obtain from simulated data the expected sensitivity for various measurements and to tune the algorithms to achieve an optimal preparation for the analysis of data.

In this chapter I will show a short summary of the applied software and computing techniques (section 3.1) and of the GRID computing (section 3.2).

3.1 The ATLAS Simulation Software Framework

The basic goal of the ATLAS software is the implementation of a code able to perform event generation, simulation, reconstruction, event filter visualization and to allow the writing of analysis programs to the user, but detaching the user from the typical implementation details.

- In the event generation particles emerging from the collision are generated using codes, called generators, based on physics theories and phenomenology.
- In the simulation, the particles are transported through the detector according the laws that govern the passage of particles through the matter.
- The interactions of particles with sensitive elements of the detector are converted into informations similar to the digital output from the real detector.

● The events are finally reconstructed. The original information (*truth*) of the Monte Carlo is conserved as a comparison with the reconstructed one.

The simulation software runs under a software framework called ATHENA.

3.1.1 ATHENA

The common official software framework of ATLAS is called ATHENA (**AT**las realization of a **H**igh **E**nergy and **N**uclear physics data analysis **A**rchitecture), and it is an Object Oriented/C++ program based on the GAUDI architecture originally developed for LHCb. The ATLAS software is based on the concept of **Packages**, sets of C++ classes and their interfaces and implementations files grouped together.

The main components of ATHENA are Algorithms, Services, Data Objects and Transient Stores, Converters, Tools and Packages.

The **Algorithms** are the basic building blocks of user applications; they accept input data, manipulate it and generate new output data.

The **Services** provide specific capabilities of the framework, and are initialized at the beginning of the job by the framework and used if they are needed by the algorithms.

The **Data Objects** are moved between the algorithms, acting as their input and output. Several TDS (Transient Data Store) are available to reduce the coupling between the Algorithms, and they act as temporary repository for informations. All algorithms have access to TDS via the so-called StoreGate service.

Converters convert an object form a representation to another. **Tools** are an helper class provided from the framework, to which the Algorithm may delegate a specific processes.

3.1.2 Monte Carlo Generators

The purpose of Monte Carlo event generators is to describe the theoretical prediction of physics processes, e.g. the production of a *Z* boson in a proton-proton collision and its decay into two muons. Such a theoretical prediction is crucial to understand the measured data and to tune physics analysis.

In case of LHC Monte Carlo generators must describe the structure of hadrons, the parton showers, the actual hard scattering process, and the hadronization. Various Monte Carlo event generator programs use different approximations during the different steps and therefore the theoretical prediction relies at least partially on the choice of the underlying Event Generator. The generators interfaced with ATHENA are Pythia, Herwig, Isajet, Hjing, Tauola, Photos, Alpgen, Phojetm, CompHep, AcerMC. The data used for

the analysis were produced with Pythia.

Pythia[33] is a general purpose event generator, which is commonly used in high energy physics, because of its easy handling and relatively large predictive power. It can simulate lepton-lepton, lepton-hadron and hadron-hadron interactions with a broad field of theoretical models, including supersymmetric models or models with leptoquarks. These are the main aspect reproduced by Pythia:

- Initially two beam particles are coming each toward other. Each hadron is usually characterized by a set of parton distributions, which defines the partonic substructure in terms of flavour composition and energy sharing.
- One shower initiator parton form each beam stars a sequence of branchings, which build up an initial state shower.
- One incoming parton form each of the two showers enter the hard process. The nature of the process determines the characteristics of the event.
  In Pythia the following major groups of processes are implemented: hard QCD processes (such as $qg{\rightarrow}qg$); soft QCD processes, (as diffractive and elastic scattering); heavy flavour production; photon-induced processes (e.g. $\gamma g{\rightarrow} q\bar{q}$); deep Inelastic Scattering; W/Z production; Standard Model Higgs production; gauge boson scattering processes; Non-Standard Higgs particle production, Technicolor production; Leptoquark; a rich set of Supersymmetry processes. The hard scattering process is calculated in leading order approximation. The higher order corrections are approximated with the parton shower approach. The hadronization process is based on the String-Model.
- The hard process may produce a set of short lifetime resonances, like Z and W.
- The outgoing partons may branch, just like the incoming did, and build up final-state showers.

3.1.3 Simulation

Depending on the speed and the precision with which the user wants to simulate data through ATLAS, there are different levels of simulation of the detector. In fact, large computing resources are required to accurately model the complex detector geometry and physics descriptions in the standard ATLAS simulation, called "full simulation". This has lead to the development of several varieties of "fast simulations". The different simulation package developed in ATLAS are briefly described in the following.

Full simulation

The standard ATLAS detector simulation is based on the GEANT4 toolkit[34], that provides both a framework and the necessary functionalities for running detector simulation in particle physics and other fields. GEANT4 simulates the impact of the magnetic field and the interactions with the material, e.g. multiple scattering, energy loss, photon conversions and further decays of unstable particles. Each interaction of a particle with an active, i.e. sensitive, detector element is stored in a so called hit-object, which represents the position and type of the interaction.

During the digitization step, the response of the detector and of its electronics on the various hit-objects is simulated.

GEANT4 is part of the LCG application software project and it is developed with a world-wide effort, coordinated by a strong development team by CERN. The use of GEANT4 functionalities within ATLAS specific setup is embedded in the ATLAS program, integrated in the ATHENA framework, where tailored packages for handling geometry, kinematics, materials, physics, fields, sensitive detectors, etc., have been added by means of plug-in modules.

The ATLAS detector geometry used in the simulation is as much as possible matched to the as built detector conditions.

Fast simulation

Because of the complicated detector geometry and detailed physics description used by the ATLAS GEANT4 simulation, it is impossible to achieve the required simulated statistics for many physics studies without faster simulation. To that end, several varieties of fast simulation programs have been developed to complement the GEANT4 simulation. In particular these three programs are used: Fast G4 Simulation, ATLFAST-I and ATLFAST-II. All of them have the goal to speed up the calorimeter simulation, that is the slowest part of the full simulation; in fact almost 80% of the full simulation time is spent simulating particles traversing the calorimetry, in particular electromagnetic showers.

Some of the data analyzed in this work were simulated with ATLFAST-II. This tool makes use of the simplified detector description used for reconstruction; it uses full simulation for the inner detector and muon system and *Fast Calorimeter Simulation (FastCaloSim)* in the calorimetry.

3.1.4 Reconstruction and output

Several packages are employed for reconstruction in the ATHENA software framework. In particular for the muons there are three strategies: reconstruction in standalone, combined and tagged.

In the standalone reconstruction, muons are reconstructed by finding tracks in the muon spectrometer and then extrapolating these to the beam line. There are two main standalone algorithms, MOORE[35] (Muon Object Oriented Reconstruction) and Muonboy[36].

Combined muons are found by matching standalone muons to nearby inner detector tracks and then combining the measurements from the two systems in a single track. There are two combined tracking algorithms: STACO [36], and MuID[37]. STACO associates Muonboy and ID tracks statistically using their covariant matrix. MuID combines the MOORE and ID tracks by global fitting using the original measurements in MS and ID.

The third strategy is the one implemented by tagging algorithms, that extrapolate inner detector tracks to the spectrometer detectors and search nearby hits.

For the electrons two different algorithms are actually implemented: the standard one starts form clusters in the EM calorimeter and then builds the identification variables form the signals in the ID and EM calorimeters. The second one, which is suited to the study of low pT electrons, starts from tracks in the ID and then search for a reasonably isolated cluster in the EM calorimeter; the identification variables are than found in the same way of the standard algorithm.

The output of the reconstruction part are so-called Event Summary Data (ESD) and Analysis Object Data (AOD) files. While the first includes a more detailed description of an event, the latter one only includes informations which are of primary interest for physics analysis. Another way to store the
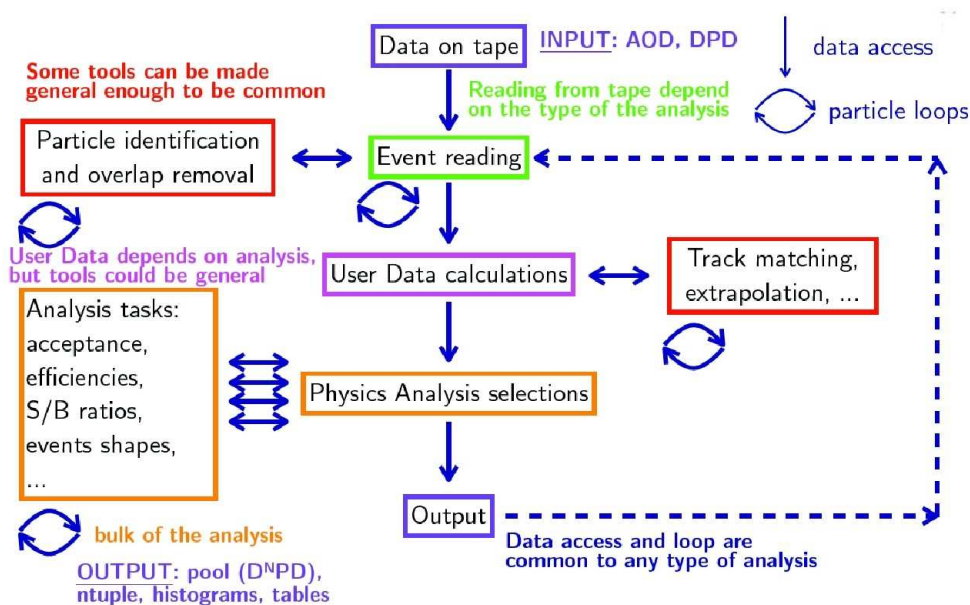

Fig 3.1: Schema of the EWPA analysis framework

events is the CBNT (ComBinedNTuple) production. These are created at the AOD level and are root n-tuples.

The AOD files can have an additional selection in Derived Physics Data (DPD). In the DPD files the AOD content that is not necessary for the specific analysis is removed, and eventually others informations useful for the analysis are added. Secondary and tertiary DPD (D2PD, D3PD) can be produced locally for user analysis (D2PD are more refined DPD, D3PD are flat ntuples suitable for plotting results).

In the creation and analysis of the DPD used in the *Z*, it was employed an analysis framework called EWPA (Every Where Physics Analysis)[38], that is integrated in the ATHENA official ATLAS package, and has been developed by the Pavia ATLAS analysis group. EWPA is a simple and light framework upon which is possible to create multiple plugin tools for users specific physics analysis. The user can run his analysis reading ESD or AOD datasets and creating D2PD in ATHENA, or creating D3PD and then working without ATHENA installed. The schema of the EWPA framework is illustrated in Figure 3.1.

3.2 Grid computing

One year of data taking at the LHC will result in 15 Petabytes (15 million Gigabytes) of data, produced by the four experiments, which have to be carefully analyzed by physicists worldwide to discover new physics processes. Moreover, billions of complex theoretical simulations of the proton-proton collision must be calculated.

In the former LEP experiments, the computer processing was done at a computer farm, near to the experiment itself. For LHC, storage and processing requirements exceed by far the capacities available at a single site and hence a new approach was chosen, which is commonly known under LHC Computing Grid (LCG) project. This computing grid provides to infrastructure for the storage of data and the necessary computing power for the physics analysis and simulations.

The data distribution follows a so-called Tier- structure[39]. The LHC data is recorded in a first step on tape at so called Tier-0 center at CERN. From there, it is further distributed to worldwide Tier-1 centers, which store also a large part of data and provide a twenty-four hour support. The Tier-2 centers store only a small part of data since they are designated for user specific physics analysis and simulation. The Grid is accessed via the lowest hierarchy level (Tier-3), which are small computer clusters or individual PCS of physicists. A schema of the Tier structure is depicted in Figure 3.2. Tier-structure has several advantages. First of all, several copies of data exist, which ensures that data safety. The single Tier centers are independent from each

other which minimizes the critical points in the infrastructure. A further advantage is the cost sharing for maintenance and support through the several national computer centers.

The LCG project involves dedicated hardware and software developments. Obviously, an adequate bandwidth is needed for the data distribution within the grid. The grid-software must be compatible with heterogeneous hardware and must also ensure coherent software at all connected computers. Distributed data must be identifiable by the user and stored redundantly. Moreover a fair access to all resources for all users (load balancing) must be guaranteed and a secure access to all the sites without local accounts must be provided.
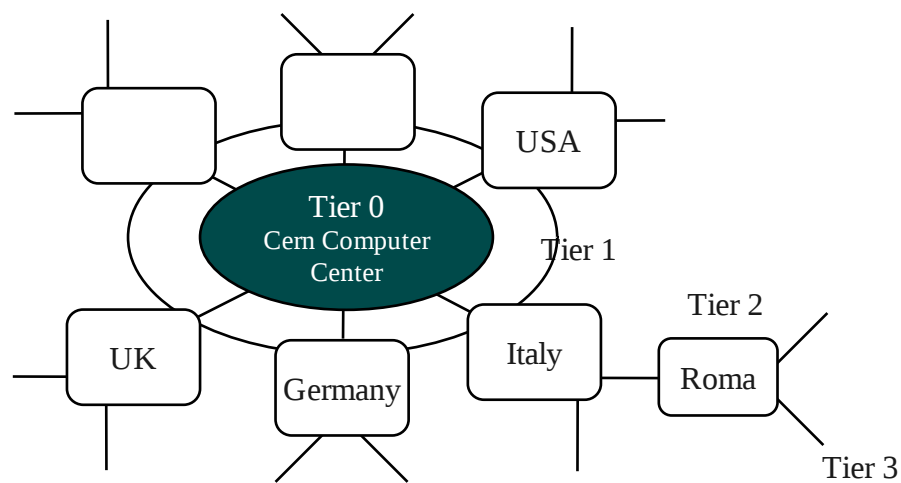
Fig 3.2: Tier structure of the LGC Grid.

Chapter 4

The search for the Higgs boson in the channel
H→ZZ→4l*

The search for the Standard Model Higgs boson is the major goal of the Large Hadron Collider (LHC). The Higgs boson mass is a free parameter in the SM, however there is strong expectation motivated by precision electroweak data[29] and direct searches[31] that a low mass Higgs should be discovered at the LHC.

The experimentally cleanest signature for the discovery of the Higgs is its decay channel to four leptons (electrons and muons): *H→ZZ→4l*. The excellent energy resolution and linearity of the reconstructed electrons and muons in ATLAS leads to a narrow 4-lepton invariant mass peak on top of a smooth background. For Higgs masses above $2m_Z$, this channel becomes the "golden" channel for SM Higgs searches.

The expected signal to background ratio after all experimental cuts depends on the Higgs mass itself. In the mass range between ~120 GeV and $2m_Z$ the sources of background that affect this channel are large. The continuum *pp→ZZ*→4l* constitutes the *irreducible background*; its final state in fact is characterized by four isolated leptons as well as the signal events. In addition, there is a smaller background from *ZZ** continuum production, where one of the *Z* boson decay into τ-pair, with subsequent decays of the τ-leptons, and the other *Z* decays into a muon or electron pair; also this background can have 4 isolated leptons in the final state. Background sources like $Z b \bar{b} \rightarrow 2 l b \bar{b}$ or $t \bar{t} \rightarrow W b W \bar{b} \rightarrow l \nu b l \nu \bar{b}$ with two leptons produced in heavy flavor decays represent the *reducible background* dominant at production level; in this background the presence of non isolated muons is expected. These background require tight lepton isolation cuts to keep their contribution well below the *ZZ* continuum.

For $m_H > 2m_Z$ the "golden" channel with two real Z bosons in final state opens up. In this mass range, the signal dominates the background, mainly constituted by the continuum ZZ.

In this chapter I report the analysis performed for the channel $H{\to}ZZ^*{\to}4l$ for the masses between 120 and 180 GeV. I have participated and contributed to this analysis as a member of the Higgs working group at CERN[40],[41].

This chapter is organized as follow. In Section 4.1 the results of a preliminary technical analysis done by all the groups of the collaboration are shown. In Section 4.2 two methods for background extraction in the Higgs mass region are described.

4.1 Technical analysis

In the first phase of my work I have participated to the initial analysis for the CSC note and internal note. This preliminary work was done by all the different groups of the collaboration: the same data were analyzed with methods developed independently from each group. The goal was to tune the individual code of the different groups obtaining the same results with different approaches (using AOD with ATHENA, AOD with EventView, CBNT...). After this step, the group has evaluated which was the optimal lepton quality that could be used in the analysis, choosing which of the muon reconstruction packages would be employed and which electron identification quality would be better suited for our purposes, and the better set of cuts.

In this analysis the different groups used the same cuts. The sequence and the kind of cuts used are based on the TDR analysis[13]. These are relative to:

- the acceptance of the detector and of the trigger;
- the kinematics of the event;
- the reconstructed mass of ZZ pair;
- the isolation of the leptons and the vertex identification;

The details of the cuts and analysis checks used are shown in Table 4.1. In this phase our group examined the data for $H{\to}4l$ stored as AOD using ATHENA (release 12); the AOD were stored on the cluster CASTOR at CERN.

4.1.1 Dataset

The ATLAS detector was simulated by the GEANT4 software[34]. Simulation, digitization and reconstruction have been all performed within the ATLAS software framework ATHENA offline, release 12. The set of $H{\to}4l$ samples used in this analysis is for m_H of 130 GeV, with 39,250 events.

4.1.2 Muon Identification

The muon identification in ATLAS relies on the Muon Spectrometer (MS) for standalone reconstruction as well as on the Inner Detector (ID) and Calorimeters for combined muon reconstruction. In order to combine the muon tracks reconstructed in the ID and the MS, the ATLAS offline muon identification packages (as MUID and STACO) have been developed.

Lepton definitions	STACO/MUID combined muons, *Medium* Electrons.
1.1	Four leptons with $|\eta| < 2.5$.
1.2	Leptons with $p_T > 7$ GeV/c, at least two with $p_T > 20$ GeV/c.
2.0	2 pairs of same flavour opposite charge leptons.
2.1-2.2	$|M_{ll1} - M_Z| < 15$GeV, with M_{ll1} the closest to M_Z
2.3-2.4	$M_{ll2} > 20$ GeV, with M_{ll2} from the highest possible p_T leptons.
3.1-3.3	Check on the number of events with a reconstructed mass inside a window ΔM_H centered on the nominal Higgs mass; $\Delta M_H = 2, 5, 10$ GeV
4.1	Calorimetric isolation $\left(\sum E_T < 5 \text{ GeV.}\right)$
4.2	Lepton Inner detector track isolation $\left(\sum p_T < 5 \text{ GeV.}\right)$
5.1-5.2	Cut on transverse impact parameter significance $(d_0/\sigma_{d_0} < 5)$.

Table 4.1: Summary of the cuts and checks requested in the $H \to 4l$ technical analysis. The two lepton pairs are denoted as M_{ll1} and M_{ll2}.

The purpose of these packages is to associate segments and tracks found in the MS with the corresponding ID track in order to identify muons at their production vertex with optimum parameter resolution. In the output data used in the actual ATLAS physics analysis there are two different collections of muons. Each collection refers to a family of reconstruction algorithms: MUID or STACO (see chapter 3). In this analysis a user code running under ATHENA has been written to choose between the STACO or the MUID muons from the official AOD.

4.1.3 Electron identification

In the electron reconstruction three different criteria of identification are used (*Loose*, *Medium* and *Tight* cut). In this analysis the particle is defined as an

Electron Identification		
Cut	Type	Description
Loose	Acceptance of the detector Hadronic leakage	$\|\eta\| < 2.47$ Ratio of E_T in the first sampling of the hadronic calorimeter to E_T of the EM cluster
	Second layer of EM calorimeter	Ratio in η of cell energies in 3x7 versus 7x7 cells. Ratio in ϕ of cell energies in 3x3 versus 3x7 cells. Lateral width of the shower
Medium (include *Loose* cuts)	First layer of EM calorimeter	Difference between energy associated with the second largest energy deposit and the energy associated with the minimal value between the first and second maxims. Second largest energy deposit normalized to the cluster energy. Total shower width. Shower width for three strips around maximum strip. Fraction energy outside core of three central strips but within seven strips.
	Track quality	Number of hits in the pixel detector (at least one) Number of hits in the pixels and SCT (at least nine) Transverse impact parameter (< 1mm)
Tight (include *Loose* and *Medium* cuts)	Isolation	Ratio of transverse energy in a cone ΔR <2 to the total cluster transverse energy.
	Vertexing-layer	Number of hits in the vertexing-layer (at least one)
	Track matching	$\Delta\eta$ between the cluster and the track (< 0.005). $\Delta\phi$ between the cluster and the track (< 0.02). Ratio of the cluster energy to the track momentum.
	TRT	Total number of hits in the TRT. Ratio of the number of the high-threshold hits to the total number of hits in the TRT.

Table 4.2: Standard electron identification strategies.

electron if cuts corresponding to the medium quality are satisfied. They are relative to shower profile, and energy released in the EM calorimeter, leakage in the hadronic calorimeter, and quality of track reconstruction. In Table 4.2 all the electron identification criteria are reported.

4.1.4 Event Selection

I show here some of the plots and results obtained at different steps of the analysis. The final tables summarize them for all the considered channels.

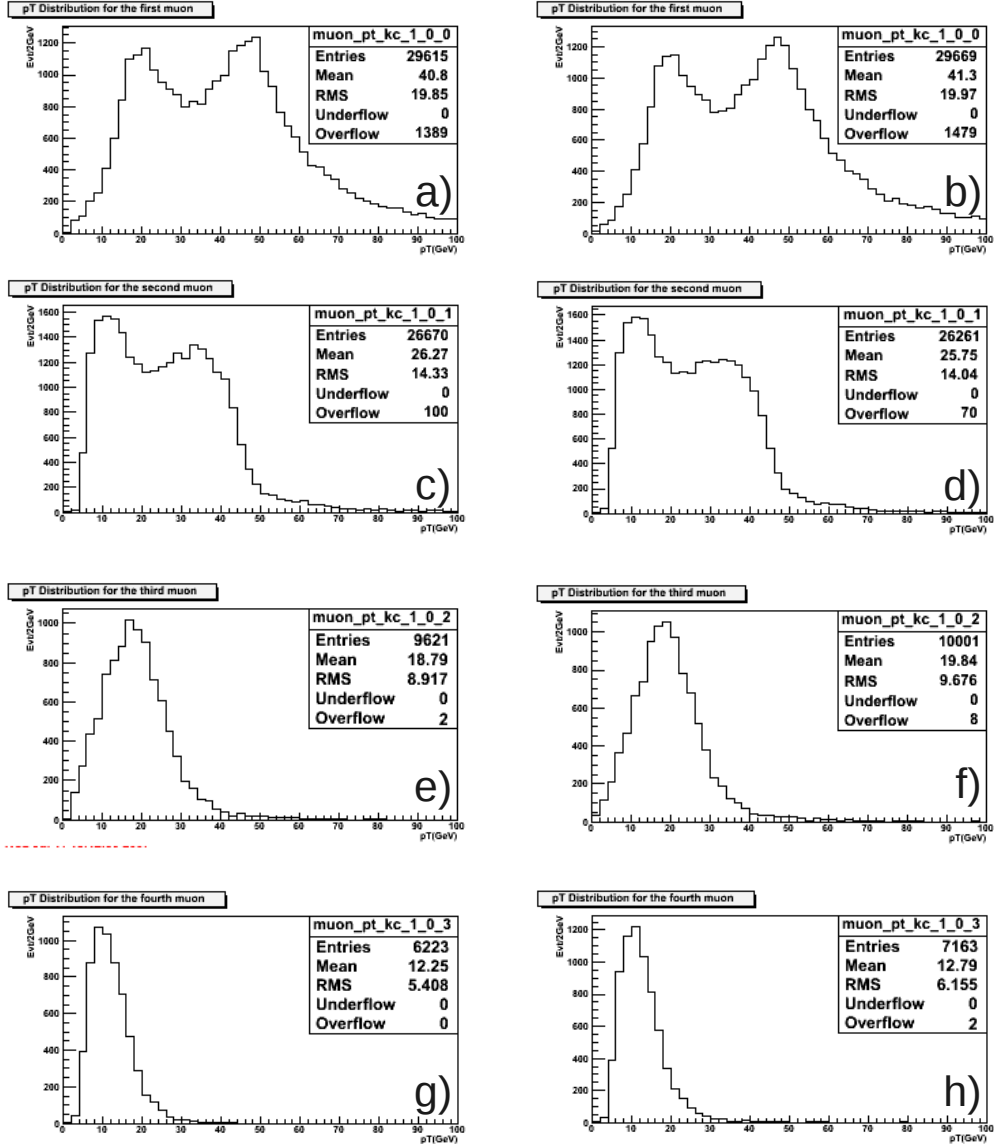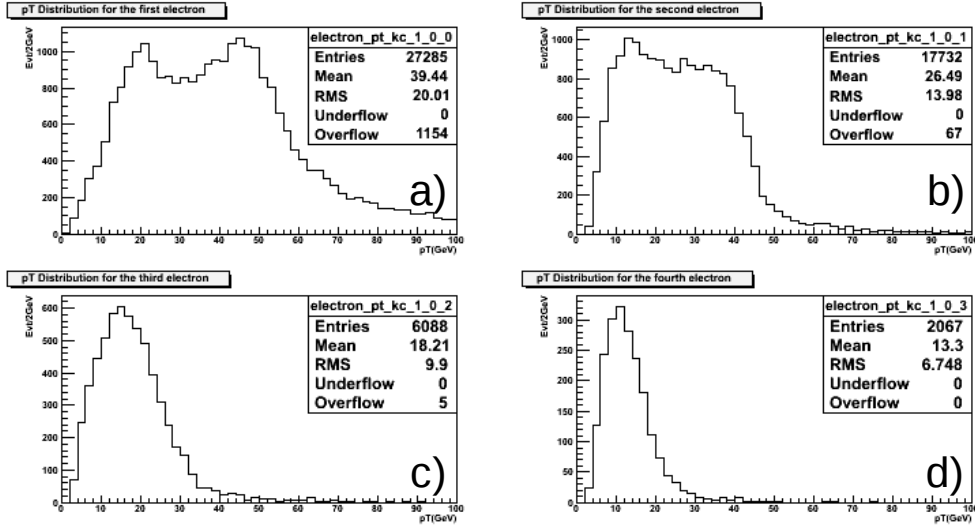In the fig. 4.1 the distributions of the transverse momentum for the first

Fig. 4.1: Transversal momentum (p_T) distributions for the first four muons (in order of p_T) before any cut. a) distribution for the highest p_T muons with MUID reconstruction. b) distribution for the highest p_T muons with STACO reconstruction. c) distribution for the second highest p_T muons with MUID reconstruction. d) distribution for the second highest p_T muons with STACO reconstruction. e) distribution for the third highest p_T muons with MUID reconstruction. f) distribution for the third highest p_T muons with STACO reconstruction. g) distribution for the fourth highest p_T muons with MUID reconstruction. h) distribution for the fourth highest p_T muons with STACO reconstruction.

four highest p_T signal muons are shown without any cut and both for the two track reconstruction packages, MUID and STACO. The initial number of events is 39250 and in the 75% at least a muon is reconstructed, in very good agreement with the theoretical branching ratio. The low energy peak in the first and second muon distribution correspond essentially to the virtual *Z* decay for the channel *H➙ZZ*➙2μ2e*. The STACO reconstruction is a little more powerful than the MUID.

In the fig. 4.2 the distributions of the transverse momentum for the first four highest p_T signal *Medium* electrons are shown without any cut. In agreement with the theoretical branching ratio, we expect that at least one electron is reconstructed in the 75% of events, but only the 70% of event are selected due to the electron quality requirements. Again, the low energy peak in the first and second electron distribution correspond essentially to the virtual *Z* decay for the channel *H➙ZZ*➙2μ2e*.

Fig. 4.2: Transversal momentum (p_T) distributions for the first four (in order of p_T) before any cut. a) distribution for the highest p_T electron. b) distribution for the second highest p_T electron. c) distribution for the third highest p_T electron. d) distribution for the fourth highest p_T electron.

In the fig. 4.3 is reported the η distributions for the highest p_T muons and electrons. The minimum at η = 0 is due to the experimental layout of the detector (there is an opening in the central $R - \phi$ plane (η = 0) for the passage of cables and services).

Event preselection and Kinematic cuts

It is requested that the events have at least 4 leptons with |η|<2.5, p_T>7 GeV/c with at least of two of these leptons having p_T>20 GeV/c. In figure
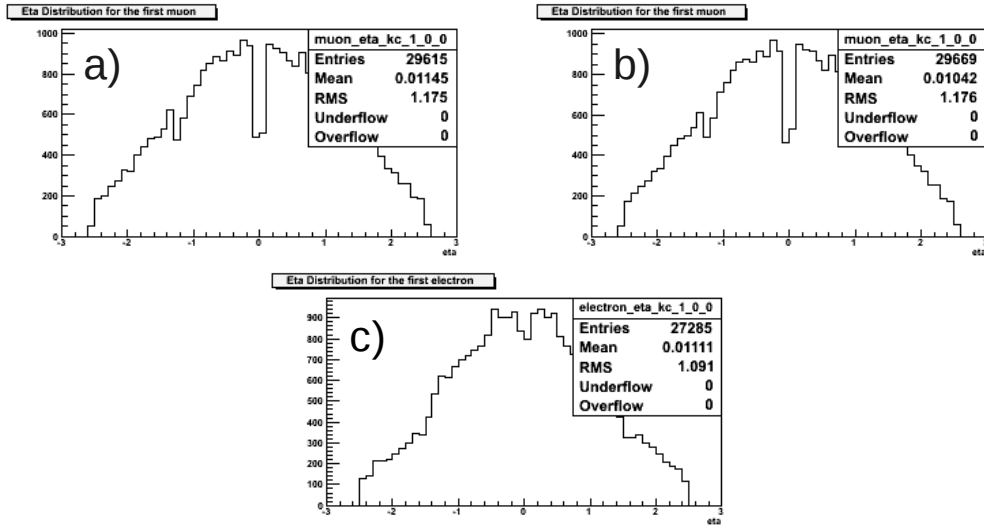
Fig 4.3: The η distributions for the highest p_T muons and electrons, before any cut. a) MUID muons; b) STACO muons; c) electrons.
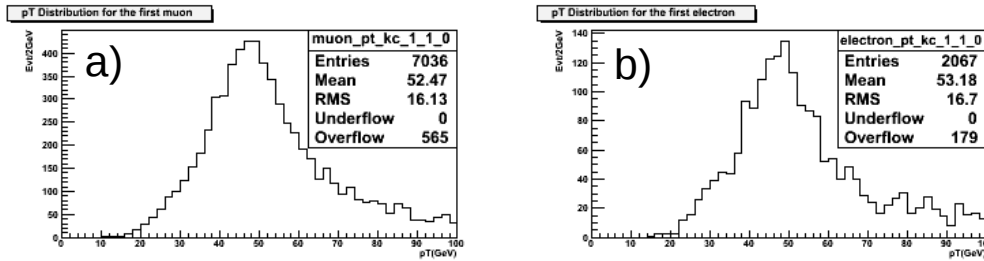

Fig. 4.4: Distributions of the transverse momentum for the highest p_T STACO muons and the highest p_T electrons, after the selection of events with at least 4 leptons with |η| <2.5

4.4 I report the distributions of the highest p_T electrons and STACO muons after the selection of events with 4 electrons with |η|<2.5 and 4 muons with |η|<2.5 respectively.

ZZ selection*

It is required to the events to have at least four leptons which can be combined in at least two pairs of opposite charge and same flavor.

With the mass that we are considering (130 GeV) Higgs decay into a real Z and a virtual Z (Z*); in the figure 4.5 and 4.6 the distributions of the distributions for the pair with second highest p_T (which usually came from the virtual one) are shown.
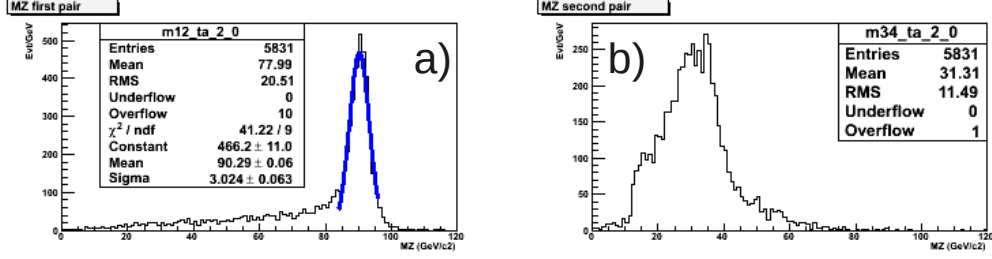
Fig 4.5: a) invariant mass distribution for highest p_T STACO muon pair. b) invariant mass distribution for the second highest p_T STACO muon pair.
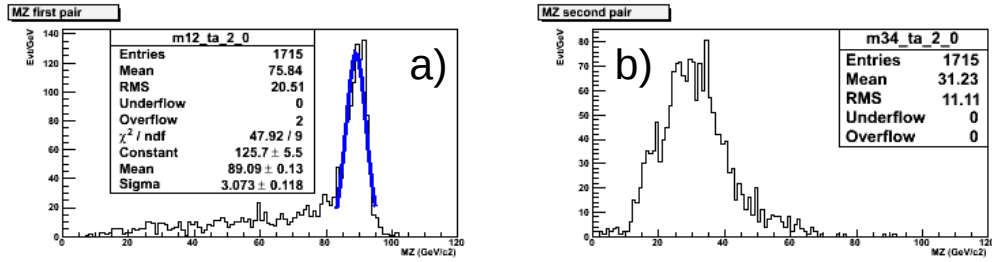

Fig: 4.6: a) invariant mass distribution for highest p_T electron pair. b) invariant mass distribution for the second highest p_T electron pair.

To improve the resolution of the Higgs mass, a constraint on the reconstructed Z is then imposed (the pair of leptons with invariant mass closest to the nominal Z mass has to be inside a mass window of 15 GeV centered on the Z mass; the pair of leptons with highest p_T between the Z^* candidates has to have an invariant mass higher than 20 GeV).

Isolation

To reduce the large $Zb\bar{b}$ and $t\bar{t}$ background (the reducible background sources) we can apply additional criteria. A reduction well below the irreducible ZZ^* background yield is a safeguard against large uncertainties in the yields of these backgrounds. One can exploit the fact that leptons originating from the Z boson decays are expected to be significantly more isolated than the ones originating from heavy quark leptonic decays.

For each lepton, the sum transverse energy deposited in the calorimeter EM inside a cone of radius $\Delta R = 0.2$ ($\Delta R = \sqrt{\Delta \eta^2 + \Delta \varphi^2}$) centered on the track had to be less than 5 GeV. The lepton own transverse energy is excluded.

For each lepton, the sum of transverse momenta of the inner detector tracks in a cone of radius $\Delta R = 2$ centered on the track had to be less than 5 GeV/c. The lepton own transverse momentum is excluded.

Impact parameter

Leptons from $t\bar{t}$ and $Zb\bar{b}$ backgrounds are most likely to originate from displaced vertexes while leptons produced in Z decay are expected to originate from the main interaction point. Further rejection of these backgrounds are achieved by placing a cut on the transverse impact parameter significance (defined as d_0/σ_{d_0} where d_0 is the distance of closest approach in the transverse plane) of the tracks associated to the leptons. The impact parameter is calculated with respect to the event vertex fitted using a set of tracks reconstructed in the ID. This allows to remove the effect of the spread of the vertex position, which at LHC is 15 μm along each of the transverse x and y axes. We select the events with an impact parameter less than 5 for all leptons.

Final results

The aim of this work was to verify the consistency of results of independent analysis based on different data formats. This consistence, expressed as number of events survived the cuts, obtained from the different groups, is shown in Tables 4.3, 4.4 and 4.5. The little discrepancies between the results are probably due to the different data format used. We note that the analysis performed using directly the AOD under ATHENA (Cosenza, Roma, Wisconsin) obtain the same results. After this step for muons reconstruction the STACO package was chosen for the final analysis and some cuts for isolation and track reconstruction have been tuned, and used to reconstruct the Higgs mass and study the background.

Cut	Artemis	Athens	Cosenza	Madrid	Orsay	Roma	SMU	Wisc. (AOD)	Wisc. (AAN)
none	39250	39250	39250	39250	39250	39250	39250	39250	39250
1.1		2067	2067		2067	2067	2067	2067	2067
1.2	1739	1744	1744	2088	1744	1744	1744	1744	1744
2.1-2.4	1173	1174	1174		1174	1174	1174	1174	1174
3.1		511	511	494	511	511	511	511	511
3.2	921	921	921	881	921	921	921	921	921
3.3		1114	1114	1072	1114	1114	1114	1114	1114
4.1	819	817	817	781	817	817		817	817
4.2	801	800	800	789		800		800	800
5.x	649	648	648	607		648		648	648

Table 4.3: *H*➙4*e* cut flow for all the groups. The cuts are detailed in Table 4.1.

Cut	Artemis	Athens	Cosenza	Madrid	Orsay	Roma	SMU	Wisc. (AOD)	Wisc. (AAN)
none	39250	39250	39250	39250	39250	39250	39250	39250	39250
1.1	7036	7036	7036		7036	7036	7036	7036	7036
1.2	5845	5845	5845	7026	5845	5845	5845	5845	5845
2.1-2.4	4155	4156	4155		4156	4155	4156	4156	4156
3.1		2422	2422	2257	2421	2422	2422	2422	2422
3.2	3676	3676	3676	3429	3673	3676	3676	3676	3676
3.3		4019	4109	3739	4015	4019	4019	4019	4019
4.1	3467	3465	3465	3255		3465		3465	3462
4.2	3274	3275	3272	3235		3272		3272	3267
5.x	3046	3047	3044	2890		3044		3044	3040

Table 4.4: *H*➙4μ cut flow for all the groups. The cuts are detailed in Table 4.1.

Cut	Artemis	Athens	Cosenza	Madrid	Roma	SMU	Wisc. (AOD)	Wisc. (AAN)
none	39250	39250	39250	39250	39250	39250	39250	39250
1.1	8133	7781	7782		7781	7781	7782	7782
1.2	6413	6427	6444		6427	6427	6444	6444
2.1-2.4	4353	4358	4357		4357	4358	4358	4358
3.1		2306	2306	2138	2306	2306	2306	2306
3.2	3653	3654	3654	3357	3654	3654	3654	3654
3.3		4158	4157	3834	4157	4158	4158	4158
4.1	3122	3117	3117	2915	3117		3117	3116
4.2	3056	3053	3053	3054	3053		3053	3047
5.x	2622	2620	2620	2301	2620		2620	2614

Table 4.5: *H*➙2*e*2μ cut flow for all the groups. The cuts are detailed in Table 4.1.

4.2 Background Analysis

The second part of my work, after event selection, has been devoted to the study of the main backgrounds of the Higgs into four leptons. In the first paragraphs of this section the datasets employed and the cuts used in the analysis are shown, while the last section illustrates the two methods used to study the background.

4.2.1 Datasets

The ATLAS detector was again simulated by the GEANT4 software[34]. Simulation, digitization and reconstruction have been all performed within the offline release 13 of ATHENA. The set of *H*→4*l* samples used in this analysis covers the range from 120 to 180 GeV. Simulation of pileup, cavern background and minimum bias events was performed by mixing with the Higgs signal at digitization level[42],[43]. An instantaneous constant luminosity of 10^{33} cm^{-2} s^{-1} and a center mass energy of 14 TeV are assumed.

The cavern background consists of thermalized slow neutrons and low energy photons[44]. The expected level of cavern background is increased by an overall "safety factor": in this analysis a safety factor of 5 was used.

The Higgs boson signal samples were generated exclusively by PYTHIA[33], while for the background samples various event generators were used. For the signal, PYTHIA calculates the cross-sections in leading order (LO) taking into account both gluon and vector boson fusion (VBF) diagrams. Next-to-leading order (NLO) effects are considered by scaling the total PYTHIA cross-sections. During generation, a 4-lepton filter was applied to the samples, requiring 4 true leptons with p_T>5 GeV/c within |η|<2.7. The filter acceptance and the cross-section as a function of the Higgs boson mass for the

Process	σLO·BR[*fb*]	σNLO·BR[*fb*]	Filter Acc.	Events
H[120]→4*l*	1.68	2.81	0.584	40K
H[130]→4*l*	3.76	6.25	0.633	40K
H[140]→4*l*	5.81	9.72	0.662	40K
H[150]→4*l*	6.37	10.56	0.685	10K
H[160]→4*l*	2.99	4.94	0.704	40K
H[165]→4*l*	1.38	2.29	0.712	40K
H[180]→4*l*	3.25	5.38	0.733	40K

Table 4.6: Monte Carlo signal data samples, 4-lepton (*e, μ*) filter acceptance, LO and NLO cross-sections,and number of events used in the analysis as a function of the Higgs boson mass in GeV (reported in square brackets). The cross-sections in the table include the branching ratio of the Higgs boson to *ZZ** and *Z/Z*→ll*, *l = e,* μ.

Process	Generator	σ·BR[*fb*]	Corrections	FA	Events
$q\bar{q} \to ZZ \to 4\,l$	PYTHIA6.3	158.8	+47.64	[4*l*]0.219	100K
$gg \to Zb\bar{b} \to 2\,lb\bar{b}$	AcerMC/ PYTHIA6.3	52030	+8640 ($q\bar{q} \to Zb\bar{b}$)	[4*l*]0.00942	430K
$gg \to Zb\bar{b} \to 2\,lb\bar{b}$	AcerMC/ PYTHIA6.3	52030	+8640 ($q\bar{q} \to Zb\bar{b}$)	[3*l*]0.147	200K
$g, q\bar{q} \to t\bar{t}$	MC@NLO/ Jimmy	833000		[4*l*]0.00728	400K
$q\bar{q} \to Z$ inclusive	PYTHIA6.3	$1.5 \cdot 10^{-6}$		[1*l*]0.89	500K

Table 4.7: Background samples, generators used, acceptance of the multi-lepton filter (FA), LO cross-section (except for $t\bar{t}$, which is NLO) and corrections applied. The number of events is given in the last column. For *ZZ*, *l = e, μ, τ* while for the rest *l = e*, μ. The relative errors on the filter acceptances (FA) are smaller than 0.4% .

Monte Carlo signal data sample are given in Table 4.6. The generators used, filter acceptance, the cross-section and the eventual correction due to effects of sub-processes not originally included in the generators for the Monte Carlo background data samples are given in Table 4.7. In both tables, the number of available MC events are shown in the last column.

4.2.2 Event Selection

The criteria selection used for the analysis are reported in Table 4.8.

Trigger	1μ20 (one muon with E>20 GeV), 1e22i (one electron isolated with E>22 GeV)
Event Preselection	Four leptons: *LooseElectrons*, STACO muons; p_T>7 GeV/c and |η|<2.5, at least two with p_T>20 GeV/c
Event selection	
Kinematic Cuts	2 pairs of same flavour opposite charge leptons. Electrons associated with the off-shell *Z* must be *MediumElectrons*. *Z*, *Z** and Higgs reconstruction: single quadruplet with |M_{ll1} − M_Z|<ΔM_{12}, M_{ll2}>M_{34} .
Isolation and vertexing cuts	Muon calorimetric isolation $(\sum E_T/p_T < 0.23)$. Lepton Inner detector track isolation $(\sum p_T/p_T < 0.15)$. Cut on maximum lepton impact parameter ($d_0/\sigma_{d_0} < 3.5$ for muons, $d_0/\sigma_{d_0} < 6.0$ for electrons)

Table 4.8: Summary of the analysis cuts for the *H*➙4 analysis. The two lepton pairs are denoted as M_{ll1} and M_{ll2}. The values of the mass window ΔM_{12} and of the cut M_{34} are defined in Table 4.9.

After the trigger and preselection cuts n-tuples were created from the AOD to be used in the analysis. Initially we used the AOD stored on CASTOR, and later the code was implemented to use the GRID facilities.

For the electron final state, only the track isolation in the inner detector was considered because calorimetric isolation is already part of the electron identification package. In the track isolation of the electron, to remove from the sum the tracks originating from conversions of bremsstrahlung photons, only tracks which have at least one hit in the B-layer (the innermost layer of the Pixel detector) are considered. Both for muons and electrons, all the isolation discriminant are normalized for the p_T of the considered lepton.

The cut on transverse impact parameter significance is different for electrons and for muons. For electrons, bremsstrahlung smears the impact parameter distribution, hence reducing the discriminating power of this cut with respect to muons. For electron tracks, the maximum impact parameter normalized to its error is required to be less than 6, while for muons less than 3.5.

The 4-lepton Higgs candidate mass reconstruction proceeds after selecting one single lepton quadruplet in an event. When more than one quadruplet is found, the one with a dilepton mass closest to the nominal Z mass is chosen. The resolution of the dilepton mass can be improved by applying a Z-mass constraint to the pair with a mass closest to the Z invariant mass. The used cuts are reported in Table 4.9. They have been optimized using the expected distributions for signal and backgrounds, and the expected dilepton resolution. In this table Z_1 is the dilepton with a mass closest to the Z mass, inside a prefixed windows centered on this mass, while Z_2 is the dilepton pair with the lower mass for which we require a minimum value.

H Mass (GeV)	Z_1 Mass window (GeV)	Z_2 Mass Cut (GeV)
120	±15	>15
130	±15	>20
140	±15	>30
150	±15	>30
160	±15	>30
165	±15	>35
180	±12	>40

Table 4.9: Cuts applied to the reconstructed leading and sub-leading Z masses

A final cut is applied to accept the events; the 4-lepton reconstructed mass has to be inside the mass window $m_H \pm 2\sigma_{mH}$, where m_H is the nominal Higgs mass and σ_{mH} is the experimental resolution.

Event selection results

The cut flow for the selection of a 130 GeV Higgs boson is shown in Tables 4.9 and 4.10, for signal and backgrounds respectively. The same is shown for the $t\bar{t}$ background in Table 4.11. In this case, the available MC statistics is not sufficient to determine the number of expected events, and only upper limits at 90% CL are set. The distributions of the reconstructed 4-lepton mass, obtained after all cuts, are shown in Figs. 4.7, 4.8, 4.9. for m_H 130, 150 and 180 GeV.

Selection Cut	$H{\to}ZZ{\to}4e$	$H{\to}ZZ{\to}4\mu$	$H{\to}ZZ{\to}2e2\mu$
Trigger Selection	94.7	95.3	95.7
Lepton Preselection	57.0	73.8	66.8
Lepton p_T	24.7	60.5	39.7
Z mass cuts	17.1	42.9	27.6
Calo Isolation	17.1	39.5	25.4
Tracker Isolation	16.5	38.1	24.7
IP cut	15.1	36.5	23.2
H Mass cut	12.5±0.3	31.4±0.5	19.2±0.4

Table 4.9: Fraction of events (in %) selected after each event selection cut, for each of the three decay channels, and for a 130 GeV Higgs.

Selection Cut	ZZ			$Zb\bar{b}$		
	$4e$	4μ	$2e2\mu$	$4e$	4μ	$2e2\mu$
Trigger Selection	96.6	96.6	96.6	91.4	91.4	91.4
Lepton Preselection	17.6	13.8	31.4	9.4	2.6	12.0
Lepton p_T	16.0	7.3	21.9	2.1	$1.1{\cdot}10^{-1}$	1.7
Z mass cuts	14.8	6.9	20.2	1.1	$4.7{\cdot}10^{-2}$	$8.4{\cdot}10^{-1}$
Calo Isolation	13.9	6.9	19.5	$8.5{\cdot}10^{-2}$	$1.3{\cdot}10^{-2}$	$1.2{\cdot}10^{-1}$
Tracker Isolation	13.6	6.8	19.2	$3.3{\cdot}10^{-2}$	$5.6{\cdot}10^{-3}$	$4.4{\cdot}10^{-2}$
IP cut	13.0	6.2	17.8	$1.1{\cdot}10^{-2}$	$1.6{\cdot}10^{-3}$	$1.8{\cdot}10^{-2}$
H Mass cut	$11.3{\cdot}10^{-2}$	$5.2{\cdot}10^{-2}$	$12.0{\cdot}10^{-2}$	$1.2{\cdot}10^{-3}$	$1.6{\cdot}10^{-3}$	$3.0{\cdot}10^{-3}$

Table 4.10: Fraction of background events (in %) selected after each event selection cut, for the each of the three decay channels, and for a 130 GeV Higgs boson.

Selection Cut	$t\bar{t}$ (%)		
	4*e*	4μ	2*e*2μ
Trigger Selection	71.0	75.1	75.1
Lepton Preselection	4.7	1.0	10.1
Lepton p_T	$7.3{\cdot}10^{-1}$	$6.8{\cdot}10^{-3}$	$5.8{\cdot}10^{-1}$
Z mass cuts	$2.0{\cdot}10^{-1}$	$1.6{\cdot}10^{-3}$	$1.0{\cdot}10^{-1}$
Calo Isolation	$1.6{\cdot}10^{-3}$	$1.6{\cdot}10^{-3}$	$5.4{\cdot}10^{-3}$
Tracker Isolation	$2.5{\cdot}10^{-4}$	$2.6{\cdot}10^{-4}$	$1.0{\cdot}10^{-3}$
IP cut	$<6{\cdot}10^{-4}$	$2.6{\cdot}10^{-4}$	$2.6{\cdot}10^{-4}$
H Mass cut	$<6{\cdot}10^{-4}$	$<6{\cdot}10^{-4}$	$<6{\cdot}10^{-4}$

Table 4.11: Fraction of events (in %) selected after each event selection cut for the $t\bar{t}$ background, for the each of the three decay channels, and for a 130 GeV Higgs boson. For small available statistics 90% CL limits are considered.
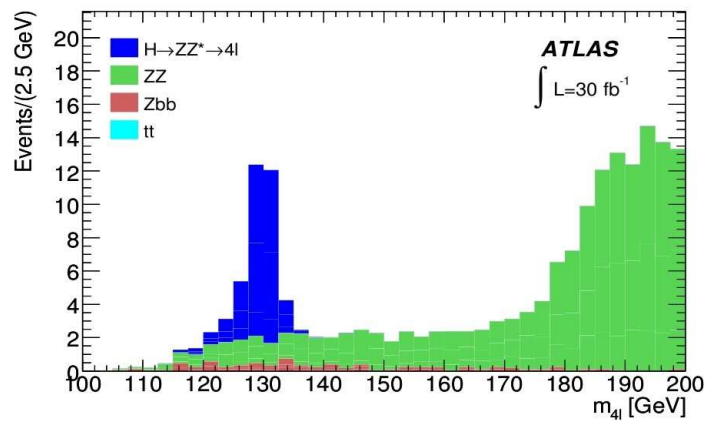
Fig. 4.7: Reconstructed 4-lepton mass for signal and background processes, in the case of a 130 GeV Higgs boson, normalized to a luminosity of 30 fb^{-1}.
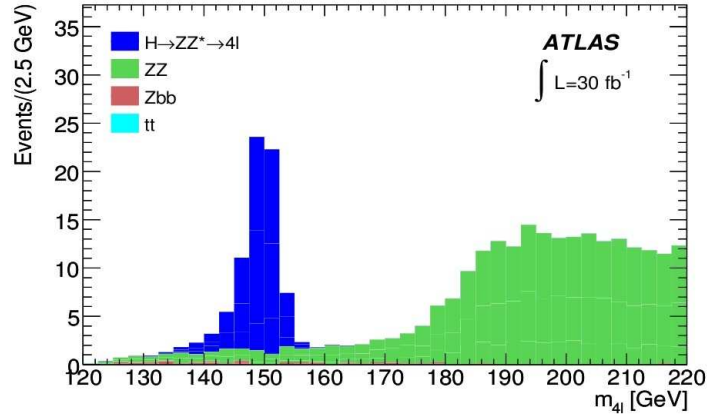
Fig. 4.8: Reconstructed 4-lepton mass for signal and background processes, in the case of a 150 GeV Higgs boson, normalized to a luminosity of 30 fb^{-1}.·
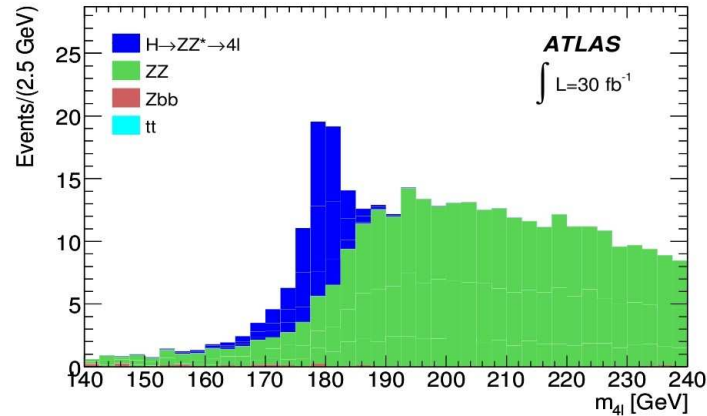
Fig. 4.9: Reconstructed 4-lepton mass for signal and background processes, in the case of a 180 GeV Higgs boson, normalized to a luminosity of 30 fb^{-1}.

4.2.3 Systematics

Central to the H➙4l analysis is the evaluation of the systematic uncertainties on quantities associated with background estimation and signal efficiency. I briefly present the main sources of these uncertainties.

Theoretical Uncertainties

The major theoretical uncertainties in the prediction of the inclusive background cross sections are the PDF uncertainties and uncertainties related to the QCD renormalization and factorization scales. Scale uncertainties reflect theoretical uncertainties due to the omission of higher order diagrams.

In the global analysis within which my work was made, the QCD scales have been independently varied in the range (0.5-2)×the energy scale of the process in the calculation of the NLO inclusive cross sections, for PDF and scale uncertainties; the PDF uncertainty has been evaluated by making use of 40 sets of PDF's for CTEQ6M.

Experimental Uncertainties

Systematic effects on the *H*➞*4l* analysis arise from experimental uncertainties related to the lepton reconstruction. The major contributions in the total systematic uncertainty in the *H*➞*4l* yield come from uncertainties in lepton energy scale, reconstruction and identification efficiency. In the general analysis, the impact of these uncertainties was studied by applying variations to offline reconstructed variables.

4.2.4 Background Extraction

Taking in account the theoretical and experimental uncertainties the significance can be obtained assuming that the background is know with negligible uncertainties. So, the estimation of the background in the candidate signal region is central to the *H*➞*4l* analysis. In this section two method to extract the background from data are presented. Afterwords, the uncertainties of the background were evaluated.

Two methods have been developed to estimate background in the signal mass region (defined as $m_H \pm 2\sigma_{mH}$). Both the methods aim to evaluate the irreducible *ZZ*➞*4l* background, and they employs some common elements: a MonteCarlo with full statistic for the irreducible background, several "data simulated" pseudo experiment (with signal and irreducible background) corresponding to the statistic expected in the data for about 30 fb^{-1}, and a function *f(M$_{ZZ}$)* which describe the shape of the irreducible background. In addition to the main irreducible background also the $Z b \bar{b}$ one has been included in the pseudo-experiments, even if its contribution is expected relevant only for low Higgs masses

In the pseudo experiments the event selection described in the previous sections has been applied and the final number of events in the signal region has been counted for each experiment ($N_{MW}^{obs} e$).

The function *f(M$_{ZZ}$)* is used to obtain the correct background shape by a fit of the overall Monte-Carlo statistics (after the usual event selection) in the full mass range (110-700 GeV). During the analysis different *f(M$_{ZZ}$)* were tried and for the final results was chose the following function:

$$f(M_{ZZ}) = \frac{p0}{(1+\frac{e^{p6-M_{zz}}}{p7})(1+\frac{e^{M_{zz}-p8}}{p9})} + \frac{p1}{(1+\frac{e^{p2-M_{zz}}}{p3})(1+\frac{e^{p4-M_{zz}}}{p5})}. \quad (4.1)$$

In this function the irreducible background has been modeled using a combination of Fermi functions which are suitable to describe both the plateau in the low mass region and the broad peak corresponding to the second *Z* coming on shell. The first plateau, in the region where only one of the two *Z* bosons is on shell, is modeled by the first term, and its suppression, needed for a correct description at higher masses, is controlled by the *p8* and *p9* parameters. The second term in the above formula accounts for the shape of the broad peak and the tail at high masses. This function can describe with a negligible bias the *ZZ* background shape with good accuracy over the full mass range. The $Z b \bar{b}$ contribution is relevant to the background shape only when searching for very light Higgs boson (in this study, only at m_H = 120 GeV). In this case, an additional term is added to the *ZZ* continuum, with a functional form similar to the second part of equation. In the figures 4.1 and 4.11 the mass invariant distribution for a pseudo experiment., fitted by *(4.1)* outside the mass window region.
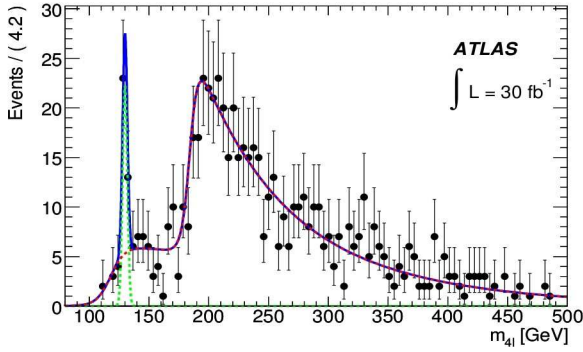
Fig. 4.10: A pseudo-experiment corresponding to 30 fb⁻¹ of data for a Higgs boson mass of 130 GeV. The functions fitting the signal (a gaussian) and the background (function 1) are shown.
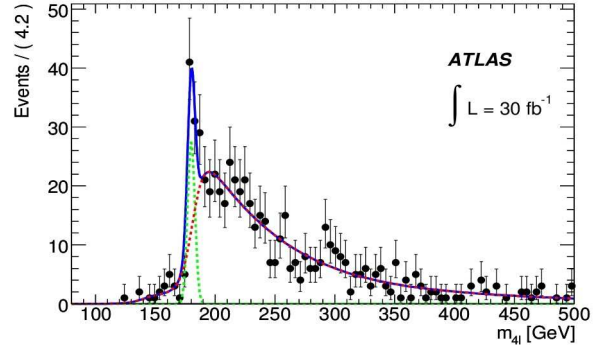
Fig. 4.11: A pseudo-experiment corresponding to 30 fb⁻¹ of data for a Higgs boson mass of 180 GeV. The functions fitting the signal (a gaussian) and the background (function 1) are shown.

Tau method

The first method, or tau method, consists of calculating, using the full MC statistics, the ratio $\tau = \frac{B_{MW}}{B_{SB}}$ between the background events in the signal mass

window (B_{MW}) and those in the regions outside the signal mass window, or sidebands, (B_{SB}). We obtained tau both counting the events or fitting the background with the function (4.1) and evaluating the number of events from the fit. The two evaluation of tau gave the same significance as result.

For each pseudo-experiment *i*, the background level in the signal mass window is estimated as:

$$B_{MW}(i) = \tau \times N_{SB}^{OBS}(i) \qquad (4.2)$$

and the signal as:

$$S_{MW}(i) = N_{MW}^{OBS}(i) - B_{MW}(i). \qquad (4.3)$$

where $N_{SB}^{OBS}(i)$ is the number of events observed in the sideband region and $N_{MW}^{OBS}(i)$ is the number of events observed in the mass window.

Sideband Method

In the second method, for each pseudo-experiment a fit is performed only in the sideband region using the previous background function (4.1). Only the normalization of the function is floating in the fit and the other parameters have been taken from the results of the fit on the overall Monte-Carlo statistics. The background level in signal mass region is obtained extrapolating and integrating the function in this region.

Results

The estimate of background from pseudo-experiments gives an estimate of the background statistical fluctuations that have to be accounted in the significance calculation. This statistical uncertainty is defined as the ratio between the r.m.s. of the background estimated in the signal mass window and the mean of it, both evaluated using all the pseudo-experiments at a fixed Higgs mass point. The uncertainty obtained for the sideband method is no more than 6% over the full mass range and the one of the tau method is no more than 5%.

The impact of this uncertainty on the significance has been hen evaluated using the profile likelihood method for counting experiments reported in [21]. The results for 130, 150 and 180 GeV Higgs boson mass are summarized in Table 4.12. As can be seen, the two methods have similar significances.

Method	Background error	130 GeV	150 GeV	180 GeV
Sideband	from fit	6.6	14.0	5.9
τ-ratio	from τ-ratio	6.7	14.0	5.8

Table 4.12: The signal significance for various Higgs boson masses, obtained including the background uncertainties from the sideband fit and the τ-ratio methods.

Chapter 5

Analysis on the background for the *Z*→µµ channel

Electroweak vector bosons decaying into leptonic final states are among the processes of primary interest in the early data analysis at LHC. These are produced with high rates and are characterized by the clean signatures of their high p_T leptons in the final state. The determination of their inclusive cross-sections represents therefore one of the first benchmark measurement for ATLAS. In particular, the measurement of their ratio to a precision of few percent will be a fundamental test of our understanding the detector performance and of its capability of delivering high quality and stable data.

At the Large Hadron Collider, the production of *W* and *Z* bosons will be a relevant process because of their large cross section and very clean signature, given by one isolated charged lepton with missing transverse energy (for *W* production) and by two isolated charged leptons with opposite charges (for *Z* production).

In this chapter, in section 1 I will give a general explanation on the measurement of the Z→µµ inclusive cross section, and in section 2 I will present my work on some data driven methods to correctly evaluate the contributions of the main background signals for the Z→µµ channel. I made this analysis as part of a collaboration of Italian groups.

5.1 The Measurement of the Z→μμ Inclusive Cross Section

5.1.1 Background

The leptonic decay of the Z is boson is surely one of the cleanest signatures among Standard Model processes and with the additional constraint of the invariant mass variable, there is no background process that can in principle give serious problems to the detection of such a signal. Nevertheless, some processes have similar final state event topologies to those of the signal samples and others can fake similar topologies when a non-lepton object within the event is misidentified as a muon. The main background channels for the muonic decay of the *Z* boson can be summarized as:

- QCD background: the main source of energetic muons (p_T>10 GeV/c) are the decays of *b*-quarks. Muons originating from QCD events appear highly non-isolated in the detector, as they are produced along with many other particles. Hence, this kind of background can be reduced by requiring the isolation of the muon; this isolation can be described by the number of tracks (NID) and the p_T -sum (pID) of these tracks within a cone in the η-φ plane ($\Delta R = \sqrt{(\Delta\eta2 + \Delta\varphi2)}$).

- *Z*→ττ events in which the τ leptons subsequently decay into a muons.

- top quark background: Due to the high collision energy of LHC, the production of top-quark pairs has a cross section in the order of the *Z* cross section. The top-quarks decay into a *W* boson and *b*-quark. The *W* boson and the *b*-quark can decay further into muons, which also might fake the signal process.

- *W*→μν.

- *W*→τν events in which τ lepton subsequently decays into a muon.

5.1.2 Datasets

The analysis described is based on Monte Carlo simulated data at 10 TeV from the ATLAS MC08 official production[45]. Main backgrounds from QCD and ealactroweak processes are considered. At the time the analysis started (late 2008) only small samples (few pb^{-1}) of simulated $b\bar{b}$ and $c\bar{c}$ QCD processes where available, due to the overwhelming cross sections. We then started a private production, after the approval of the Monte Carlo production group, of a large sample of events. In order to speed up the production we

decided to simulate the events with ATLFAST-II simulation (full reconstruction of tracking detectors and fast simulation of the calorimeters). Moreover, to further reduce the simulation resources needed, the generated sample has been filtered requiring at least one high-p_T muon (p_T>15 GeV/c) in the final state. The electroweak backgrounds are taken into account through the processes $W→μν$, $Z→τ^+τ^-$ and $W→τν$. In the last two samples at least one tau leptonic

sample	Process	Generator level cuts	$\epsilon \cdot \sigma$ (pb)	L (pb^{-1})
$Z→μμ$	$pp→Z/γ^*→μμ$; $\sqrt{s}$ >60 GeV	≥1 e or ≥1 μ; |η|<2.8	1098	200
$W→μν$	$pp→W→μν$	≥1 e or ≥1 μ; |η|<2.8	10352	165
DY$μμ$	$pp→Z/γ^*→μμ$; 10< $\sqrt{s}$ <60 GeV	≥1 e or ≥1 μ; |η|<2.7, p_T >10 GeV/c	730	200
$Z→ττ$	$pp→Z/γ^*→ττ$; $\sqrt{s}$ >60 GeV	none	1128	176
DY$ττ$	$pp→Z/γ^*→ττ$; 10 < $\sqrt{s}$ < 60 GeV	≥1 e or ≥1 μ; |η|< 2.7, p_T >10 GeV/c	30	200
$W→τν$	$pp→W→τν→lνν$; l = μ, e	≥1 e or ≥1 μ; |η|<2.8	4128	69
$t\bar{t}$	$pp→$ $t\bar{t} X$	≥1 leptonic W decay (e, μ, τ)	206	200
$b\bar{b}$	$pp→$ $b\bar{b} X$	1μ p_T>15 GeV/c, |η|<2.5	90000	82
$c\bar{c}$	$pp→$ $c\bar{c} X$	1μ p_T>15 GeV/c, |η|<2.5	20000	39

Table 5.1: List of data samples used in analysis together with their generator-level cuts, cross-sections and processed integrated luminosity.

decay in generation was required. The top quark contribution has been considered using a top-pair sample. Other sources of background (as $K/π$ decay in flight and shower muons from di-jets events) have been neglected: these events have huge cross sections and only very small samples were produced. In order to study the impact of a limited knowledge of sub-detector alignments and calibrations in first data, a set of misaligned samples have been simulated for signals and dominant background processes. The whole list of the datasets used is in Table 5.1.

The analysis is performed in the scenario of an integrated luminosity of 15 pb^{-1}. Each sample was divided in two parts: a pseudo-data sample of the size corresponding to the chosen integrated luminosity, and a MonteCarlo sample for all other events. The analysis was done with the EWPA framework running over data samples on the GRID Tier2 infrastructure; analysis tasks which required full data granularity, detector geometry and conditions databases accesses were executed inside the Athena framework. A pre-filtering of events and a selection of the level of details for each analysis object was

applied at this point. The outcome was a light D3PD (10 kBytes/event) for each channel. These D3PD were then processed locally to make final analysis selections, figures and tables.

Z➙µµ selection		
Cut	Object	Value(s)
Acceptance	at least 2 Z muons	$p_T > 15\, GeV/c$, $|\eta| < 2.5$
Kinematic	2 combined tracks (STACO), charge	$p_T > \{15, 17.5, 20, 22.5, 25\}\, GeV/c$, $|\eta| < 2.5$ $q_1 \cdot q_2 > 0$
Isolation	p_T - normalized ID cone (0.4) activity	$\sum p_T^{ID}/p_T < \{0.2, 0.6, 1.0, 1.4, 1.8, 2.2\}$
Trigger	event trigger EF trigger track	µ10, µ20 associated over threshold

Table 5.2: Selection cuts used in the Z➙µµ analysis.

5.1.3 Standard Selections for Cross-Section Measurement

The muon decay channel of *Z* bosons is characterized by two high energetic and isolated muons tracks in the final state. The muon tracks are reconstructed separately in the Muon Spectrometer and in the Inner Detector; then a combined track is built for both the systems, taking into account the energy loss in thecalorimeter system (STACO muons). The signal selection is then based on the requirement of offline high-p_T reconstructed tracks, combining the information from the muon detectors and the internal tracker. Since muons coming from QCD events are likely to have a larger activity in a cone around the track, an isolation
requirement is applied to reject those events.

Events are selected starting from the muon trigger stream applying two possible trigger selections: µ10 or µ20 (events with at least one muon that fires the 10 or 20 GeV trigger threshold are filtered). The lower threshold is foreseen to be used during the start-up phase; as soon as the LHC luminosity will increase the higher one will then be adopted. The impact on the analysis of this switch is expected to be negligible provided that the offline p_T cuts are applied over the trigger threshold. In Table 5.2 the studied selection strategies are summarized.

To study the stability of the measurements a scan over different values of the kinematic and isolation cuts was performed (both tracks were required to fulfill the same cut: e.g. both track with $p_T > 22.5$ GeV/c).

The isolation selection is based only on the tracking system data, to not

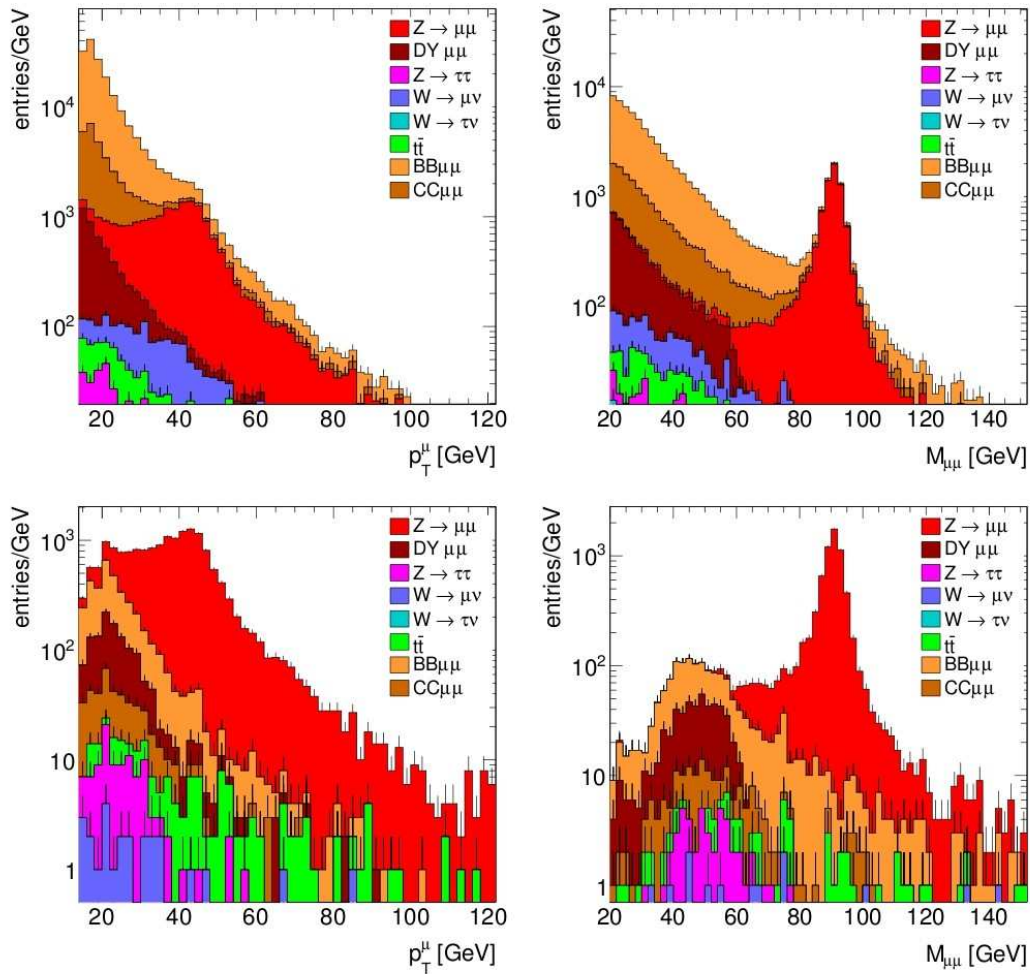**Fig. 5.1:** Muon transverse momentum (left) and *Z* invariant mass (right) for all (top) and final selected (bottom) events.

rely on calorimeter signals, whose calibration will be less precise during the initial phase. The variable used is obtained normalizing the p_T sum of inner tracks in a cone $\sqrt{\Delta\eta^2+\Delta\phi^2}<0.4$ to the transverse momentum of the candidate track $(\sum_{cone}^{0.4} p_T^{ID}/p_T)$. As explained in section 5.2.1, this choice allows to have an isolation variable that scales with p_T. This scaling property can be used to estimate Z background shape from data by means of isolation rejected events.

The *cut-flow* efficiencies, referred to the benchmark point (p_T>15 GeV/c, $\sum p_T^{ID}/p_T < 1.4$) for Z selection are shown on table 5.3. The cuts chosen here for Z identification have been loosened to get a reasonable background statistic entering the distribution. A fit procedure will be used to determinate the correct normalization of the background contributions. The distribution for the muon transverse momentum and Z invariant mass of selected events in thebenchmark point are shown in Figure 5.1.

The measurement of the production cross section is driven by the following formula:

$$\sigma(pp \to Z \to \mu\mu)=\frac{N-B}{L\cdot\epsilon\cdot A} \qquad (5.1)$$

where N is the number of measured events from data, B is the background contamination, L the integrated luminosity analyzed, ϵ is the overall selection efficiency and A the acceptance of the cinematic selection. The total uncertainty in the cross section evaluation is then factorized in the different terms:

$$\frac{\delta\sigma}{\sigma}=\frac{\delta N \oplus \delta B}{N-B}\oplus\frac{\delta L}{L}\oplus\frac{\delta A}{A}\oplus\frac{\delta\epsilon}{\epsilon} \qquad (5.2)$$

The uncertainty on the **number of events**, δ*N*, is a statistical uncertainty, and it decreases with increasing luminosity.

The **luminosity** L will be measured with various methods (at the LHC there are several dedicated experiments for the measurement of instantaneous luminosity). The uncertainty on this parameter, δ*L*, is expected to decrease through improved understanding of the LHC beam parameters and of the ATLAS luminosity detector response.

Signal and **background** yields (*N* - *B* and *B*) are extracted by means of fits on Z invariant mass. Here the main source of uncertainties come from the modeling of signal and background shapes and from detector resolution effects. The method developed in this analysis concentrate on this modeling.

Once signal events are identified from data a set of corrections that depend on trigger, reconstruction and selection need to be applied to rescale the number of measured events to absolute values. These corrections are divided in acceptance and efficiency.

The **acceptance** *A* is due to the geometrical coverage of the detector and to the kinematics of the selection; its uncertainty come mainly form theoretical effects. Acceptance has to be calculated from Monte Carlo, by imposing the same cuts on pseudorapidity and transverse momentum (η^0, p_T^0) that are used to select the signal in the analysis. The acceptance is then the ratio between the events that have passed this selection, and the inclusive set of events:

$$A = \frac{N^{p_T > p_T^0, |\eta| < \eta^0}}{N^{inclusive}} \qquad (5.3)$$

where $N^{inclusive}$ is the number of events from the Monte Carlo generator. In this way the acceptance is strongly dependent on the phase-space distribution of the sample and its decay products, and hence it strongly depends from the theoretical model that has been used to generate the sample. The theoretical predictions for the acceptance, in fact, are based on different models, describing different aspects of the theoretical understanding of the proton-proton collisions and the subsequent production and decay of vector boson. Not only the acceptance itself, but also its corresponding theoretical uncertainty depends on the chosen cuts.

The **efficiency** is instead related to the probability that each event fulfill the selection criteria outlined in Table 5.2. The simplest way to evaluate this number is to calculate it using events reconstructed from MonteCarlo samples with a realistic simulation of detector reconstruction. This approach is referred to as *cut-flow* and it takes into account (by construction) all the possible correlations between reconstructed tracks. It can however suffer of potentially large systematic uncertainties depending how well the physical process is described. The c*ut-flow* efficiency needs therefore to be weighted by a correction factor that has to be data-driven. This correction is called the *event weight* and it is defined as:

$$w = \sum_{\{mc\}} \frac{\epsilon^{data}(p_T, \eta)}{\epsilon^{mc}(p_T, \eta)} \qquad (5.4)$$

where ϵ for data and MonteCarlo samples are derived from the measured single particle efficiencies. These are measured in function of event kinematic variables. The efficiencies can be divided in three categories: reconstruction,

isolation and trigger. Following steps and labels are defined:

- $\epsilon_{ms|id}$: efficiency of the Muon Spectrometer standalone reconstruction given the Inner Detector track;
- $\epsilon_{cb|ms}$: efficiency of the combined muon reconstruction given the standalone spectrometer track;
- ϵ_{iso}: efficiency of the isolation cut given the combined track;
- ϵ_{trig}: efficiency of the trigger selection given combined and isolated track;

The absolute muon combined reconstruction efficiency is then obtained by the product $\epsilon_{ms|id} \times \epsilon_{cb|ms}$: the probability to have an Inner Detector track is taken in account by the presence of a combined track. In this way also the matching efficiency between Inner Detector and Muon Spectrometer tracks is included. The only correlation in reconstructing muon tracks between Inner Detector and Muon Spectrometer arise form the geometrical acceptance; so $\epsilon_{ms|id} = \epsilon_{ms}$ could be assumed in the fiducial region $|\eta| < 2.5$.

The total efficiency of the selection is then computed with:

$$
\begin{aligned}
\epsilon^{data,mc} &= \epsilon^{+}_{ms|id} \cdot \epsilon^{+}_{cb|ms} \cdot \epsilon^{+}_{iso} \\
&\quad \cdot \epsilon^{-}_{ms|id} \cdot \epsilon^{-}_{cb|ms} \cdot \epsilon^{-}_{iso} \\
&\quad \cdot \left[1 - (1 - \epsilon^{+}_{trig}) \cdot (1 - \epsilon^{-}_{trig}) \right] \\
&= \epsilon_{ms|id} \cdot \epsilon_{cb|ms} \cdot \epsilon_{iso} \cdot \epsilon_{trig}
\end{aligned}
\tag{5.6}
$$

where for the trigger efficiency it is considered the fact that a single muon trigger sector must be fired.

Cuts(%)	Z→μμ	W→μν	DYμμ	Z→ττ	W→τν	$t\bar{t}$	Bμμ	Cμμ
Comb.	44.3(1)	0.401(5)	55.7(1)	1.16(3)	0.158(9)	8.6(1)	7194(10)	3.53(2)
Charge	44.3(1)	0.401(5)	55.7(1)	1.16(3)	0.158(9)	8.6(1)	7194(10)	3.53(2)
Kine	44.2(1)	0.0123(9)	5.80(6)	0.23(1)	0.003(1)	0.323(2)	0.323(2)	0.166(5)
Iso	44.2(1)	0.0083(7)	5.77(6)	0.23(1)	0.003(1)	0.145(1)	0.145(1)	0.53(3)
Trigger	41.9(1)	0.0063(6)	3.66(5)	0.174(10)	0.0010(7)	0.089(1)	0.089(1)	0.031(2)
Events	6902(17)	9.7(10)	401(5)	29(2)	0.6(4)	65(2)	1196(15)	135(9)

Table 5.3: *cut flow* efficiencies for Z analysis corresponding to the benchmark point (p_T>15 GeV/c, $\sum p_T^{ID}/p_T$ <1.4). Efficiencies are calculated using MonteCarlo samples statistics while number of events are given for 10 pb^{-1} integrated luminosity (statistical uncertainty only).

Finally the event selection efficiency weighted with data driven correction is given by

$$\epsilon = \epsilon^{cut-flow} \cdot w \qquad (5.7)$$

In order to determine the muon spectrometer reconstruction efficiencies directly from data, the so-called "tag-and-probe" method can be used, using the Z→µµ channel: the events Z→µµ are identified without using the muon spectrometer for the "probe" muon, then the existence of a reconstructed muon in the spectrometer is checked.

5.2 Selection of Events and Signal Counting

MonteCarlo studies tell us that the contribution of Background Events under the *Z* peak can be reduced to below 1%[46]. However, this prediction is affected by large theoretical uncertainties both on QCD spectra and absolute cross sections, and by the uncertainty of the alignment of the detector during the first data taking period. Therefore, some methods for estimate the background from data were developed. These methods use events rejected by isolation cuts, events with same sign dimuons, or events in which there is one muon and one electron in the final state.

In the following, the invariant mass spectrum of the QCD events is derived from data control samples, and I use this shape, together with the MonteCarlo prediction for the shape of the signal events, to fit the distribution obtained from the data sample. From the fit, the number of signal events needed for the measurements can be extracted. Moreover, the χ^2 of the fit will quantify the goodness of the description of the data spectrum.

On a complementary approach, the number of selected events in the control sample can be used (for instance same signs dimuons, or muon-electron final state events) to predict the absolute value of background events in our signal sample. To do this, the ratio of events expected in the control sample and in the signal sample is needed (for instance, the ratio of opposite and same sign events). In first approximation, this number can be taken from the MonteCarlo.

5.2.1 Definition of the Isolation Cut

As already mentioned, one way of extracting the dimuon invariant-mass distribution from $b\bar{b}$ and $c\bar{c}$ events from data is to obtain it from events rejected by the track isolation requirement. However, one has to be sure that the isolation cut does not distort the invariant mass distribution; in other words, that the isolation variable and the invariant mass are not correlated. On Figure
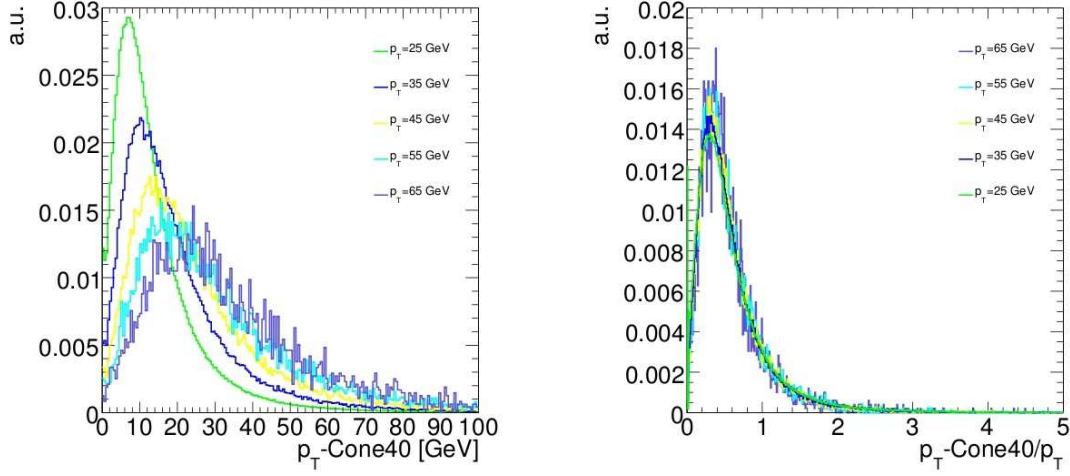
Fig. 5.2: Left: $\sum p_T^{ID}$ variable for different values of p_T of the muon for $b\bar{b}$ events. Right: Same as in the left plot, but for the $\sum p_T^{ID}/p_T$ variable. The distribution are normalized to the same number of events.

5.2 (left) I show, for $b\bar{b}$ events, the so called $\sum p_T^{ID}$ (the sum of the p_T's of all the tracks within a 0.4 cone around the muon) for different values of the p_T of the muon. The strong correlation is due to the fact that essentially all the particles within the cone come from the decay of the same b hadron. So their p_T are all correlated and proportional to the same Lorentz factor γ. Normalizing this variable to the p_T of the muon, the γ factor cancels out. In Figure 5.2 (right), the distribution $\sum p_T^{ID}/p_T$ for several values of the muon p_T shows the small correlation between these two variables.

Using this last definition of isolation variable, I performed the *Z* selection and compared the invariant mass distribution of the events rejected by the isolation cut with the $b\bar{b}$ and $c\bar{c}$ components of the selected events. This comparison is shown in Figure 5.3, in linear (left) and logarithmic scale (right). The events are selected according to the cuts listed in Table 5.2 for the benchmark point p_T>15 GeV/c and $\sum p_T^{ID}/p_T$ <1.4. The distribution for $b\bar{b}$ and $c\bar{c}$ selected events is shown with markers, while the distribution of all the events rejected by the isolation cut is shown as a stack plot. The two distributions are normalized to the (same) number of selected events. Rejected events are dominated by $b\bar{b}$ and $c\bar{c}$. A small contribution due to $t\bar{t}$ is visible, and few *Z*→μμ events appear close to 90 GeV (red histogram). The agreement is quite good both for the linear and log scales.

It will be possible to perform a direct check of this procedure on real data comparing the invariant mass distribution of dimuons with the same sign (same sign (SS) events). This is shown in Figure 5.4, where the distributions

for events selected and rejected in the MonteCarlo samples are compared. This time the markers represents all the SS events selected by the isolation cut (so not only the QCD component) and the stack plot represent all the events rejected by the isolation cut. The agreement is again good. This check allows to test directly on the data the absence of correlation between invariant mass and isolation variable.

5.2.2 Fit with QCD Background Estimated from Isolation Rejected Events

In this section the method described in the previous section is exploited to extract the QCD background shape from the data, and it is used to fit the pseudo-data distribution finding the weight of the QDC component. The fit is performed using a maximum bin likelihood [47]. Dimuon are selected with p_T>15 GeV/c and $\sum p_T^{ID}/p_T$ <1.4. The pseudo-data sample has 8450 selected events corresponding to 15 pb^{-1} at 10 TeV. The true fractions in the pseudo-data samples are shown in Table 5.4.
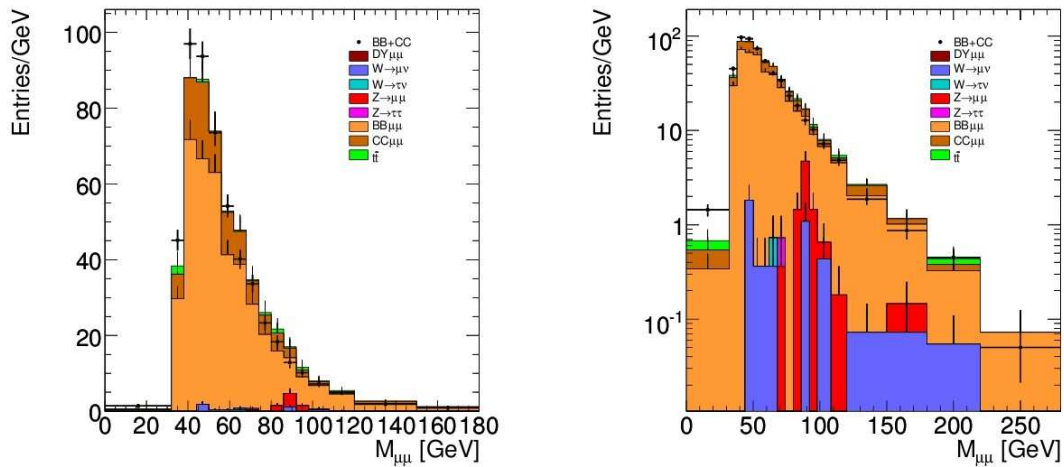
Fig. 5.3: Comparison of dimuon invariant mass distribution for events rejected by the isolation cut for all the channels (stack plot) and $b\bar{b}$ and $c\bar{c}$ selected events (markers). The distributions are normalized to the number of selected QCD events. Left: liner scale. Right: log scale.
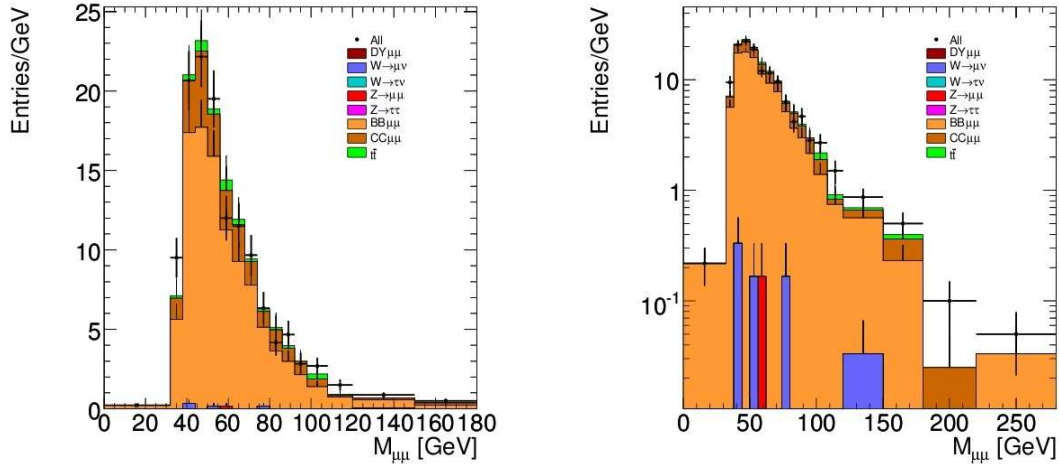
Fig. 5.4: Comparison of the dimuon invariant mass distribution for SS events rejected by the isolation cut for all the channels (stack plot) and SS selected events (markers). Left: linerar scale. Right: log scale.

Channel	True Fraction (%)
$Z{\to}\mu\mu$ (M > 60 GeV)	81.1
Drell-Yan µµ (M < 60 GeV)	4.4
$Z{\to}\tau\tau$	0.49
$W{\to}\mu\nu$	0.15
$W{\to}\tau\nu$	0
$b\bar{b}$	11.9
$c\bar{c}$	1.3
$t\bar{t}$	0.66

Table 5.4: Fractional composition of the pseudo data sample after the selection. The total number of events is 8450.

First, the fit is performed using MonteCarlo distributions for $b\bar{b}$ and $c\bar{c}$ events (Figure 5.5). In this case, only two free parameters have been used: the fraction of electroweak and $t\bar{t}$ events; the fraction of $b\bar{b}$ and $c\bar{c}$ events. Within each fit component, the ratio of channel fractions is kept fixed according to their cross section and the MonteCarlo prediction of the large uncertainty on the $b\bar{b}$ and $c\bar{c}$ cross sections in LHC. On the contrary, ratio of cross section for W and Z is known to few percent and the branching ratio at per mil level. Finally, the cross section for $t\bar{t}$ production has an uncertainty about 12%[41]. The fit χ^2 is 61 with 59 degrees of freedom.
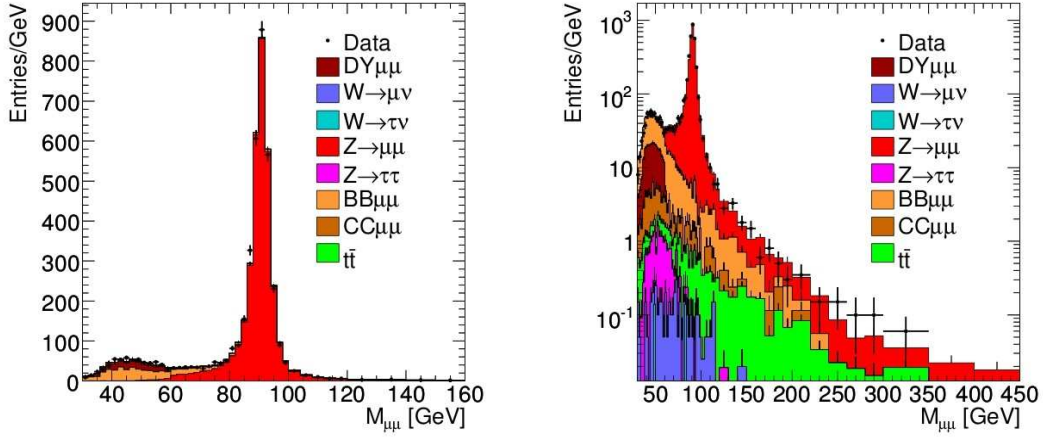
Fig. 5.5: Fit performed on pseudo-data sample using MonteCarlo shapes for the background and signal distributions.

Channel	Fit Fraction (%)
$Z{\to}\mu\mu$ (M > 60 GeV)	81.2 ± 1.1
Drell-Yan $\mu\mu$ (M < 60 GeV)	4.15 ± 0.22
$Z{\to}\tau\tau$	0.346 ± 0.064
$W{\to}\mu\nu$	0.108 ± 0.036
$W{\to}\tau\nu$	$(6 \pm 8) \times 10^{-3}$
$b\,\bar{b}$	12.05 ± 0.59
$c\,\bar{c}$	1.39 ± 0.14
$t\,\bar{t}$	0.713 ± 0.092

Table 5.5: Result of the fit performed using MonteCarlo prediction for the background and signal distributions. The fit have χ^2 equal to 61 and 59 degrees of freedom.
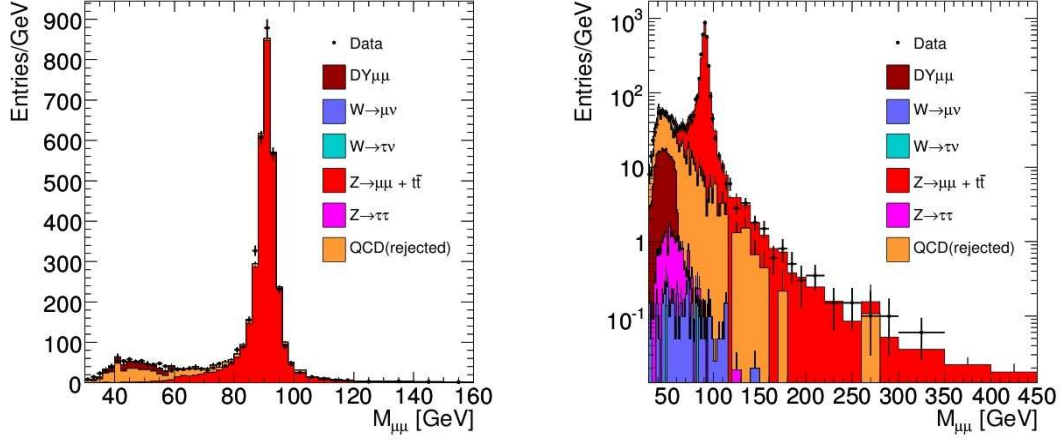
Fig. 5.6: Fit performed on pseudo-data sample using the Heavy-Q shape of the invariant mass distribution obtained from the events rejected by the isolation cut.

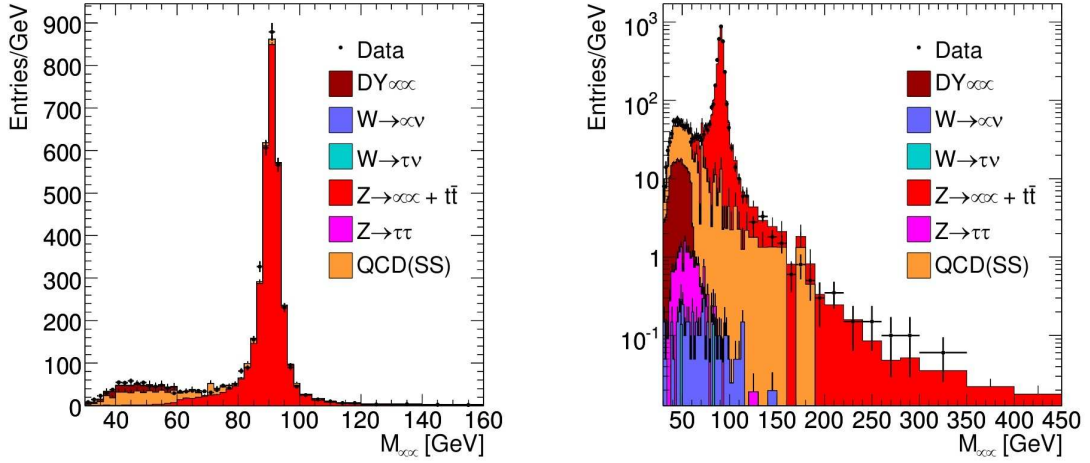| Channel	Fit Fraction (%)
$Z→µµ$ (M > 60 GeV)	80.4 ± 1.1
Drell-Yan µµ (M < 60 GeV)	4.10 ± 0.22
$Z→ττ$	0.343 ± 0.064
$W→µν$	0.107 ± 0.036
$W→τν$	$(7 \pm 9) \times 10^{-3}$
$b\bar{b} + c\bar{c}$	14.30 ± 0.87
$t\bar{t}$	0.706 ± 0.092

Table 5.6: Result of the fit performed using as QCD shape events rejected by the isolation cut. The fit have χ^2 equal to 65 and 59 degrees of freedom.

Then, the fit is performed using the $b\bar{b}$ and $c\bar{c}$ components, the shapes obtained from the pseudo-data sample rejected by the isolation cut only (Figure 5.6). There is also a good agreement between the true fractions in Table 5.4 and the fractions reported in Table 5.6. The statistical error on the number of signals events (8450*0.011 = 93) is slightly larger than the Poissonian error (82).

5.2.3 Background Estimate with Same-Sign Dimuon Events

An alternative way of extracting the QCD background shape and yield is to study the invariant mass distribution of SS (same sign) dimuon events. Here, I apply the same selection as for opposite-sign dimuon but requiring the same charge. In Figure 5.7 the invariant mass distribution of SS events is compared with the same distribution but for $c\bar{c}$ and $b\bar{b}$ with opposite charge sign. As in the previous case, I normalized the two distributions to the same number of events (so no absolute prediction is done for the moment). The agreement is quite good.

The fit is performed for events selected as in section 5.2.2 using the same MonteCarlo and pseudo-data samples. The result is shown in Figure 5.8. In this case we use for the $c\bar{c}$ and $b\bar{b}$ background the shape obtained from SS dimuon events from the pseudo-data sample (QCD(SS) component). The electroweak components are treated as in the previous case. The $t\bar{t}$ component is kept constant with respect to the electroweak components, according to the MonteCarlo estimate.

The fit fractions are shown in Table 5.7. The χ^2 is about 59 with 59 degrees of freedom. Again a good agreement is found comparing with the true fractions in Table 5.4.
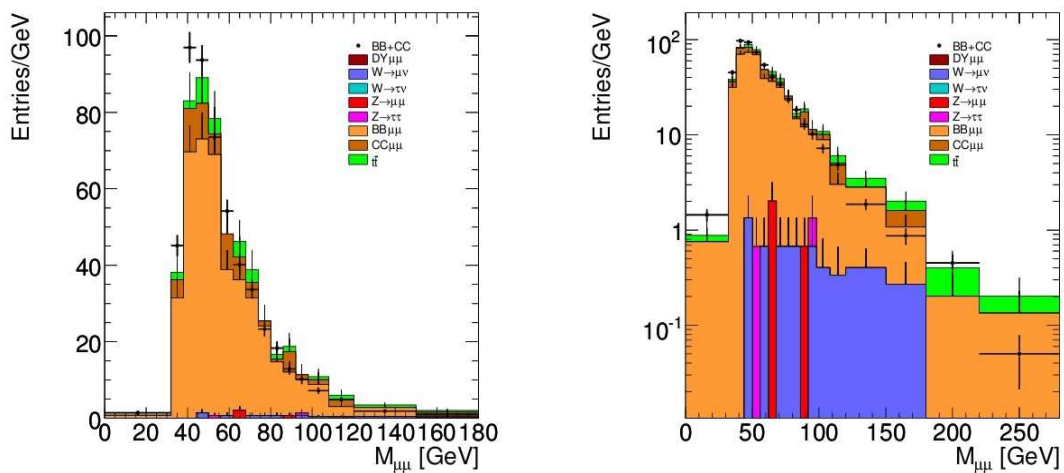
Fig. 5.7: Comparison of the dimuon invariant mass distribution for SS events for all the channels (stack plot) and OS $b\bar{b}$ and $c\bar{c}$ selected events (markers).

Fig. 5.8: Fit performed on pseudo-data sample using the Heavy-Q shape of the invariant mass distribution obtained from the events with same sign muons.

Channel	Fit Fraction (%)
Z→μμ (M > 60 GeV)	80.5 ± 1.2
Drell-Yan μμ (M < 60 GeV)	4.11 ± 0.22
Z→ττ	0.343 ± 0.064
W→μν	0.108 ± 0.036
W→τν	$(7 ± 9) × 10^{-3}$
$b\bar{b}$ + $c\bar{c}$	14.35 ± 0.90
$t\bar{t}$	0.707 ± 0.091

Table 5.7: Result of the fit performed using the QCD shape obtained from SS dimuon events. The fit have χ2 equal to 59 and 59 degrees of freedom.

5.2.4 Estimate of *Z*→ττ and $t\bar{t}$ Background from µ-*e* Events

It is possible to estimate the background shape for the contributions to *Z*→ττ and $t\bar{t}$ events, using the events with a muon and an electron in the final state. while the contribution from $b\bar{b}$ and $c\bar{c}$ is extremely reduced by the isolation cuts. Since the W boson decays with equal probability to muon and electron, after correcting for selection efficiency, the number of eµ events is expected to be twice the number of µµ events, both for *Z*→ττ and $t\bar{t}$ events. Hence, both the shape and the absolute number of events can be estimated directly from the data as

$$Events_{\mu e} = 2\, Events_{2\mu}. \qquad (5.8)$$

In the following we will focus on the shape determination of the background.

The selection applied is similar to the one applied for the selection of *Z*→µµ events; I look for a muon and an electron with p_T>15 GeV/c and |η|<2.5. The muon must also fire a trigger sector (µ20).

A number of µe events which is greater than expected is found. This is due to the great number of fake electrons, as it was not applied any identification criteria on the electron used. However, the shape of the reconstructed invariant mass is still compatible with the dimuon case. This can be explained with the usually high energy retained by the fake electron signal, which permits to preserve the shape. To reduce the number of events with fake electrons, *loose, medium*, and *tight* identifications are checked. The isolation of the muon is requested by requiring a $\sum p_T^{ID}/p_T$ less than 0.2.

In Figure 5.9 I show the comparison of the invariant mass distribution of the selected µe events, with the expected distribution for dimuons from Z→ττ and $t\bar{t}$ samples. The distribution are normalized to the number of dimuon events. The comparison is shown for different electron selections: all the candidate electrons (top left); Loose electron (top right); Medium electron

µ*e* events selection		
Cut	Object	Value(s)
Kinematic	1 combined muon track (STACO) 1 electron track	p_T>15, $\lvert \eta \rvert$<2.5
Isolation	P_T – normalized ID cone (0.4) activity for the µ	$\sum p_T^{ID}/p_T<\{0.2, 0.6, 1.0, 1.4, 1.8, 2.2\}$
Trigger	event trigger	µ10
Identification	Electron ID	*Loose, Medium* or *Tigh*

Table 5.8: Selection cuts used in the µ*e* background analysis

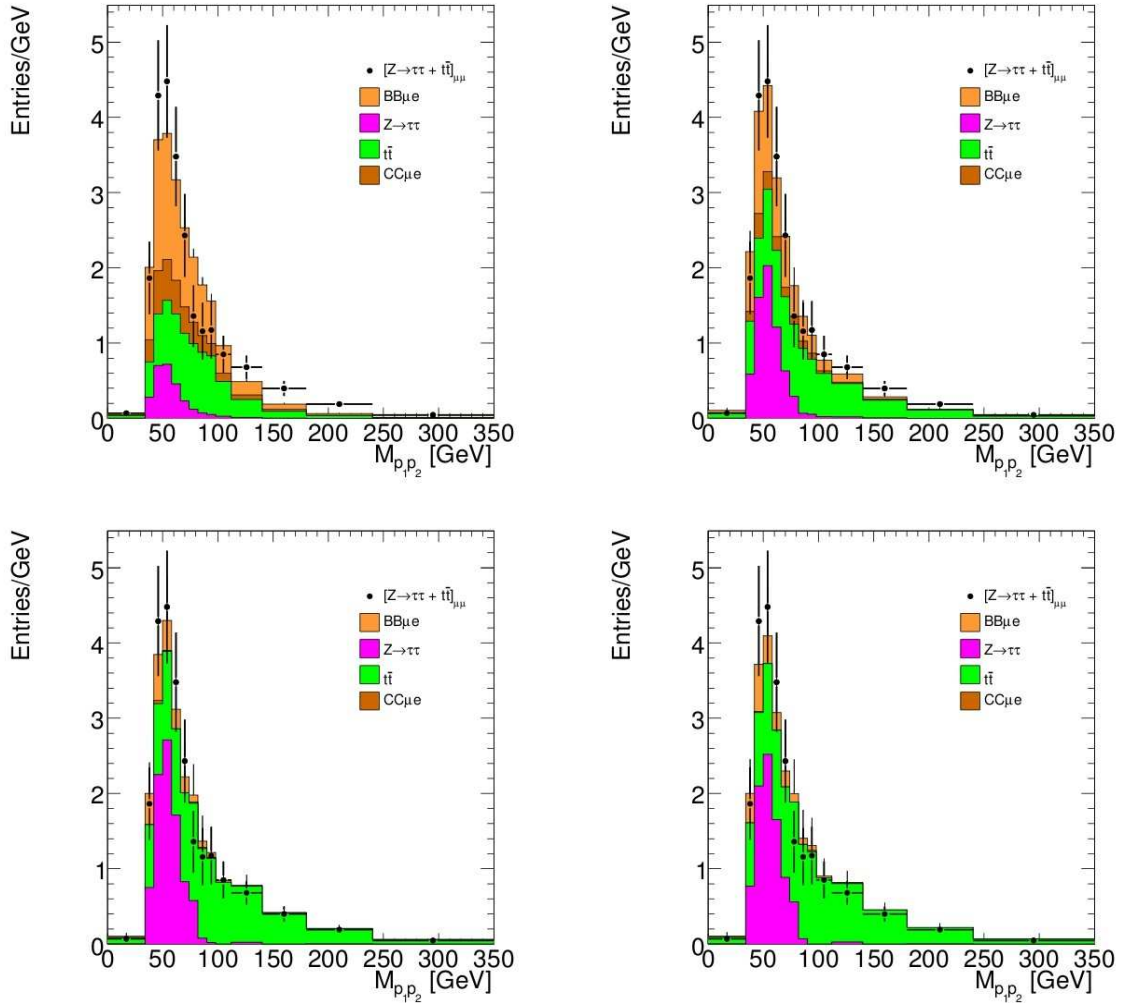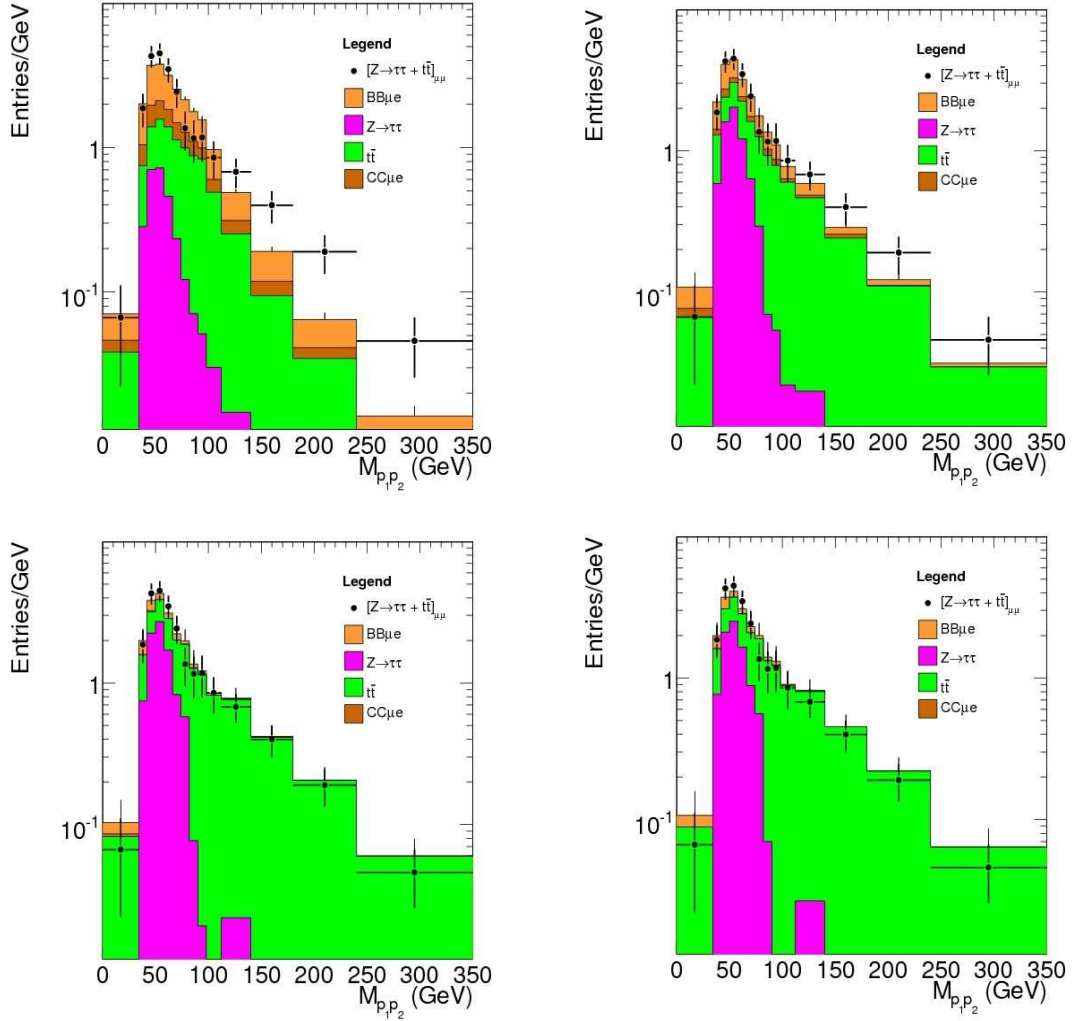**Fig. 5.9:** Comparison of invariant mass distribution of the selected µe events (stack plot) with the expected distribution for dimuons form *Z→ττ* and $t\bar{t}$ samples. The distributions are normalized to the number of dimuon events. The comparison is shown for different electron selections: all the candidate electrons (top left); *Loose* electrons (top right); *Medium* electrons (bottom left); *Tight* electrons (bottom right).

Fig. 5.10: Comparison of invariant mass distribution of the selected μe events (stack plot) with the expected distribution for dimuons form $Z\rightarrow\tau\tau$ and $t\bar{t}$ samples, in logaritmic scale. The distributions are normalized to the number of dimuon events. The comparison is shown for different electron selections: all the candidate electrons (top left); *Loose* electrons (top right); *Medium* electrons (bottom left); *Tight* electrons (bottom right).

(bottom left); Tight electron (bottom right). We see how the agreement between the dimuon and µe distribution improves as the amount of $b\bar{b}$ and $c\bar{c}$ events is reduced by tightening the electron identification. The same comparison is shown Figure 5.10 in logarithmic scale. In spite of a final 10% contamination from $b\bar{b}$ and $c\bar{c}$ events, the agreement between the shapes is rather good, at least with the statistics corresponding to about 50 pb^{-1}. The chosen tight isolation cut excludes the $c\bar{c}$ and $b\bar{b}$ contribution, while the shape of the Z➙ττ and $t\bar{t}$ contribution is more or less left invariant. An attempt to use the previously looser isolation criteria was done: it is requested $\sum p_T^{ID}/p_T < 1.4$ for the muon in the µe events and both the muons in the dimuon events. This increases the $c\bar{c}$ and $b\bar{b}$ contribution. In the Figure 5.11 I show the comparison between the µ*e* invariant mass distribution and the expected dimuon distribution from $Z \rightarrow \tau\tau, t\bar{t}, b\bar{b}$ and $c\bar{c}$ (i.e. all the dominant background components) with this looser isolation requirements. The shape of the µe distribution is clearly different from the dimuon one, as the $b\bar{b}$ and $c\bar{c}$ contributions are underestimated. This is caused by the identification cuts that reject the less isolated electrons, thus reducing the $b\bar{b}$ and $c\bar{c}$ contributions. This is compatible with the lower efficiencies of the identification cuts for $b\bar{b}$ and $c\bar{c}$ electrons[41].

I tried to use the shape of the muon-electron distribution in the likelihood fit to determinate the Z➙ττ and $t\bar{t}$ contribution using the same pseudo-data sample of the previous section. To increase the statistic and keep a good shape the *loose* electrons identification was chosen. The results are good: as seen from Table 5.9 and Figure 5.12, the results are compatible with the MonteCarlo one. The χ^2 is about 57 with 59 degrees of freedom.

5.2.5 Background Measurement Stability for Different Selection Cuts

As already stated, the selection cuts used were not fixed a priori, but several values of muon p_T and isolation cuts were used to check the measurement stability. Loosening the selection cuts we increase the background contamination, that may affect our signal counting: this is particularly true if we consider that in many cases we extract the background shapes directly from our pseudo-data sample.

We consider here a scan on the following values of the selection cuts:

$$p_T \text{ (GeV/c)} \in \{15, 17.5, 20, 22.5, 25\}$$
$$\Sigma p_{ID}/p_T \in \{0.2, 0.6, 1, 1.4, 1.8\}$$

In Figure 5.13 the result of the scan for the *Z* event counting is show for the method described in section 5.2.1, where the QCD background shape is

extracted from the pseudo-data sample itself. On the bottom-left picture, the residuals of the number of signal events as a function of the p_T cut applied and for the different isolation cuts are shown, where the residual are defined as the difference between the events obtained from fit and "true" events, divided by the uncertainty on the number of fitted events. On the bottom-right panel, the corresponding value of the fit normalized-χ^2 is shown. In the top panels, the invariant mass distributions of the pseudo-data samples together with the MonteCarlo signal and background components, normalized to the fit fractions, are shown: on the left for the loosest cut; on the right for the tightest one. The fit number of signal events are always within one standard deviation from the true value. The highest discrepancy is observed when both the isolation and p_T cuts are loosened.
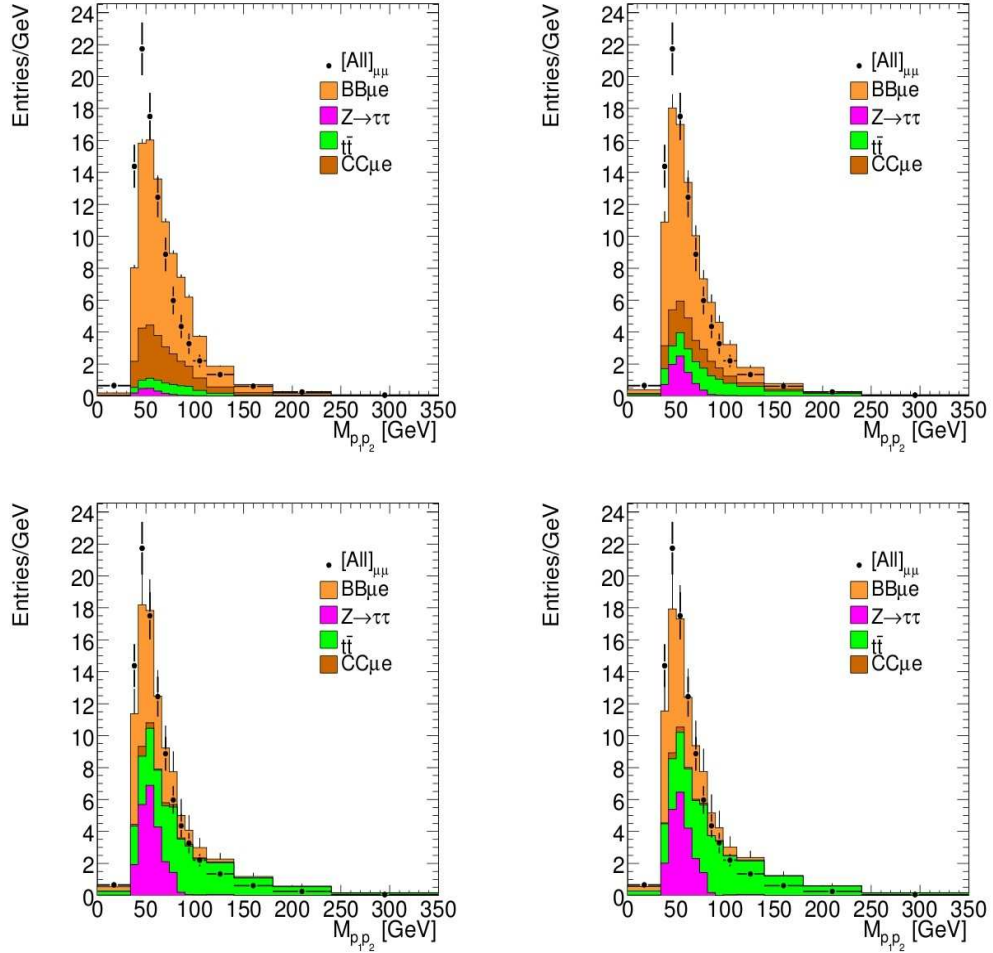
Fig. 5.11: Comparison of invariant mass distribution of the selected μe events (stack plot) with the expected distribution for dimuons for the same samples. It is requested $\sum p_T^{ID}/p_T < 1.4$ for the muon in the μ-*e* events and both the muons in the dimuon events. The distributions are normalized to the number of dimuon events. The comparison is shown for different electron selections: all the candidate electrons (top left); *Loose* electrons (top right); *Medium* electrons (bottom left); *Tight* electrons (bottom right).
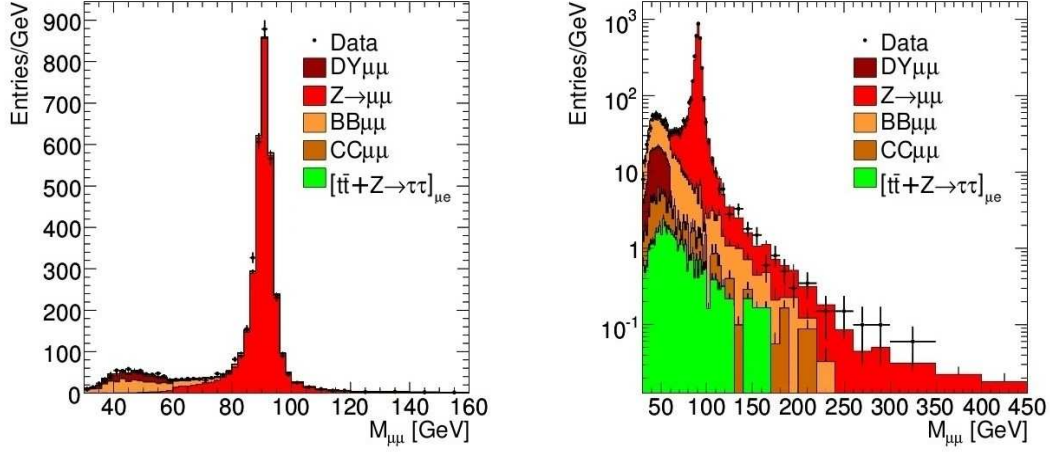
Fig. 5.12: Fit performed on pseudo-data sample using the $t\bar{t}$ + Z→ττ shape of the invariant mass distribution obtained from the muon-electron events.

Channel	Fit Fraction (%)
Z→µµ (M > 60 GeV)	80.5 ± 1.2
Drell-Yan µµ (M < 60 GeV)	4.09 ± 0.22
W→µν	0.108 ± 0.036
W→τν	$(6 \pm 8) \times 10^{-3}$
$b\bar{b}$	12.6 ± 0.61
$c\bar{c}$	14.5 ± 0.15
$t\bar{t}$ + *Z*→ττ	1.05 ± 0.15

Table 5.9: Result of the fit performed using the $t\bar{t}$ + *Z*→ττ shape obtained from muon-electron events. The fit have χ2 equal to 57 and 59 degrees of freedom.
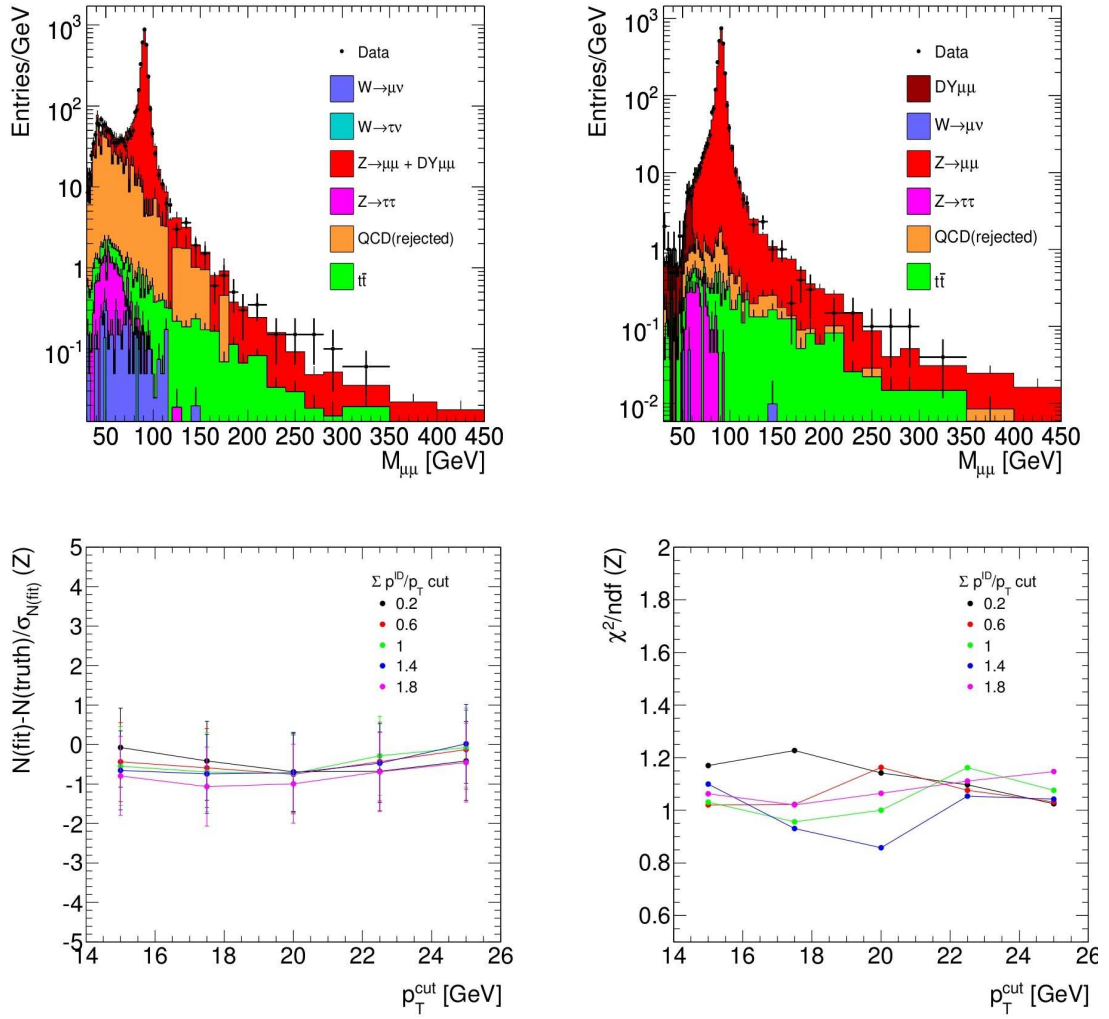
Fig. 5.13: Results of the fits to the Z lineshape for several cuts ranging from $\Sigma p_T^{ID}/p_T$ less than 1.8 and $p_T>15$ GeV/c. to $\Sigma p_T^{ID}/p_T$ less than 0.2 and $p_T>25$ GeV/c. $b\bar{b}$ and $c\bar{c}$ shape is estimated from pseudo-data events rejected by the isolation cut. Top left: fit with loosest cuts. Top Right: fit with tightest cuts. Bottom left: signal residuals. Bottom right: χ^2 per degree of freedom.

Chapter 5

Dual REAd-out Method: DREAM

The DREAM project, based on an idea proposed by R. Wigmans in 1997 started in 2002 as a generic detector R&D project intended to develop a new method, the Dual REAd-out Method, to improve the hadronic calorimeters resolution.

The prototype detector was built at Texas Tech University and then was shipped to CERN to be tested at the SPS. With the US researchers an Italian collaboration (Cosenza, Pavia, Pisa, Roma1) is involved, from 2006 in the project. As a member of the Cosenza group I participate to data taking and data analysis from 2007, while, relatively to 2006 test beam, I was only involved in data analysis.

This chapter is organized as follow. In Section 6.1 is shortly described the principles and the advantages of the Dual Readout technique for hadronic calorimeters. The most important results obtained applying the method to the fiber module prototype, are summarized.

Section 6.2 is relative to the extension of the Dual-REAdout Method to homogeneous materials (crystals) and some of the analysis that I developed during my PhD thesis are reported.

6.1 The DREAM Approach

5.1.1 A New Approach to Hadronic Calorimetry

The energy resolution of a hadron calorimeter is in general much worse than what can be achieved for electromagnetic (*em)* shower detection. The wide variety of possible interaction processes and the effects associated with excitation of the absorber nuclei are considered responsible for this. In showers created by hadron particles we can individuate an *em* component that is due, principally, to π^o decay and a *non-em* component that is populated mostly by spallation protons, neutrons and charged pions produced in nuclear reactions.

Typically calorimeters give a larger signal per unit deposited energy for the *em* shower component (e) that for the *not-em* component (h): e/h >1.

Event by event there are large fluctuations in the energy sharing between the two components of the deposited energy and the fraction of the deposited *em* energy, f_{em}, is unpredictable. As a consequence, in non compensated calorimeters, the f_{em} fluctuations are the dominant source of the poor resolution in the calorimeter response**:** $R = [f_{em} + (1 - f_{em})h/e]$.

These fluctuations, and their energy-dependent characteristics, are also responsible for other undesirable calorimeter characteristics, in particular hadronic signal non-linearity and a non-Gaussian response function.

Two different approaches are possible to eliminate the effect of these fluctuations[48][49]: by designing the calorimeter such that the response to *em* and *non-em* energy deposit is the same (compensation, e/h = 1.0), or by measuring f_{em} event by event. The DREAM project follows the latter approach.

Therefore, calorimeters built according to the DREAM principles are not subject to the limitations imposed by the requirements for compensating calorimetry: a small sampling fraction (and the corresponding large sampling fluctuations), and the need to integrate the signals over a very large detector volume (because of the crucial signal contributions of soft neutrons).

6.1.2 Dual Read Out Fiber Module

Dream calorimeters are based on a simultaneous measurement of two different types of signals which provided complementary information about the details of shower developed. The prototype (Figure 6.1, Figure 6.2) is based on a copper absorber structure equipped whit two different active media: scintillating plastic fibers and undoped quartz fibers. The first ones measure the total deposited energy while clear fibers measure the Čerenkov light generated in the shower development.

The basic element of the hadronic DREAM calorimeter section was an extruded copper rod, 2 meters long and 4×4 mm^2 in cross section. The rod was hollow, and the central cylinder had a diameter of 2.5 mm. Seven optical

fibers were inserted in this hole: three were plastic scintillating fibers, the other four fibers were undoped, intended to detect Čerenkov light. The instrumented volume had a length of 2.0 m (10 interaction lengths, 100 radiation lengths), an effective radius of 16.2 cm and a mass of 1030 kg. The fibers were grouped in 19 hexagonal towers. The effective radius of each tower was 37.1 mm (1.82 R_M). A central tower was surrounded by two hexagonal rings. The fibers sticking out at the rear end of this structure were separated in 38 bunches: 19 bunches of scintillating fibers and 19 bunches of Čerenkov fibers. Each bunch was coupled to a PMT.

Since the *not-em* component is mainly composed by not relativistic protons generated in nuclear reactions[49], the Čerenkov light is predominantly produced by the electromagnetic shower component because the $e^\pm$ through which the energy is deposited in the *em* shower component are relativistic down to kinetic energies of ~200 keV.

5.1.3 The Dual Read Out Method

The response R in a non compensated calorimeter is expressed as a function of the *em* fraction, f_{em}, and the e/h ratio by:

$$R(f_{em}) = f_{em} + \frac{1}{e/h}(1 - f_{em}) \qquad (6.1)$$

Defined in this way, R = 1 for *em* showers.

In the DREAM Module, based on 6.1, that holds separately for both sampling media, the two signals Q (Čerenkov signal) and S (scintillation signal) are respectively:

$$Q = [f_{em} + \frac{1}{(e/h)_q}(1 - f_{em})] \, E \qquad (6.2)$$

$$S = [f_{em} + \frac{1}{(e/h)_s}(1 - f_{em})] \, E \qquad (6.3)$$

For the DREAM fiber module $(e/h)_q \sim 5$, $(e/h)_s \sim 1.4$ [50]

So the signals ratio is expressed by:

$$\frac{Q}{S} = \frac{[f_{em} + 0.21(1 - f_{em})]}{[f_{em} + 0.77(1 - f_{em})]} \qquad (6.4)$$

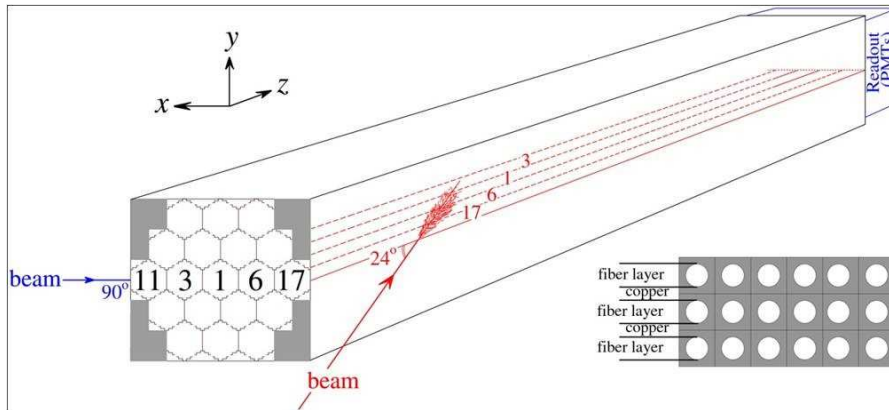where 0.21 and 0.77 represent the h/e ratios.
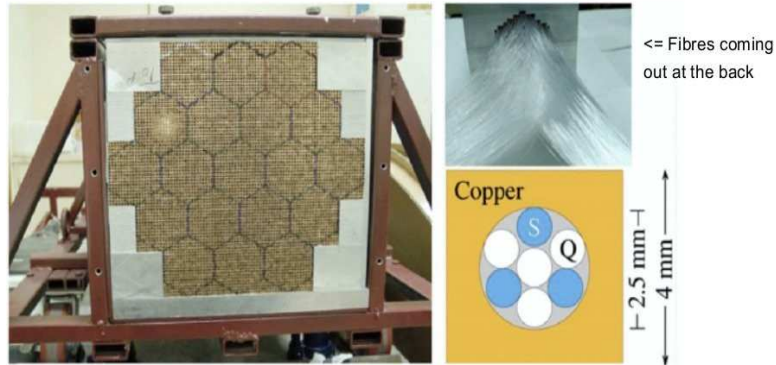
Fig. 6.1: DREAM calorimeter sketch.

Fig. 6.2: The hexagonal tower structure of the DREAM hadronic fiber calorimeter (a). An example of the separation of fibers in different bunches (b). The structure of the basic element of the calorimeter (the seven fibers and the copper rod) (c).

Equation 6.4 provides a simple and energy- independent relationship between the measured signals ratio and the electromagnetic fraction that can be determined for each event.

In Figure 6.3 is reported the Čerenkov signal distribution for 100 GeV π^- (a) and the distribution for subsamples selected for different f_{em} ranges are reported in (b). The average value increases with the electromagnetic fraction. The total signal distribution is the sum of many Gaussian distributions, each characterized by a certain range of f_{em} values. Once the value of f_{em} is determined the signals can be corrected in a straightforward way for the effects of non-compensation and the total shower energy can be reconstructed using the known e/h value of the calorimeter:

$$E = \frac{S - \chi Q}{1 - \chi} \qquad (6.5)$$
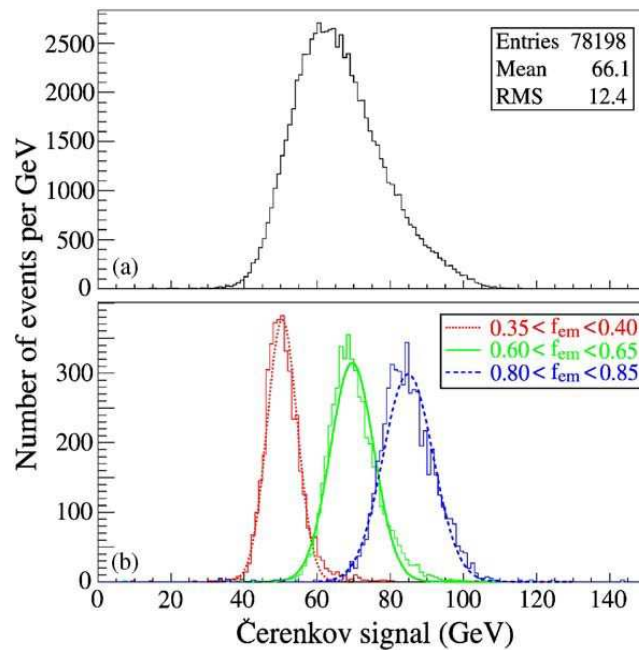
Fig. 6.3: Čerenkov signal distributions for 100 GeV multi-particle events. Shown are the raw data (a), and the signal distributions for subsamples selected for different f_{em} ranges (b).
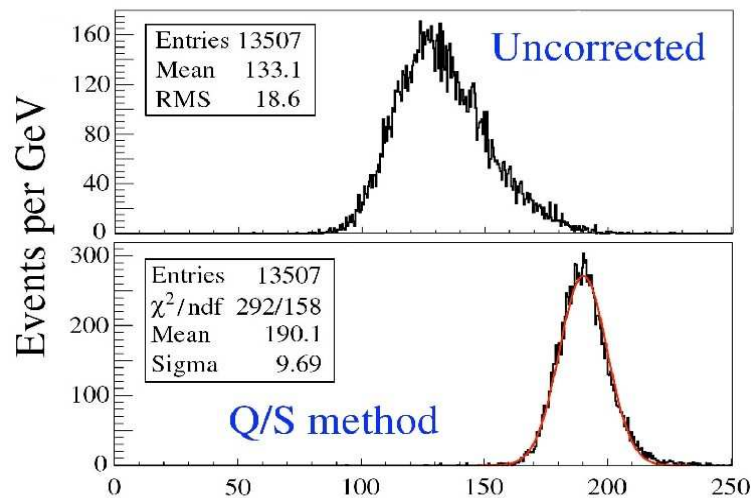

Fig. 6.4: Čerenkov signal distributions for 200 GeV multi-particle events. Shown are the raw data (a), and the signal distributions obtained after application of the corrections based on the measured *em* shower content (b).

where

$$\chi = \frac{1 - (h/e)_S}{1 - (h/e)_Q} \qquad\qquad (6.6)$$

is the "calorimetric constant".

  To show how the Q/S method work in energy reconstruction, in Figure 6.4 is reported the Čerenkov signal distribution before and after the application of the corrections. The raw Čerenkov signal distribution is plotted in Figure 6.4(a). The distribution is asymmetric, broad and the central value is much too small (133 GeV). After applying the correction method based on event-by-event measurements of f_{em}, this distribution is transformed into the one shown in Figure 6.4(b), which is almost perfectly symmetric, much more narrow, and centered around 190 GeV. Because of the relatively small detector size the obtained result is dominated by fluctuations in (lateral) leakage

5.1.4 Advantages of the Dual Readout Method

The overall results obtained applying the Dual readout method can be summarized as follow:

- Non linearity in the response due to the fact that $<f_{em}>$ increases with energy is eliminated.
- The hadronic shower energy is correctly reconstructed, based on electron calibration.
- The signal distribution becomes much more Gaussian in shape.
- Energy resolution scales as $1/\sqrt{E}$.

Once the effects of the dominant source of fluctuations, i.e fluctuations in the *em* energy fraction, are eliminated, the performance characteristics are determined (and limited) by other types of fluctuations.

  In the described detector these fluctuations include, apart from fluctuations on side leakage which can be eliminated by making the detector larger, *sampling fluctuations* and *fluctuations in the Čerenkov light yield* due to the small number of Čerenkov photoelectrons constituting the signals (8 p.e./GeV). As described in Section 6.2, these effects may be effectively reduced by using a homogeneous calorimeter that produces a separable mixture of scintillation and Čerenkov light.

  Once the mentioned effects have been eliminated, the performance of this type of detector may approach the theoretical hadronic energy resolution limit. This limit is correlated to invisible energy, which results from the fact that some (variable) fraction of the energy carried by the showering particle is

used to provide the nuclear binding energy needed to release nucleons and nucleon aggregates in nuclear reactions. It has been shown that efficient detection of the neutrons abundantly produced in these processes may be an effective tool for reducing the effect of these fluctuations and that hadronic energy resolutions of 15-20%/$\sqrt{E}$ might be achieved this way[48].

The measure of the neutron contribution to the hadron signals has been obtained[51][52] by analyzing the time structure. The relative contribution of soft neutrons to these signals is derived from the characteristic exponential tail in the time structure of the scintillation signals.

6.2 The Dual Read Out Method with Crystals

In these past years the possibility to apply the DREAM principle not only to a sampling calorimeter but also to an homogeneous (fully sensitive) calorimeter, provided that the light signals can be separated into scintillation and Čerenkov components, has been investigated. From 2006 the DREAM collaboration, with this purpose, carried out a variety of studies involving crystal calorimeters.

If successful, this approach could eliminate at once both the effects of sampling fluctuations and the effects of fluctuations in the Čerenkov light yield to the hadronic energy resolution.

The improvement of the calorimeter performance is, in that case, determined by the precision with which the relative contributions to the total signal of these two types of light can be determined.

An interesting scenario, in terms of resolution, is a composite system where in front to a DREAM-like calorimeter is placed a dual readout high resolution electromagnetic calorimeter in order to measure event by event the electromagnetic fraction in hadronic showers and therefore to correct the energy measurement. In general calorimeter systems have a separate *em* section, optimized for electron and photon detection. Such a section is typically ~1 λ_{int} deep and it absorbs half of the energy carried by jets. Application of the dual-readout principles in such a segmented calorimeter system would only make sense if one could also detect both *dE*/*dx* and Čerenkov signals from the *em* calorimeter section. Crystals producing a mixture of scintillation and Čerenkov light would provide that option.

5.2.1 Analysis Method in Single Crystals

To distinguish the contributions from the Čerenkov and the (dominating) scintillation components to the crystal signals, we have exploited three properties:

- *Directionality*: The Čerenkov light, emitted by relativistic particles, is directional, while the scintillation light is isotropically emitted. By

reading out the detector from two opposite sides, and by varying the detector orientation, a contribution of Čerenkov light manifests itself as an angle-dependent asymmetry. We measured the signals for different orientation (i.e. angles θ) of the crystal respect to the beam. This properties, useful to evaluate the relative Čerenkov contribution, cannot be used in a realistic experiment.

- *Time structure*: The Čerenkov light is prompt, while scintillation processes in the crystals exhibit one or several time constants, which determine the pulse shape. By measuring the detailed time structure of the signals, the two components of the signal may be distinguished.

- *Spectrum*: The spectrum of the Čerenkov light exhibits a characteristic λ^{-2} shape, while the scintillation processes have their own characteristic spectra, very crystal-specific. If these two spectra are sufficiently different, they can be separated by means of optical filters.

An additional feature that potentially also might be used to distinguish the contributions of the two types of light to the calorimeter signals is the fact that Čerenkov light is polarized. We have started form July 2010 test beam to exploit this aspect. The work is going on, the obtained results up to now are interesting, and we submitted them for publishing.

Based on the above criteria, some qualitative indications can be given for the choice of the crystals. First, the use of a "slow" scintillator would be preferred, to allow the separation of the prompt (Čerenkov) and the delayed (scintillation) component from the signal waveform. The prompt signal timing will usually be dominated by the photodetector response function, so one would take advantage of a scintillator with a decay time much larger than this value, time constants of the order of $20 \div 50$ ns (or longer) would be preferred. Two considerations can then be made to take advantage of the different light spectra. Čerenkov radiation is distributed as λ^{-2}, however it is in general difficult in a standard setup to collect light below 300 nm. For this reason one would like to have a scintillator emitting mainly above 400 nm, in order to dedicate the interval $300 \div 400$ nm of photodetector sensitivity to the Čerenkov light. In this situation the use of colored filters in front of the photo-multipliers will allow an efficient separation of the two light components. It should also be noted that the transmittance of the crystal below the scintillation emission peak should be guaranteed for this method to work, otherwise no separation could be achieved based on the light wavelength. This is not easy to obtain in doped crystals, where usually the emission spectrum is partially overlapping the absorption spectrum. Some natural scintillating crystals however have this property. Finally, it should be noted that the scintillation and Čerenkov signals

should be comparable at the photodetector, since the corrected calorimeter energy resolution, calculated using both signals, will be dominated by the statistical fluctuations of the smaller signal component.

5.2.2 Experimental Setup

All the measurements were performed in H4 beam line of the SPS at CERN. In the Figure 6.5 right it is shown the principle on which are based our measures: depending on the orientation, the directionally emitted Čerenkov light contributes differently to the signal. The crystal was mounted (Figure 6.5, left) on a platform that could rotate around a vertical axis. The crystal was oriented in the horizontal plane and the rotation axis went through its geometrical center. The particle beam was also steered through this center.

The angle θ represents the angle between the crystal axis and a plane perpendicular to the beam line. The angle increases when the crystal is rotated such that the crystal axis (L-R) approaches the direction of the traveling beam particles.

The light produced by particles in the crystal was acquired by two PMTs: the Left PMT and the Right PMT (indicated as L and R in Figure 6.5).

Two small scintillation counters provided the signals that were used to trigger the data acquisition system. These Trigger Counters (TC) were 2.5 mm thick, and the area of overlap was 6×6 cm^2. A coincidence between the logic signals from these counters provided the trigger.

To reconstruct the trajectories of particles two small drift chambers (DC1, DC2) were installed upstream of the trigger counters.

The platform is located upstream the DREAM calorimeter. A muon counter is provided by a 50x50 cm^2 scintillator paddle. It is placed about 10 m downstream of the crystal, behind about 20 interaction lengths of concrete blocks.
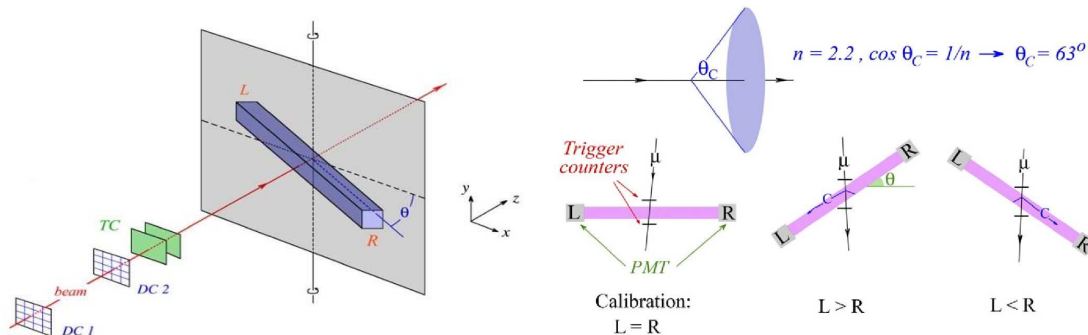

Fig. 6.5: *Left: e*xperimental setup in which the beam tests of the crystals were performed. *Right:* principle of the asymmetry measurement used to establish the contribution of Čerenkov light to the signals from the crystals.
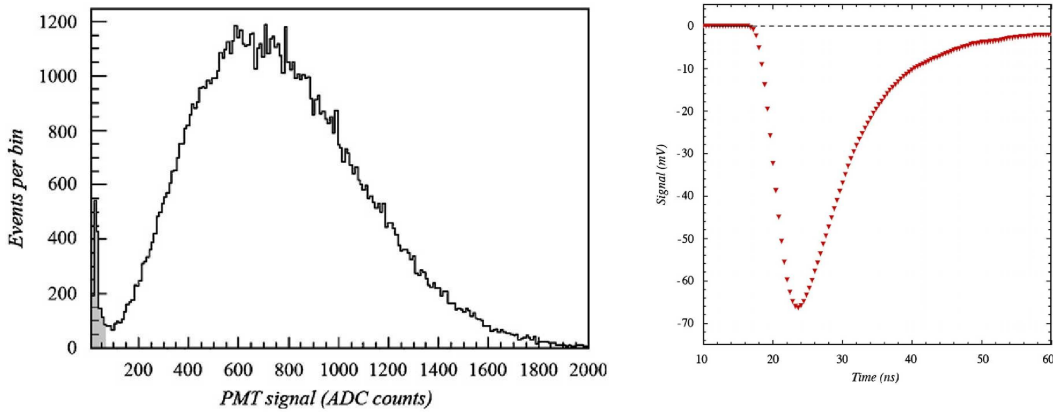
Fig. 6.6: The signal of a beam of 50 GeV electrons traversing the PbWO$_4$ crystal is read from both sides of the crystal with an ADC counter and an oscilloscope. Fig. a (left) shows the ADC spectrum, that is proportional to the mean energy released by particles traversing the crystal, and Fig. b (right) shows the average time structure of the signals.

       The crystal signals were sent into a unity-gain Linear Fan-out unit, output signals of which were used to measure the time structure and the total charge. The charge measurements were performed with 12-bit Lecroy 1182 ADCs. These had a sensitivity of 100 fC/count and a conversion time of 5.7 μs.

       In 2006 the signals were split into five equal parts. One was sent to the ADC for the charge measurement, four were used for the time-structure analysis by the means of a FADC, that measured the amplitude of the signals at the rate of 200 MHz. The four signal were measured in 4 different channels. Signal 2, 3 and 4 were delayed of 1.25 ns, 2.50 ns and 3.75 ns with respect to the signal 1; in this way the time structure was measured with a resolution of 1.25 ns.

       In 2007, 2008 and 2009 to obtain the time structure we employed a Tektronik TDS 7254B digital oscilloscope, with sampling capacity of 5 GSample/s, at an analog bandwidth of 2.5 GHz, over four input channels (only two channels were samples, from the two PMTs reading out both sides of the crystal).

       As example in Figure 6.6 an typical ADC signal distribution and the average time structure of the signals from one PMT are shown, both signals generated by 50 GeV electrons traversing a PbWO$_4$ crystal.

       A monitoring program produces online histograms to control the data quality during acquisition.

5.2.3 Single Crystals

Directionality

The crystal to be tested was a Lead Tungstate (**PbWO$_4$**) crystal with a length of 18 cm and a cross section of 2.2x2.2 cm^2. The transverse dimension corresponded to ~2.5 radiation lengths[53]. These crystals are used in several modern experiments as detectors for electromagnetic showers because of their short radiation length and Moliere radius, their fast signals and their relative insensitivity to the effects of radiation damage.

In these crystals a significant fraction of light production is due to Čerenkov radiation.

The experimental setup is shown in Figure 6.5 left. The crystal was posed in a 10 GeV electron beam. Any Čerenkov light produced by the showering particles would be emitted at a characteristic angle of ~63° with the beam direction. Detection of this light would thus depend on the crystal orientation, i.e. on the angle θ. On the other hand, detection of the isotropically emitted scintillation light would be independent of θ.

We define the *asymmetry* ξ as

$$\xi = \frac{(R-L)}{(R+L)} \qquad (6.7)$$

where *R* and *L* represent the average value of the signal measured by PMT R and L at the same angle θ of the crystal respect to the beam line, and:
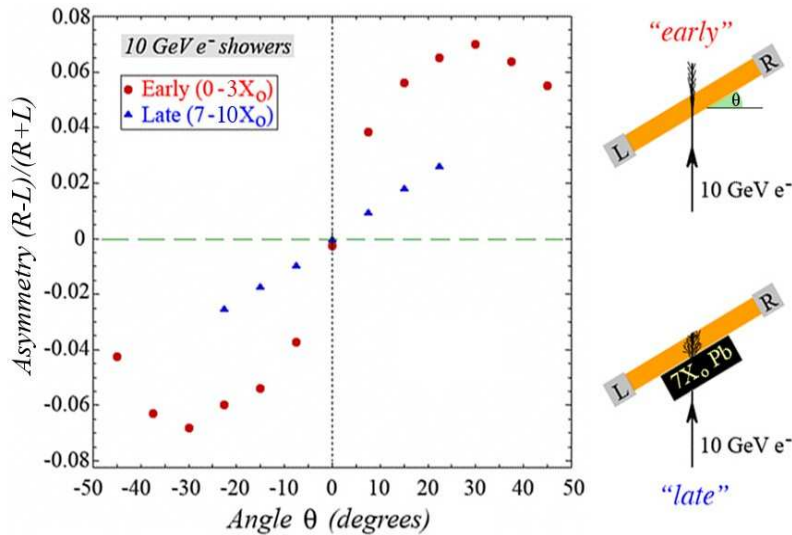

Fig. 6.7: Left-right response asymmetry as a function of the orientation of the crystal.

$$R = C_R + S \qquad L = C_L + S \qquad (6.8)$$

with C_R and C_L the Čerenkov component of the two signal and S the scintillation one.

In Figure 6.7 the obtained asymmetry ξ as function of the angle θ is reported. From 6.7 and 6.8 we can express ξ as:

$$\xi = \frac{\epsilon_R - \epsilon_L}{2 + \epsilon_R + \epsilon_L} \qquad (6.9)$$

where ϵ_R and ϵ_R are the Čerenkov contributions C_R and C_L normalized to the scintillator signals.

When the asymmetry reaches its maximum value, $\epsilon_L = 0$ and $\xi = \epsilon_R /(\epsilon_L+2)$. The relative contribution of the Čerenkov light to the total R signal can be than expressed as

$$f_C = \frac{\epsilon_R}{1 + \epsilon_R} = \frac{2\xi}{1 + \xi} \qquad (6.10)$$

In this experiment the maximum asymmetry was 0.07 at θ = ±30°, corresponding to the characteristic Čerenkov angle of ~63°, and we can conclude that more than the 15% of the signal is due to Čerenkov light.
With the same approach we have also analyzed the asymmetry at different phases of the *em* shower development. This was obtained putting between the beam and the crystal some lead absorber with different thickness. With an absorber with a thickness of 25 mm (4.5 X_0), for example, the crystal detected light produced at a depth between 4.5 and 7X_0, i.e. around the shower maximum. In this case the anisotropy decreases because the particles of the shower are no longer mips that go in the same direction; the Čerenkov light is then emitted more isotropically respect to the detector (Figure 6.7). The same measures were taken again using a different acquisition system[54] with improved time resolution to study the possibility to improve the precision of the measurement of the Čerenkov component based on the time structure signal.

In a different data taking[55], after that the crystal was bring to thermic equilibrium, similar measures were executed changing the temperature in a range between 13°C and 45°C. We could so evaluate the expected dependence of the scintillation properties of the crystals from the temperature[56] (Figure 6.8), and the independence of the Čerenkov light from it (Figure 6.9).
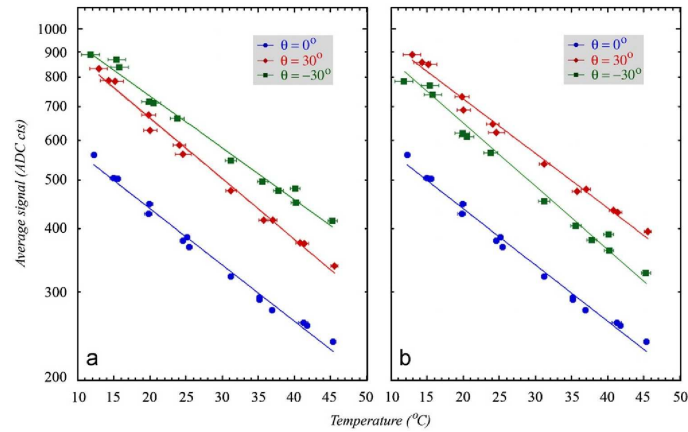
Fig. 6.8: Signals from the PbWO$_4$ crystal as a function of the temperature, measured with PMT L (a) and PMT R (b), for 50 GeV electrons traversing the crystal at angles θ=30°, 0° and -30°. The error bars report the statistical errors.
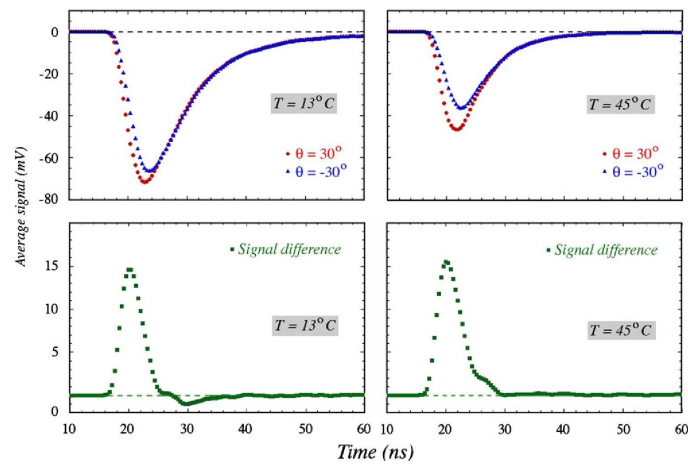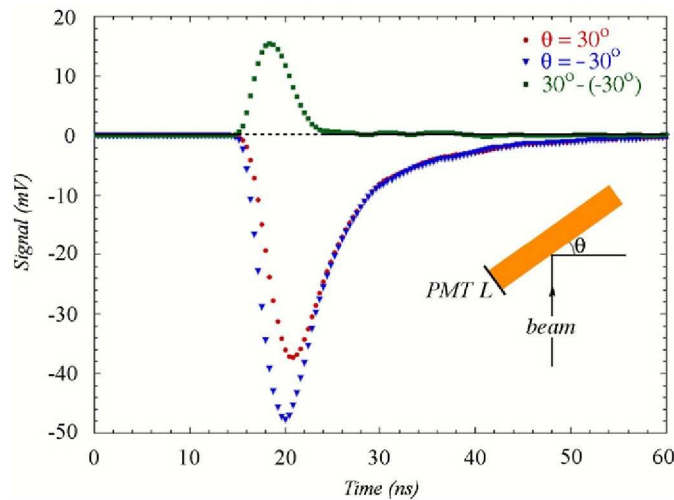

Fig. 6.9: Average time structure of the signals from PMT R measured for 50 GeV electrons traversing the PbWO$_4$ crystal at θ = 30° and θ = -30°(top plots), as well as the difference between these two signals (bottom plots), measured for two different temperatures: 13°C (left) and 45°C (right)

Time structure and spectrum

A calorimeter based on the dual readout method requires a precise measurement of the ratio Q/S event by event. To obtain this the two signals have to be well separated and the value of the ratio Q/S is required to be high enough.

We have investigated different kinds of crystals to evaluate the signals separability, that is based on the time structure and the spectrum. A separation in time structure implies a scintillation decay time long enough to recognize the scintillation component from the shape of the signal. A wavelength difference allow us to use filters to enhance the Čerenkov component.

Fig. 6.10: Average time structure of the signals from PMT R measured for 50 GeV electrons traversing the PbWO$_4$ crystal at θ = 30° and θ = -30° (red and blue), as well as the difference between these two signals (green)

The first analysis of time structure of signals was made for a single PbWO$_4$ crystal. A check on the dependence of the average time structure from the angle of the incident beam was done. In Figure 6.10 a comparison between the oscilloscope signal for PMT L at θ = -30° (Čerenkov maximum) and θ = 30° (no Čerenkov) is shown: as can be seen, the contribution of Čerenkov light in the signal at -30° causes the leading edge to be steeper and the amplitude to be larger. This properties of the time structure was been exploited to estimate the fraction of Čerenkov light produced event by event. Three methods were employed: measuring the time at which the impulse exceed a preset threshold value, measuring the steepness of the leading edge by parametrizing it, or measuring the fraction of total charge collected in a given time interval (e.g.: the first 5 ns)[53],[54]. Overall, the light produced in the PbWO$_4$ crystal has a considerable fraction of Čerenkov component. However, as seen from the
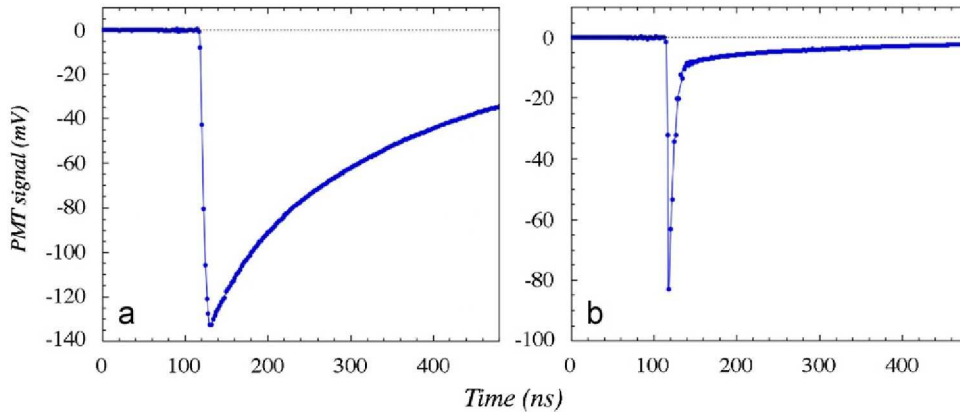
Fig. 6.11: The time structure of a typical shower signal measured in the BGO crystal equipped with a Yellow filter (a) and a UV filter (b).

average time structure, the separability of the two components required in an event by event analysis is not so good even in the situation of the greatest difference in the Čerenkov light production.

Searching for a crystal with better characteristics, in later data taking signals of a **BGO** ($Bi_4Ge_3O_{12}$) crystal were analyzed[57]. Even though Čerenkov radiation represents a much smaller fraction of the light produced by these crystals, BGO scintillation light has a high wavelength. This fact was exploited using two different filters on the two sides of the crystal which select the two light components: one (Yellow) selects mostly the scintillation component, while the other (UV) enhances the Čerenkov component reducing the scintillation light. In Figure 6.11 the time structures of the signals for the two filters are shown. In particular, the Figure 6.11b (signal with UV filter) shows the prompt peak of the Čerenkov light and a long tail which is the residual fraction of scintillation light. This shape for the UV side can be used to obtain all the information needed from only one signal (Figure 6.12a). A narrow gate centered on the Čerenkov peak is chosen to select mostly the Čerenkov light, while a longer second one selects the tail, allowing us to see only scintillation light. This method permits also to estimate the fraction of scintillation light in the first gate. In Figure 6.12b the fraction of scintillation and Čerenkov light at the first time gate for different lengths of the gate is shown.

In Figure 6.13 I report the shape of the scintillation and Čerenkov light as function of the angle for 50 GeV electrons (left), and the corresponding C/S ratio, that is a measure of the dependence of the Čerenkov component from the angle (right). As expected, the Čerenkov component is peaked on the Čerenkov angle. The angular distribution shows variations outside statistic in the range from 20°-35°. This has been attributed to some systematic effects as shape of the crystal (as it will be descibed later) and light collection mechanism.
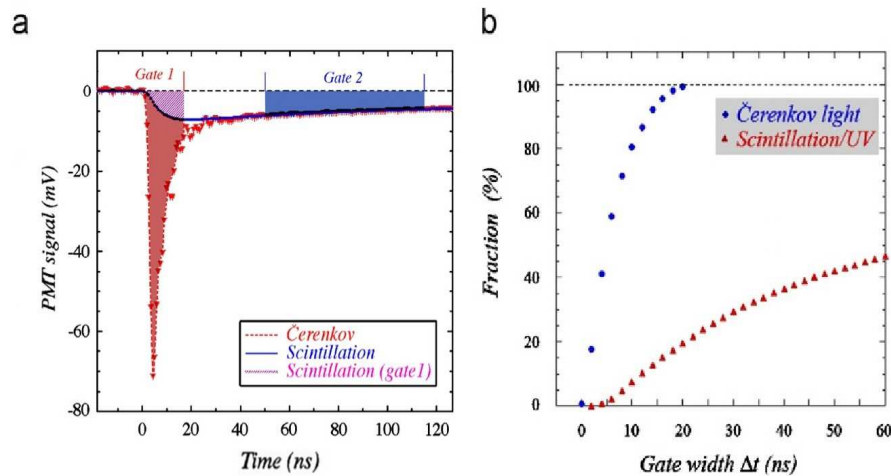
Fig. 6.12: *a)* The average time structure of the UV BGO signals, with the two gates used to measure the relative contributions of scintillation light (gate 2) and Čerenkov light (gate 1). *b)* The average fraction of the total UV signal that was caused by scintillation light, as well as the average fraction of the Čerenkov light collected as a function of the gate width.

The BGO has better properties than the $PbWO_4$ (higher scintillation spectrum, longer decay time) but the fraction of Čerenkov light in its signals is too much low to permit the use in a real calorimeter because of the fluctuations in the collected photoelectrons. Because of this results, several $PbWO_4$ crystals, each with different kinds and levels of doping (Mo, Pr), have been produced and tested[58]. This impurities increased the decay time of the $PbWO_4$ and the wavelength of the scintillation light emitted.

For the crystal doped with praseodymium, a huge prompt peak is shown, even with Yellow filters; the scintillation light is dominated by very slow components and its signal is stretched in an extremely long tail.

The crystal doped with molybdenum show a good distinction between Čerenkov and scintillation: using a UV filter Čerenkov light almost pure can be seen (as seen in Figure 6.14).

Increasing the concentration greatly decrease the Čerenkov component. This a symptom of auto-absorption of Čerenkov light form the molybdenum impurities, and it is a negative characteristic for us (for example, to increase the absorption implies to increase the dependence of the signal from the impact point of the beam). This effect can be mitigate using a filter with a broader bandwidth for the Čerenkov light filter[59].

We can so conclude that:
- pure PbWO4 crystals have the advantage that Čerenkov light represents an high fraction of the total, but they have not a not good separation of Čerenkov and scintillation components;
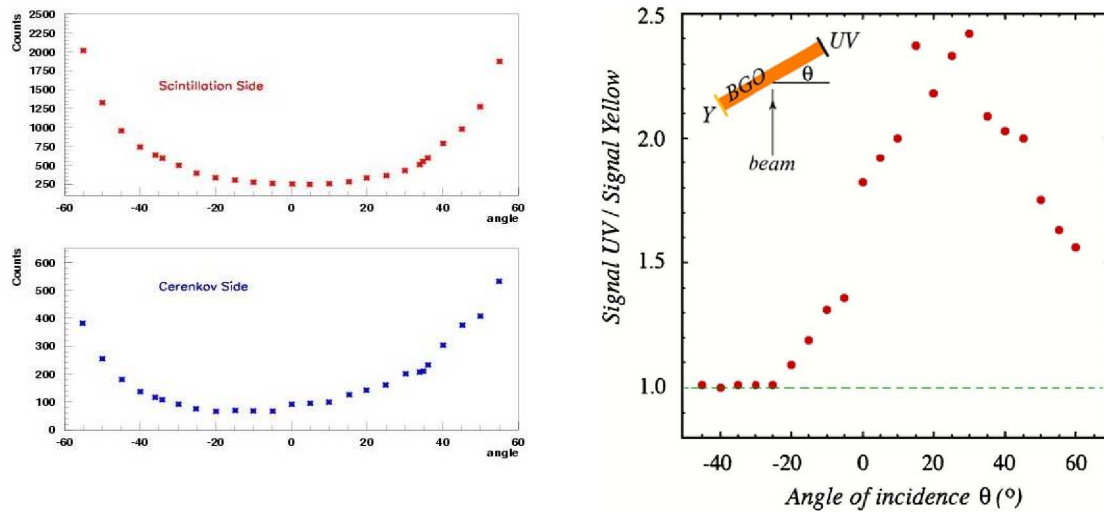
Fig. 6.13: *Left:* Čerenkov and scintillation signals in a BGO crystal for 50 GeV e^-, as function of the orientation of the crystal with respect to the beam. *Right:* the Čerenkov/scintillation ratio as a a function of the orientation.
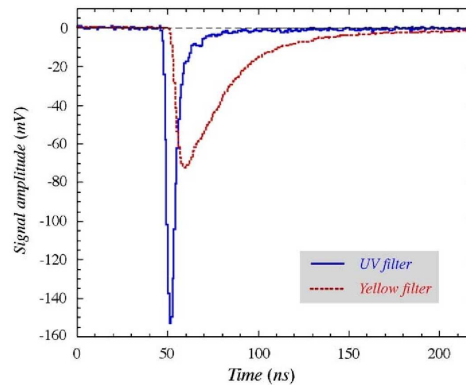

Fig. 6.14: Average time structure forma a PbWO$_4$ crystal doped with 1% Mo, generated by 50 GeV e at a 30° angle.

- BGO crystals have a good separation but a low Čerenkov fraction;
- doped $PbWO_4$ crystals have a good separation and but the self-absorption of Čerenkov light is not insignificant (this is a concern for the application on real calorimeters where the shower fluctuate over distances of typically 20 cm).

In July 2010 test-beam a crystal of **BSO** ($Bi_4Si_3O_{12}$), which has the same crystal structure as BGO with the germanium atoms replaced by silicon ones, was analyzed. The obtained results are encouraging and have been submitted to be published.

5.2.4 Correlation between Electromagnetic and Hadronic Calorimeters

As previously explained, the study of the performances of an hybrid system ECAL-HCAL to improve the hadronic resolution is a goal of the collaboration. We started to test such a system employing as *em* section a single crystal or crystal matrices ($PbWO_4$, BGO)[57][60][61].

DREAM and single BGO crystal

The experimental setup used with the DREAM-BGO single crystal system is shown in Figure 6.15. All measurement were preformed with 200 GeV π^+ beams. The data acquisition employed ADCs for HCAL (the DREAM fiber calorimeter) and both ADCs and oscilloscope for ECAL (the BGO crystal). The UV Čerenkov and the scintillation signals produced by the BGO crystal, as the 38 DREAM channels, were separately calibrated with 50 GeV electrons. On the two BGO PMTs two different filters were used to better separate Čerenkov and scintillation components. The scintillation spectrum of BGO is
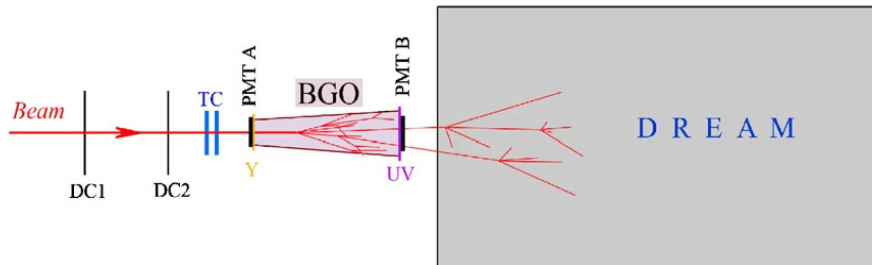

Fig. 6.15: Schematic (not in scale) experimental setup in which the BGO crystal was tested in conjunction with DREAM. A muon counter, not reported in figure, is placed 8 m downstream of DREAM behind a 80 cm thick concrete block.

centered around a wavelength of 480 nm, so the Yellow filter is highly transparent for this type of light. The UV filter is transparent for light in the wavelength region from 250 to 400 nm, which harbors a large fraction of the Čerenkov light, and little of the scintillation one. The crystal was tapered, with a front face (UV filter side) of 2.4x2.4 cm^2 and a rear face (Y filter side) of 3.2x3.2 cm^2. It is long 24 cm, so even for the *e-* showers only less than the 80% of the deposited energy is contained in the crystal. For the pions, the interaction length is about 30 cm, so ~45% of these particles traversed the crystal without undergoing a nuclear interaction (as seen in Figure 6.16). In our studies we are interested to pions that started to shower in the BGO and deposited a significant fraction of their energy in it; so we selected the events with energy deposited in the crystal in the range 20-40 GeV (Figure 6.16).

Our aim is to verify that the event-by-event determination of the Čerenkov component and thus of the electromagnetic shower fraction in the hadronic shower development is of comparable quality as that achieved for the DREAM fiber calorimeter were the two components were measured with two physically active media. For that purpose, it is useful to focus the attention on the C/S ratio. In Figure 6.17 the ratio C/S for 50 GeV electrons showering in the BGO is reported. As expected, the main value is (after calibration) very close to one.
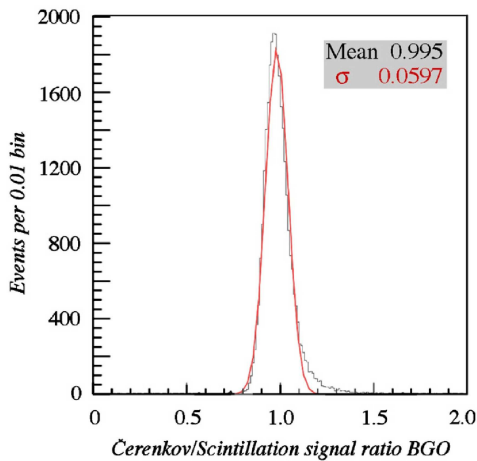

Fig. 6.16: distribution of the C/S signal ratio for 50 GeV *e*⁻ showering in the BGO crystal.
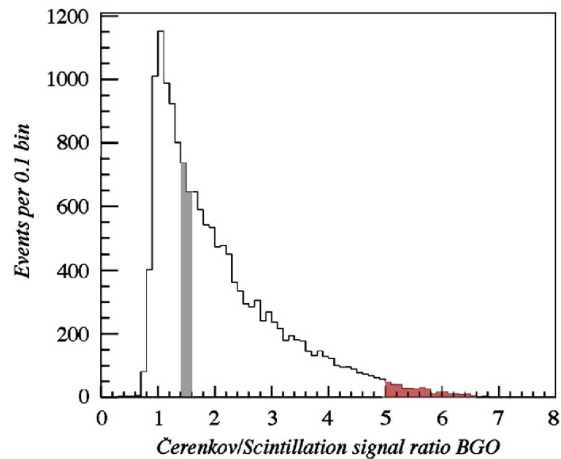
Fig. 6.17: distribution of the C/S signal ratio for 200 GeV π^+ showering in the BGO crystal, and depositing 20-40 GeV.

The cause of long tail in the C/S ratio for pions (in the Figure 6.18) was investigated. To verify the importance of attenuation effects we rotated the crystal of 90° (i. e., perpendicularly to the beam line). *e*⁻ of 50 GeV were sent
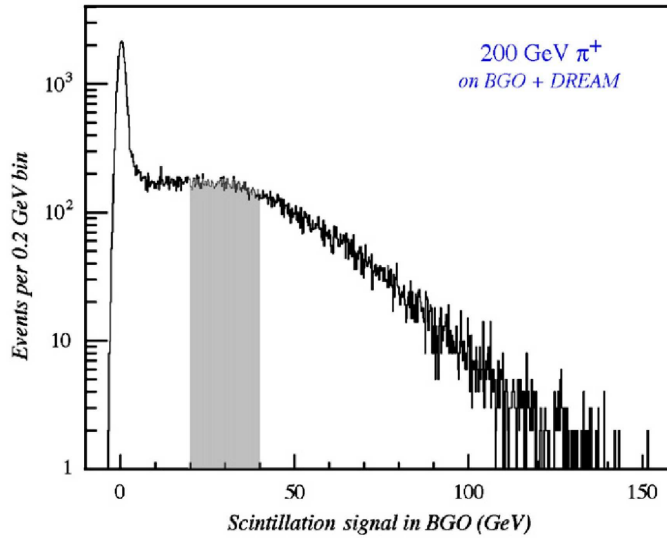
Fig. 6.18: Scintillation signal distribution in BGO crystal for 200 GeV π^+. Events in the shaded area were selected for analysis. The logarithmic scale is needed since a large fraction of the pion did not started a shower in BGO.

into the crystal, which was moved in steps of 1 cm; in this way, the responses of the two PMTs were measured over the full length. The C/S ratio does not change much over length (Figure 6.19) except for the point closest to the UV PMT. We interpret this effect as the fact that in this case some of the particles of the shower transverse the glass window of the PMT and/or the filter and generate Čerenkov light but not scintillation light in the process.

Because the BGO ECAL section of our calorimeter system was so small, it is reasonable to expect that the C/S ratios in the two sections have to be correlated (Figure 6.20). From this, as in DREAM standalone we could find a correlation between the signal and C/S, now we expect the same correlation between C/S in the BGO and the signal in DREAM (Figure 6.21).

The results in Figure 6.22 confirm, once again, that the event selection on the basis of the C/S signal ratio in the BGO crystal is a good measure of the f_{em}. In Figure 6.22 the total scintillation signal measured in HCAL for subsets of events selected on the basis of the C/S signal ratio in the BGO ECAL is shown. This figure can be compared with the Figure 6.3 for DREAM standalone. As expected, the signal distribution for the events with a large C/S value is narrower and peaked at larger values than the distribution for events with a smaller C/S ratio.
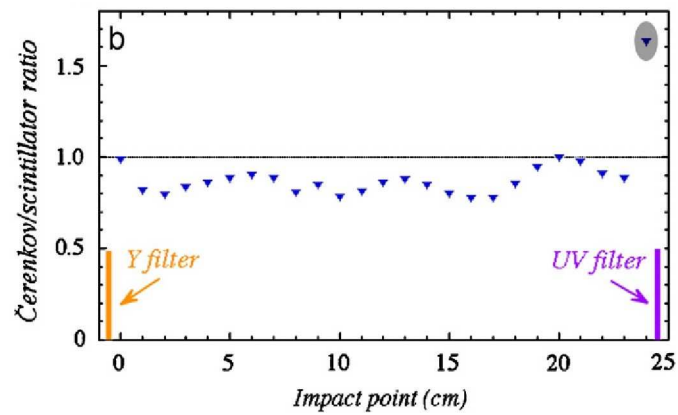
Fig. 6.19: C/S ratio as a function of the distance from the light production to the PMTs (50 GeV e^-).
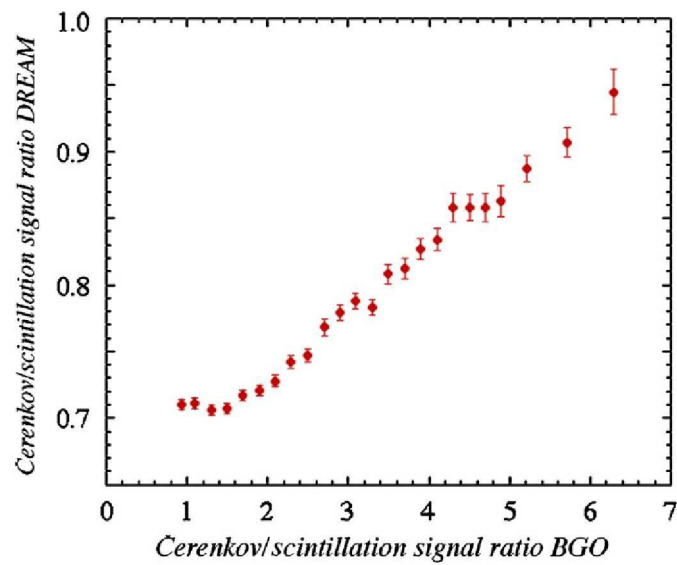

Fig. 6.20: C/S ratio in the DREAM calorimeter as a function of the C/S ratio in the BGO crystal for 200 GeV π^+ starting a shower in the crystal.
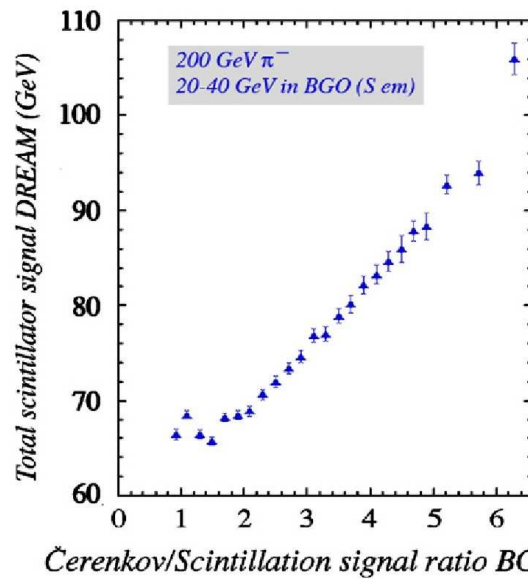
Fig. 6.21: Scintillation signal in the DREAM calorimeter as a function of the C/S ratio in the BGO crystal for 200 GeV π^+ starting a shower in the crystal.
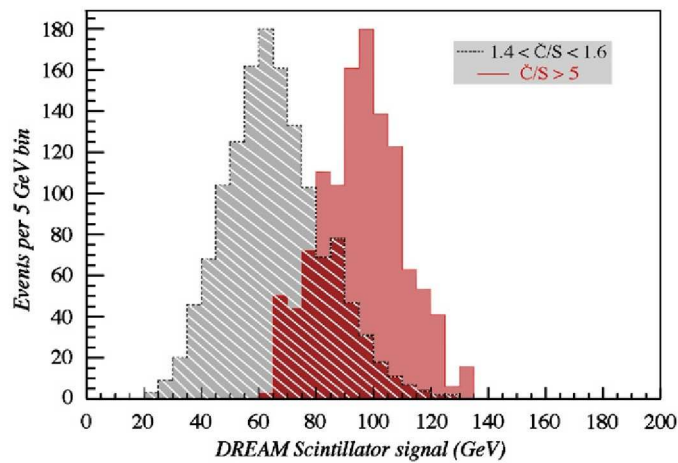

Fig. 6.22: Scintillation distribution in DREAM for a 200 GeV π^+ starting a shower in the crystal and depositing 20-40 GeV in the crystal, for two different values of the C/S ratio in BGO

DREAM and BGO matrix

In order to make up a complete Dual Readout calorimeter system, a BGO crystal matrix was placed upstream of DREAM as electromagnetic section (Figure 6.23a). It consisted of 100 BGO crystals (described in the previous section) and placed perpendicular to the beam line. For particles entering the calorimeter in its geometrical center, the ECAL had a thickness of 28 cm corresponding to 25 radiation lengths or 1.3 interaction lengths.
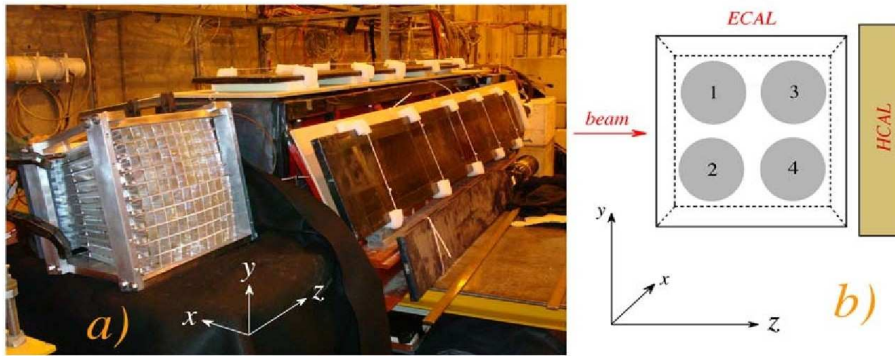

Fig. 6.23: a) The calorimeter installed in H4 test-beam. The 100-crystal BGO matrix is located upstream the fyber calorimeter and it is readout by 4 PMTs on the left side (small end face). Some of the leakage counters are visible as well. b) The location and numbering of PMTs.

DREAM was surrounded by eight leakage counters (eight scintillator paddles) to measure the energy leakage.

Upstream the BGO matrix, a 10 cm thick polyethylene target (~0.1 λ_{int}) can be placed to "simulate" interacting jets.

The matrix was readout by 4 PMTs facing the small end face side of the crystals (Figure 6.23b) and equipped with an UV filter. The distance between the PMT photocathodes and the crystal surface was about 5 cm. Each PMT detected light produced in at least 10 different crystals.

This readout was far from ideal: there was no optical contact between the crystal and the photocathode, great response non-uniformities due to the variation of quantum efficiency over the large surface of the photocathodes, strong left-right dependence of the calorimeter response as result of the tapered shape of the crystals, insensitivity to light produced in the peripheral region of the matrix which where not covered at all by the PMTs. This read-out arrangement was necessitated by the fact that only 4 electronic channels were available to split the scintillation signal into Čerenkov and scintillation component. However our goal was, as with the single crystal, to test the dual-readout principles in a hybrid calorimeter system, when a large fraction of the signal is deposited in the homogeneous detector.

Both ECAL (the BGO matrix) and HCAL (the DREAM fiber calorimeter) were calibrated with 50 GeV electrons, while the eight leakage counters where calibrated using 150 GeV muons.

In the single crystal and in DREAM standalone we saw that the ratio of Čerenkov and scintillation signals is a good measure of the *em* shower component. For the combined system there is not a simple relationship between this ratio and the f_{em} because of the different e/h values of the two components of the system, and because the energy sharing between them varies event by event. However, as can be seen in Figure 6.24, we can still use C/S as measure of the f_{em}. In Figure 6.24a the distribution of the total Čerenkov signal of the combined system is shown; in Figure 6.24b the same distribution is shown for different subsets of events, selected on the basis of the total measured C/S signal ratio. These three distributions are narrower and well described from Gaussian fits. This results confirm, even with this not ideal experimental setup, that the total C/S ratio can be used as a measure of the f_{em} even in a combined system ECAL+HCAL.

As in the case of the single crystal we expect a correlation between the Q/S ratio of the DREAM fiber calorimeter signals and the C/S ratio of the BGO matrix signals, and so between the *em* fractions measured in the two sections. In order to perform such a measurement we selected only those events in which pions start showering in the crystal section. The expected correlation between the two fractions is found for showers developing late in the BGO matrix (Figure 6.25).

This type of studies is going on; we will employ crystals with more regular shapes and a more suitable setup to improve our results.
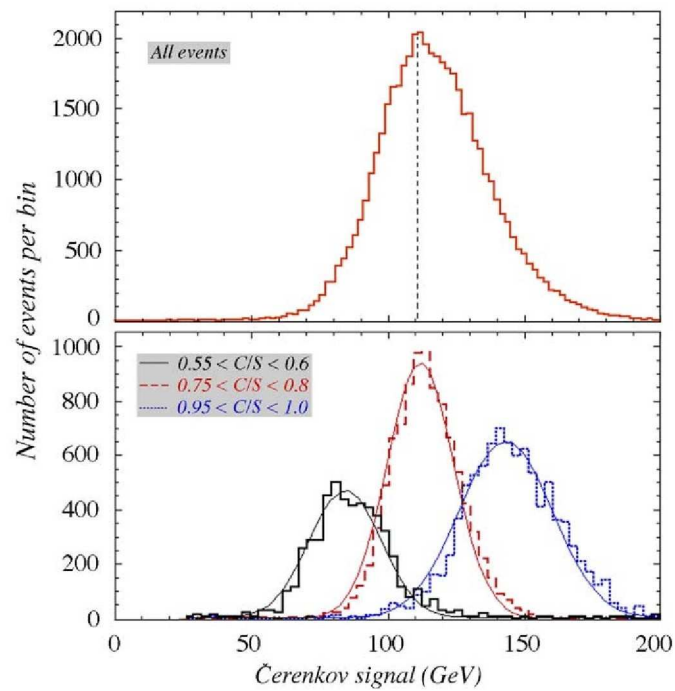
Fig. 6.24: a) Čerenkov signal distribution for 200 GeV π^+ in the system BGO matrix + DREAM fiber calorimeter. b) distributions of subsets of events selected on the basis of the ratio of the total Čerenkov and scintillation signals of the system.
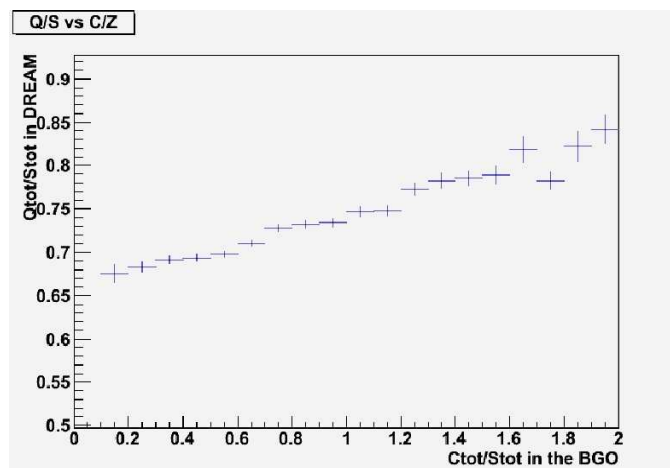

Fig. 6.25: Correlation between the ratios of the scintillation and Čerenkov signals in the two calorimeters (200 GeV π^+).

Conclusions

In this thesis are presented my research activities from 2007, performed in the field of high energy physics as part of the Cosenza group at CERN, in Geneva. The experiments I have participated to are two: ATLAS and DREAM. ATLAS is one of two general purpose experiments at the LHC proton-proton collider at CERN. My work on ATLAS was on the channels $H{\rightarrow}ZZ{\rightarrow}4l$ and $Z{\rightarrow}2\mu$. DREAM is a new experiment in calorimetry which goal is to improve hadronic calorimetry performances by comparing the scintillation and Čerenkov signals produced by particles. I participated to the data taking and to the data analysis in DREAM test -beams.

The first argument exposed in this thesis is the search for the Higgs boson in the masses between 120 and 180 GeV for the channel $H{\rightarrow}ZZ{\rightarrow}4l$ in the ATLAS experiment. First the initial results, done with the preliminary selection cuts of the "technical analysis", an initial analysis common to all the $H{\rightarrow}ZZ{\rightarrow}4l$ groups used to tune the different codes and determinate the better selection cuts, are shown. Then my work on the contribution to the Higgs signal of the backgrounds left after the standard selection criteria (especially the irreducible background $ZZ{\rightarrow}4l$) is presented. Two MonteCarlo based methods, *sideband* and *tau-ratio*, were developed to estimate this contribute.

In the second part of my thesis my work in the Z boson cross-section measurement for the channel $Z{\rightarrow}2\mu$ in ATLAS was presented. The measure of the Z cross section is a crucial task in LHC, for a better comprehension of the working of the detectors. I shown how it is possible to obtain an estimation of the background contribution to the Z cross section measurement with data driven techniques: I presented three methods to use data rejected from selection to obtain the shape of the different background contributions after the selection cuts. The quality of these methods was evaluated and the stability of their results with different sets of selection cuts was checked.

Conclusions

Finally, as third and last argument, the new calorimetric technique DREAM (Dual REadout Method) has been described in details. In particular, results of test beams applying this technique to homogeneous media (single crystals and crystal matrices) are described and analyzed in detail.

Publications

1. T. Venturelli et al., *Effects of the Temperature Dependence of the Signal from Lead Tungstate Crystals*, Nucl. Instr. and Meth. A530 (2008).

2. T. Venturelli et al., *Separation of Crystal Signals into Scintillation and Cherenkov Components*, Nucl. Instr.and Meth. A595 359 (2008).

3. T. Venturelli et al., *Search for the Standard Model H → ZZ* → 4l*, ATL-PHYS-PUB-2009-054, ATL-COM-PHYS-2009-205, May 2009.

4. T. Venturelli et al., *Statistical Combination of Several Important Standard Model Higgs Boson Search Channels*, ATL-PHYS-PUB-2009-063, ATL-COM-PHYS-2009-222, May 2009.

5. T. Venturelli et al., *Neutron signals for dual-readout calorimetry*, Nucl. Instr. and Meth. in Physics A598 422 (2009).

6. T. Venturelli et al., *Dual-Readout calorimetry with crystal calorimeters*, Nucl. Instr. and Meth. A598 710 (2009).

7. T. Venturelli et al., *New Crystals for Dual-Readout Calorimetry*, Nucl. Instr. and Meth. A604 512 (2009).

8. T. Venturelli et al., *Dual-Readout Calorimetry with a Full-Size BGO Electromagnetic Section*, Nucl. Instr. Meth. A610 488 (2009).

9. T. Venturelli et al., *Optimization of Crystals for Applications in Dual-Readout Calorimetry*, Nucl. Instr.and Meth. A621 212 (2010).

10. T. Venturelli et al., *pp→γ/Z*→ μμ and pp→W→μν inclusive cross-section measurement in early data with the ATLAS detector*, ATL-COM-PHYS-2010-124 (2010).

11. T. Venturelli et al., *A Comparison of BGO and BSO Crystals Used in the Dual-Readout Mode*, Submitted to Nuclear Instruments and Methods A (October 2010) .

12. T. Venturelli et al., *Polarization as a Tool for the Dual-Readout Calorimetry*, Submitted to Nuclear Instruments and Methods A (October 2010) .

Bibliografy

[1]   *The Large Hadron Collider Accelerator Project*, LHC CERN/AC/93-03.

[2]   *The Large Hadron Collider Conceptual Design*, LHC CERN/AC/95-05.

[3]   S. Weinberg, Phys Rev. Lett. 19 1264 (1967).

[4]   S.L. Glashow, Nucl. Phys. B22 579 (1961).

[5]   R.N. Mohapatra, *Supersymmetric Grand Unification: Lectures at TASI97*, hep-ph/9801235, (1998).

[6]   R.N. Mohapatra, *Supersymmetric Grand Unification: An Update. Lectures at Trieste Summer School*, 1999, hep-ph/9911272, (1999).

[7]   http://lepewwg.web.cern.ch/LEPEWWG/

[8]   LHCb Collaboration, *LHCb Technical Proposal*, CERN/LHCC/98-4 (1998).

[9]   ALICE Collaboration, *ALICE Technical Proposal*, CERN/LHCC/95-71 (1995).

[10]   CMS Collaboration, *CMS Technical Proposal*, CERN/LHCC/94-38 (1994).

[11]   ATLAS Collaboration, *ATLAS Technical Proposal*, CERN/LHCC/94-43 (1994).

[12]   ATLAS Collaboration, *ATLAS Letter of Intent for a General Purpose pp Experiment at the Large Hadron Collider at CERN*, CERN/LHCC/92-4, LHCC/I2 (1992).

[13]   ATLAS Collaboration, *ATLAS Detector and Physical Performance Technical Design Report (Vol. 1 and Vol. 2)*, CERN/LHCC/99-14, ATLAS TDR 14 and ATLAS TDR 15, (1999).

[14]   ATLAS Collaboration, *ATLAS Magnet System Technical Design Report*, CERN/LHCC/97-18, ATLAS TDR 6 (1997).

[15]   ATLAS Collaboration, *ATLAS Central Solenoid Technical Design Report*, CERN/LHCC/97-21, ATLAS TDR 9 (1997).

[16]   ATLAS Collaboration, *ATLAS End-Cap Toroids Technical Design Report*, CERN/LHCC/97-20, ATLAS TDR 8 (1997).

[17]   ATLAS Collaboration, *ATLAS Barrel Toroid Technical Design Report*, CERN/LHCC/97-19, ATLAS TDR 7 (1997).

[18]   ATLAS Collaboration, *ATLAS Inner Detector Technical Design Report*

Vol. 1, CERN/LHCC/97-16, ATLAS TDR 4 (1997).

[19]   ATLAS Collaboration, *ATLAS Inner Detector Technical Design Report Vol. 2*, CERN/LHCC/97-17, ATLAS TDR 5 (1997).

[20]   ATLAS Collaboration, *ATLAS Calorimeter Technical Design Report*, CERN/LHCC/96-40, ATLAS TDR 1 (1996).

[21]   ATLAS Collaboration, *ATLAS Liquid Argon Calorimeter Technical Design Report*, CERN/LHCC/96-41, ATLAS TDR 2 (1996).

[22]   ATLAS Collaboration, *ATLAS Tile Calorimeter Technical Design Report*, CERN/LHCC/96-42, ATLAS TDR 3 (1996).

[23]   ATLAS Collaboration, *ATLAS Muon Spectrometer Technical Design Report*, CERN/LHCC/97-22, ATLAS TDR 10 (1997).

[24]   C. Amelung, *The alignment system of the ATLAS muon spectrometer*. EUR Phys J C 33 s01, a999-s1001 (2004).

[25]   ATLAS Collaboration, ATLAS First Level Trigger Technical Design Report, CERN/LHCC/98-14, ATLAS TDR (1998).

[26]   ATLAS Collaboration, ATLAS High-level Triggers, DAQ and DCS Technical Design Report, CERN/LHCC/2000-17, ATLAS TDR (2000).

[27]   C. Quigg, *Electroweak Symmetry Breaking and the Higgs Sector*, hep-ph9905369, (1999).

[28]   K. Nakamura et al., *(Particle Data Group)*, J. Phys. G 37, 075021 (2010).

[29]   http://lepewwg.web.cern.ch/LEPEWWG/

[30]   A.D. Martina , J. Outhwaitea and M.G. Ryskina, *A new determination of the QED coupling alpha(M_Z^2) lets the Higgs off the hook*, Phys.Lett. B492 69 (2000).

[31]   The Aleph, Delphy, L3 and Opal Collaboration*s, Search for the Standard Model Higgs Boson at LEP*, CERN-EP/2003-011 (2003).

[32]   M. Spira, *QCD Effects in Higgs Physics*, hep-ph/9705337 (1997).

[33]   T. Sjostrand, P. Eden, C.Friberg, L. Lonnblad, G. Miu, S. Mrenna and E. Norrbin, Comput. Phys. Commun. 135 (2001).

[34]   Geant4 Collaboration, *Geant4 - A simulation toolkit*, Nuclear Instruments and Methods in Physics Research Section A 506 250-303 (2003) .

[35]   D. Adams et al., ATL-SOFT-2003-007 (2003).

[36]   S. Hassini, et al., *Muon identification algorithms in ATLAS*, NIM A572

77–79 (2007).

[37] Th. Lagouri et al., IEEE Trans.Nucl. Sci. 51 (2004).

[38] https://twiki.cern.ch/twiki/bin/view/AtlasProtected/EWPAMainPage

[39] D. Adams et al., *The ATLAS computing model*, ATL-SOFT-2004-007, CERN-LHCC-2004-037/G-085 V1.2.

[40] ATLAS Collaboration, *Search for the standard model H → ZZ* → 4l*, ATL-PHYS-PUB-2009-054, ATL-COM-PHYS-2009-205 (2009).

[41] ATLAS Collaboration, *Expected Performance of the ATLAS Experiment*, CERN-OPEN-2008-020 (2008).

[42] Lampl, W.; Laplace, S.; Lechowski, M.; Rousseau, D.; Ma, H.; Menke, S.; Unal, G., *Digitization of LAr Calorimeter for CSC simulations*, ATL-LARG-PUB-2007-011.

[43] Rebuzzi, D.; Assamagan, K.A.; Di Simone, A.; Hasegawa, Y.; Van Eldik, N., *Geant4 Muon Digitization in the ATHENA Framework*, ATL-SOFT-PUB-2007-001.

[44] Baranov, S.; Bosman, M.; Dawson, I.; Hedberg, V.; Nisati, A.; Shupe, M., *Estimation of Radiation Background, Impact on Detectors, Activation and Shielding Optimization in ATLAS*, CERN-ATLGEN-2005-001 (2005).

[45] Baroncelli, A.; Bellomo, M.; Di Ciaccio, A.; Farilla, A.; Franchino, S.; Gatti, C.; Petrucci, F.; Salvucci, A.; Sibidanov, A.; Testa, M.; Venturelli, T.; Venturi, M.; Vercesi, V., $pp \to \gamma/Z \to \mu\mu$ and $pp \to W \to \mu\nu$ *inclusive cross section measurement in early data with the ATLAS detector*, ATL-COM-PHYS-2010-124

[46] A. Tricoli, *Underlying Event Studies at ATLAS*, ATL-PHYS-PROC-2009-048

[47] R.J. Barlow and C. Beeston, Comput. Phys. Commun. 77, 219 (1526)

[48] R. Wigmans, *Calorimetry - Energy Measurement in Particle Physics*, International Series of Monographs on Physics, vol. 107, Oxford University Press (2000).

[49] N. Akchurin et al., *Hadron and Jet Detection with a Dual-Readout Calorimeter*, Nucl. Instr. And Meth. A537 537 – 561 (2005).

[50] N.Akchurin et al., *Beam Test Results from a Fine-Sampling Quartz Fiber Calorimeter for Electron, Photon and Hadron Detection*, Nucl. Instr. and Meth. A399 202 (1997).

[51] N.Akchurin et al., *Measurement of the Contribution of Neutrons to Hadron Calorimeter Signals*, Nucl. Instr. and Meth. A581 643 (2007).

Bibliography

[52] N.Akchurin et al., *Neutron Signals for Dual-Readout Calorimetry*, Nucl. Instr. and Meth. A598 422 (2009).

[53] N.Akchurin et al., *Contributions of Cherenkov light to the signals from lead tungstate crystals*, Nucl. Instr. and Meth. A582 447 (2007).

[54] N.Akchurin et al., *Separation of crystal signals into scintillation and Cherenkov component*, Nucl. Instr. and Meth. A595 539 (2008).

[55] N.Akchurin et al., *Effects of the temperature dependence of the signals from lead tungstate crystals*, Nucl. Instr. and Meth. A593 530 (2008).

[56] Millers, et al., Phys. Status Solidi (b) 203 585 (1997).

[57] N.Akchurin et al., *Dual-Readout Calorimetry with Crystal Calorimeters*, Nucl. Instr. and Meth. A598 710 (2009).

[58] N.Akchurin et al., *New Crystals for Dual Readout Calorimetry*, Nucl. Instr. and Meth. A604 512 (2009).

[59] N. Akchurin et al., *Optimization of Crystals for Applications in Dual-Readout Calorimetry*, Nucl. Instr. and Meth. A621 212 (2010) .

[60] N. Akchurin et al., *Dual-Readout Calorimetry with a Full-size BGO Electromagnetic Section*, Nucl. Instr. and Meth. A610 488 (2009).

[61] N.Akchurin et al., *Dual-readout Calorimetry with lead tungstate crystals*, Nucl. Instr. and Meth. A584 273 (2008).

Ringraziamenti

Voglio ringraziare in primo luogo il mio supervisore, la professoressa Laura La Rotonda, per tutto l'aiuto e l'appoggio fornitemi in questi anni, in particolare nell'ultimo periodo durante la lunga stesura di questa tesi. Il suo appoggio, sia come esperienza e competenza che come sostegno durante gli anni di dottorato è stato per me fondamentale e imprescindibile.

Sono assai riconoscente per l'aiuto, i consigli, il sostegno (ma anche solo la compagnia) fornitemi da tutti i professori, ricercatori e studenti dell'UNICAL con cui mi sono trovato a lavorare in questi quattro anni. In particolare vorrei ringraziare per il grandissimo aiuto datomi la dott.essa Evelin Meoni, senza cui non avrei potuto impostare buona parte del lavoro sull'Higgs esposto in questa tesi, per i consigli "al volo" il dott. Antonio Policicchio (con cui ho condiviso per diverso tempo l'ufficio), e per il sostegno fornitemi da nostro capogruppo, Giancarlo Susinno.

Devo inoltre ringraziare il dott. Claudio Gatti, di Frascati, per l'aiuto assolutamente fondamentale che mi ha fornito in questi due anni nella stesura del lavoro sulle Z e per la sua continua disponibilità, il dott. Massimiliano Bellomo di Pavia per l'appoggio datomi sempre in tale ambito, e in generale vorrei ringraziare tutta la collaborazione con cui è stata prodotta la nota su W e Z impiegando EWPA per il lavoro utile e interessante che ho potuto svolgere insieme a loro.

Un caloroso grazie va anche a Richard Wigmans, della Texas University, e a tutta la collaborazione DREAM per questi produttivi anni di lavoro insieme.

Infine, vorrei ringraziare la mia famiglia e i miei amici, mia madre in particolare, per tutti questi anni di sostegno silenzioso (e in certi casi anche non così silenzioso), e tutti quelli che mi sono senz'altro dimenticato di citare qui.